The Pennsylvania State University

The Graduate School

Department of Materials Science and Engineering

HEAT TRANSFER, FLUID FLOW AND MASS TRANSFER IN LASER WELDING OF STAINLESS STEELWITH SMALL LENGTH SCALE

A Thesis in

Materials Science and Engineering

by

Xiuli He

Submitted in Partial Fulfillment
of the Requirements
for the Degree of

Doctor of Philosophy

May 2006

The thesis of Xiuli He was reviewed and approved* by the following:

Tarasankar DebRoy
Professor of Materials Science and Engineering
Thesis Advisor
Chair of Committee

Long-Qing Chen
Professor of Materials Science and Engineering

Christopher Muhlstein
Assistant Professor of Materials Science and Engineering

Stephen M. Copley
Professor of Mechanical Engineering

Gary L. Messing
Professor of Ceramic Science and Engineering
Head of the Department of Materials Science and Engineering

*Signatures are on file in the Graduate School

ABSTRACT

Nd: YAG Laser welding with hundreds of micrometers in laser beam diameter is widely used for assembly and closure of high reliability electrical and electronic packages for the telecommunications, aerospace and medical industries. However, certain concerns have to be addressed to obtain defect-free and structurally sound welds. During laser welding, Because of the high power density used, the pressures at the weld pool surface can be greater than the ambient pressure. This excess pressure provides a driving force for the vaporization to take place. As a result of vaporization for different elements, the composition in the weld pool may differ from that of base metal, which can result in changes in the microstructure and degradation of mechanical properties of weldments. When the weld pool temperatures are very high, the escaping vapor exerts a large recoil force on the weld pool surface, and as a consequence, tiny liquid metal particles may be expelled from the weld pool. Vaporization of alloying elements and liquid metal expulsion are the two main mechanisms of material loss. Besides, for laser welds with small length scale, heat transfer and fluid flow are different from those for arc welds with much larger length scale. Because of small weld pool size, rapid changes of temperature and very short duration of the laser welding process, physical measurements of important parameters such as temperature and velocity fields, weld thermal cycles, solidification and cooling rates are very difficult. The objective of the research is to quantitatively understand the influences of various factors on the heat transfer, fluid flow, vaporization of alloying elements and liquid metal expulsion in Nd:YAG laser welding with small length scale of 304 stainless steel.

In this study, a comprehensive three dimensional heat transfer and fluid flow model based on the mass, momentum and energy conservation equations is relied upon to calculate temperature and velocity fields in the weld pool, weld thermal cycle, weld pool geometry and solidification parameters. Surface tension and buoyancy forces were considered for the calculation of transient weld pool convection. Very fine grids and small time steps were used to achieve accuracy in the calculations. The calculated weld pool dimensions were compared with the corresponding measured values to validate the model. Dimensional analysis was carried out to evaluate the relative importance of the various driving forces and heat transferred by convection and conduction. The behavior of the mushy zone, i.e., the solid-liquid two phase region, during heating and cooling were investigated. Results also revealed information about the important solidification parameters R, the solidification rate, and G, the temperature gradient in the mushy zone at the mushy zone/liquid front. These data are useful for determining the solidification morphology and the scale of the solidification substructure.

Using the computed temperature fields, the mass loss and composition change due to vaporization of various alloying elements and vapor composition during laser spot welding were calculated, based on principles of transport phenomena, kinetics and thermodynamics. The vaporization of alloying elements was considered to result from concentration and pressure gradients. Both vaporization and condensation were considered in the model. The calculations show that the vaporization was concentrated in a small region under the laser beam where the temperature was very high. After laser spot welding, the concentration of manganese and chromium decreases, while the concentration of iron and nickel increases owing to welding. The vapor composition and composition change in the weld pool predicted by the model are in fair agreement with the corresponding experimental results.

For a weld pool of known composition, the vaporization rates of various alloying elements are strongly affected by the surface temperatures. Since the relative rates of vaporization of two alloying elements are determined by the local temperature, the vapor composition can be used to determine the effective temperature of the weld pool. The effective temperature determined from the vapor composition has been found to be close to the numerically computed peak temperature at the weld pool surface using a three-dimensional, transient, numerical model. Estimation of the approximate values of peak temperature during laser spot welding by measuring vapor composition overcomes the problems encountered in direct measurement of temperatures.

The computed vapor loss was found to be lower than the measured weight loss. Therefore, so the liquid metal expulsion was examined by experiments. Liquid metal expulsion is caused by the recoil force exerted by escaping metal vapors when the temperature at the weld pool surface is very high. The liquid metal expulsion can be predicted by balancing the vapor recoil force with the surface tension force at the periphery of the liquid pool under various welding conditions. The laser power density and pulse duration are the two most important parameters for liquid metal expulsion during laser spot welding. Larger laser power density and longer pulse duration increase the tendency of occurrence of liquid metal expulsion. Furthermore, the depression of the weld center under the recoil pressure could be used as an indicator of liquid metal expulsion during welding.

The results presented in this thesis, taken as a whole, indicate that heat transfer and fluid flow, alloying element vaporization, composition change and liquid metal expulsion of weld pool can be predicted from the integrated model based on mass, momentum and energy conservation equations. The thesis research work represents a contribution to the growing quantitative knowledge base in laser welding with small length scale.

TABLE OF CONTENTS

LIST OF FIGURES

LIST OF TABLES

ACKNOWLEDGEMENTS

I would first like to express my sincere gratitude and deep appreciation to my advisor, Dr. Tarasankar DebRoy, for his patient and expert guidance throughout this research. I am grateful to Mr. Phillip W. Fuerschbach and Mr. Jerome Norris at Sandia National Laboratories for their invaluable experimental work and Dr. John W. Elmer at Lawrence Livermore National Laboratory. I consider myself fortunate to have had the opportunity to work with them.

I would like to thank Dr. Long-qing Chen, Dr. Christopher Muhlstein and Dr. Stephen M. Copley for serving on my thesis committee and giving their valuable time to review and comment on this thesis.

I would also like to thank my colleagues, Dr. Wei Zhang, Dr. Gour G. Roy, Mr. Saraubh Mishra, Mr. Amit Kumar, Mr. Rituraj Nandan and Mr. Rohit Rai, for their outstanding research and great help.

Last but not least, I am grateful to my parents for their love and support throughout my life, and I am deeply indebted to my husband, Xiang Xu, for his love, encouragement, understanding and support during the course of my study.

I would like to acknowledge the financial support of the U.S. Department of Energy, Office of Basic Energy Sciences, Division of Materials Sciences, under grant number DE-FGO2-01ER45900.

Chapter 1

INTRODUCTION

1.1 General Background

Laser welding with small length scale is used in many applications in the electronics, instrumentation, packaging, aerospace and medical industries. Generally speaking, small length scale means that laser beam diameter is not more than 1 mm. Lasers are well suited for welding with small length scale because they can deliver a controlled amount of energy to very small components with a high degree of precision. In recent years, Nd-YAG lasers have been used in electronic packaging [1-3] where joining of smaller components is of interest. The welding of small components is different from that for larger welds. For the welding of larger components, a keyhole is often deliberately formed to achieve deep penetration welds in thick plates. In such cases, contamination of the weldment by the metal vapors and ejected particles is often not a major issue. However, for the welding of small components, where a large depth of penetration may not be needed since fairly thin parts are joined, an important requirement is to keep the parts free of contamination. Since the components are often processed in a clean room environment, discharge of metal vapors is not acceptable.

During laser welding, the interaction of the heat source and the material results in rapid heating, melting and circulation of molten metal in the weld pool aided by surface tension gradient and buoyancy forces. The resulting flow of liquid metal and heat transfer determines the temperature and velocity fields, which are important because they determine the geometry, composition, structure and the resulting properties of the welds. Most previous research on welding with very small length scale focused on welding methods, weld quality and weld properties [3-6]. Very little effort has been made to understand the physical processes in welding with small length scale. This is due in part to the experimental measurements of the temperature and velocity fields during laser welding being difficult because of the small size of the weld pool, insufficient time for measurement and high heating and cooling rates. In recent decades, the application of numerical transport phenomena has resulted in useful information about the thermal cycles and weld pool geometry in both linear and spot welding [7,8]. However, most of these studies were concerned with arc welds where the length scale was much larger. Thus far, heat transfer and fluid flow in laser welds with small length scale have not received much attention.

Laser spot welds behave very differently from their moving weld counterparts because the temperature profiles never reach a steady state, and also because the heating and cooling rates for these welds are much higher than those of linear welds. Generally, the order of pulse duration for laser spot welding is less than several milliseconds, one thousandth of that for arc spot welding. Such short time makes it much more difficult to make physical measurements of the above-mentioned important parameters. The heat transfer and fluid flow during laser spot welding still remain to be investigated to understand how the velocity and temperature fields evolve during heating and cooling, and how the heat is transferred in such a short time and small weld pool. Such a computationally intensive investigation, requiring use of fine grids and very small time steps, has now become practical because of recent advances in computational hardware and software.

Because of the high power density used in laser welding, the temperatures of weld metal often exceed the boiling points of materials being welded. In such situations, the equilibrium pressure on the weld pool surface becomes higher than the atmospheric pressure, causing significant vaporization to take place from the weld pool surface [9-13]. Moreover, if the weld pool temperature is very high, the escaping vapor exerts a large recoil force on the weld pool surface [14]. As a consequence, the molten metal may be expelled from the weld pool. Vaporization and liquid metal expulsion are the two main mechanisms of material loss during laser welding. The loss of alloying elements can result in significant changes in the microstructure and degradation of mechanical properties of weldments [11,15]. Cieslak and Fuerschbach [11] investigated the property change of aluminum alloys 5456 and 5086. They found that the hardness of weld metal was lower than the base metal due to the magnesium vaporization. The loss of hardness was attributed to a reduction in the solid solution strengthening effect as a result of lower magnesium concentration. Moon and Metzbower [**15**] investigated the change of properties of aluminum alloy before and after welding using a CO_2 laser with He gas shield. They found that the tensile properties of the welds were inferior to the base metal, mainly because of magnesium depletion, loss of strain hardened structure, and porosity. For the welding of small components, especially in the electronics industry, the components are often processed in a clean room environment, and discharge of metal vapors is not acceptable. During laser assisted joining of components, loss of alloying elements needs to be minimized. Therefore, quantitative understanding of the vaporization of alloying elements and liquid metal expulsion is important in the welding of engineering alloys.

In order to have a quantitative understanding of the vaporization of weld metal, a comprehensive model is needed. The Langmuir equation [**16**] has been widely used for the estimation of vaporization rates during welding [**11**,**12**]. This simple model is useful in predicting the relative vaporization rates of various alloying elements. However, since it was derived for vaporization in a vacuum where no significant condensation of the vaporized species occurred, the Langmuir equation significantly overestimates the vaporization rate under commonly used welding conditions. Aden *et al*. [**17**] investigated laser-induced vaporization from steel and aluminum surfaces as a function of laser intensity and material properties. A material-dependent minimum laser intensity above which no further expansion of the metal vapor occurs was discussed. However, the model did not take into account the flow of liquid metal in the weld pool nor the detailed heat transfer in the weldment. A theoretical model was developed by Dilthey *et al*. [**18**] to describe the vaporization of alloying elements during laser welding. Two important processes were analyzed, the diffusion of alloying elements from the interior to the weld surface and their subsequent vaporization from the weld pool surface. Both of the models ignored the condensation of the metal vapor. Anisimov [**19**] and Knight [**20**] derived expressions for the vapor temperature, density, velocity and the extent of condensation by solving the equations of conservation of mass, momentum and energy in a thin layer adjacent to the liquid-vapor interface, known as the Knudsen layer. Their approach has been incorporated into a vaporization model [9,10] to calculate the laser-induced vaporization rate.

All of these calculations were performed for the vaporization of linear laser welding. For laser spot welding, vaporization of alloying elements differs in several ways. First, the vaporization rate is strongly time-dependent, i.e., the rate is negligible at the initiation of the pulse and gradually increases owing to temperature increase. Second, because of the short duration of the laser pulse, experimental determination of temperature and velocity fields is difficult and remains both an important goal and a major challenge in the field. Third, although both the surface area and the volume of the weld pool are small, they change significantly with time. As a result of these difficulties, very little information is available in the literature about calculation of alloying element vaporization during laser spot welding. As such, it will be investigated in this project.

1.2 Objectives

The overall objective of this study is to develop improved understanding of important physical phenomena during Nd:YAG laser welding of 304 stainless steel with small length scale. The temperature and velocity fields, weld pool geometry, alloying element vaporization and resultant composition change, liquid metal expulsion and weld pool solidification were investigated. The primary objectives of this study are as follows:

1) To investigate heat transfer and fluid flow to obtain the information of temperature and velocity fields and the weld pool thermal cycle, as well as to predict the weld pool geometry, solidification rate and cooling rate for both laser linear and spot welding based on mass, momentum and energy conservation equations.

2) To analyze the two mechanisms of material loss during laser spot welding: vaporization and liquid metal expulsion. The analysis includes the following two components:

(a) Calculation of mass loss, vapor composition and composition change in the weld pool as a function of time due to vaporization of various alloying elements, using the computed temperature field from heat transfer and fluid flow model, and determination of the temperature on the weld pool surface from vapor composition.

(b) Investigation of the conditions for the occurrence of liquid metal expulsion from force balance and free surface deformation and calculation of ejected droplet size.

In this thesis, an integrated comprehensive model is used to calculate heat transfer, fluid flow and vaporization of alloying elements. The results provide detailed information of the weld pool, including three-dimensional temperature and velocity fields, weld pool geometry, solidification parameters, spatial distribution of vapor fluxes of various alloying elements, and the composition change of alloys due to vaporization — all for laser welding with small length. This information is difficult to obtain experimentally due to the small weld pool size, insufficient time for measurement and high heating and cooling rates. The model can serve as a tool for the quantitative understanding of the influences of weld variables on weld pool geometry and weld metal composition change for laser welding of various alloys with small weld pool size.

1.3 Thesis Structure

The thesis consists of eight chapters. Chapter 1 describes the general background, objective and contents of the thesis.

Chapter 2 is a critical literature review on current questions and problems in laser welding, with emphasis on energy absorption, heat transfer and fluid flow in the weld pool, vaporization of alloying elements and resulting composition change, and liquid metal expulsion.

In Chapter 3, the models developed in the present study, the three dimensional heat transfer and fluid flow model and the vaporization model, are described. The procedures for applying these models for the prediction of the weld pool geometry, vaporization loss and composition change are also presented.

In Chapter 4, the heat transfer and fluid flow during both laser spot welding and laser linear welding are simulated. The evolution of temperature and velocity fields, and weld pool geometry in laser welding is studied using the three dimensional heat transfer and fluid flow model. Verification of the model is performed through comparing the calculated weld pool geometry with corresponding experimental results. Dimensionless analysis is carried out to understand both the heat transfer mechanism in the weld pool and the significance of the various driving forces for the liquid convection. The behavior of the mushy zone, i.e., the solid + liquid two-phase region, during heating and cooling is also investigated. Results reveal information about the important solidification parameters, i.e., the temperature gradient and solidification rate along the mushy zone/ liquid interface. These data are useful in determining the solidification morphology and the scale of the solidification substructure.

In Chapter 5, the method of temperature determination from vapor composition for various welding conditions is described. Composition of the metal vapor from the weld pool is determined by condensing a portion of the vapor on the inner surface of a both-end-open quartz tube which has been mounted perpendicular to the sample surface and co-axial with the laser beam. The results from this method are compared with those calculated from the three dimensional heat transfer and fluid flow model. Temperature determination from vapor composition overcomes prior problems encountered via direct measurement of peak temperature in the weld pool.

In Chapter 6, the simulation of vaporization of alloying elements and composition change in the weld pool is performed based on the conservations of mass, momentum and translational kinetic energy in the gas phase. The vaporization is driven by both concentration and pressure gradient. Both vaporization and condensation are considered in the calculation. The experimentally-determined vapor composition, overall vaporization loss and composition change are compared with the corresponding modeling results. Besides vaporization of alloying elements, another kind of material loss, liquid metal expulsion during laser spot welding of 304 stainless steel, is investigated experimentally and theoretically. Conditions for the initiation of liquid metal expulsion are examined by comparing the vapor recoil force with the surface tension force at the periphery of the liquid pool. The free surface profile is simulated at different times by minimizing the total surface energy. The predictions of liquid metal expulsion are compared with experimental observations under different welding conditions.

In Chapter 7, a summary and conclusions of the present study are presented.

1.4 References

1. W. S. Chang and S. J. Na, *J. Mater. Proc. Tech.*, **120**, 208 (2002).

2. M. J. Jackson and W. O'Neill, *J. Mater. Proc. Tech.*, **142**, 517 (2003).

3. K. Uenishi, M. Seki, M. Takatsugu, T. Kunimasa, K. F. Kobayashi, T. Ikeda and A. Tsuboi, *Mater. Trans.*, **43**, 3083 (2002).

4. S. Bednarczyk, R. Bechir and P. Baclet, *Appl. Phys. A: Materials Science and Processing*, **69**, S495 (1999).

5. H. J. Booth, J. Mater. *Thin Solid Films*, **453-454**, 450 (2004).

6. S. Ahn, D. W. Kim, H. S. Kim and S.J. Ahn, *J. Cho, Microelecton. Eng.*, **69**, 57 (2003).

7. W. Zhang, G. G. Roy, J. Elmer and T. DebRoy, *J. Appl. Phys.*, 93, 3022 (2003).

8. W. Zhang, J. W. Elmer and T. DebRoy, *Mater. Sci. Eng. A*, **333**, 320 (2002).

9. H. Zhao and T. DebRoy, *Metall. Trans. B*, **32B**, 163 (2001).

10. K. Mundra and T. DebRoy, *Metall. Trans. B*, **24B**, 145 (1993).

11. M. J. Cieslak and P. W. Fuerschbach, *Metall. Trans. B*, **19B**, 319 (1988).

12 A. Block-bolten and T. W. Eager, *Metall. Trans. B*, **15B**, 461 (1984).

13 T. A. Palmer and T. DebRoy, *Metall. Trans. B*, **31B**, 1371 (2000).

14. S. Basu and T. DebRoy, *J. Appl. Phys.*, **72**, 3317 (1992).

15. D. W. Moon and E. A. Metzbower, *Welding J.*, **62**, 53s (1983).

16. S. Dushman and J. M. Lafferty, eds., *Scientific Foundations of Vacuum Science* (New York: John Wisley, 1962).

17. M. Aden, E. Beyer, G. Herziger and H. Kunze, *J. of Phys. D: Appl. Phys.*, **25**, 57 (1992).

18. U. Dilthey, A. Goumeniouk, V. Lopota, G. Turichin and E. Valdaitseva, *J. of Phys. D: Appl. Phys.*, **34**, 81 (2001).

19. S. I. Anisimov and A. Kh Rakhmatulina, *Soviet Physics – JETP*, **37**, 441 (1973).

20. C. J. Knight, *AIAA J.*, **17**, 519 (1979).

Chapter 2

BACKGROUND

The purpose of this chapter is to critically review the background materials necessary for the research in the present thesis. The subject matter is classified into three categories: (1) heat transfer and fluid flow, (2) vaporization of alloying elements, and (3) liquid metal expulsion.

2.1 Heat Transfer and Fluid Flow

2.1.1 Energy Absorption

During welding, only a portion of the total energy supplied by the heat source is absorbed by the workpiece. The absorbed energy is responsible for the outcome of the welding process. Consequence of the absorbed energy includes: formation of the liquid pool, establishment of the time-dependent temperature field in the entire weldment, and development of the structure and properties of the weldment [1]. The absorptivity can be measured with a calorimeter. The heat transferred from the heat source to the workpiece is in turn transferred from the workpiece to the calorimeter. For example, Fuerschbach [2] used a calorimeter to determine the absorption efficiency of laser energy by the workpiece during laser welding of 304 stainless steel.

The physical phenomena that influence the energy absorption in the workpiece are unique to each welding process. Fig. 2.1 summarizes the absorptivity measured in several welding processes. It is shown that the absorptivity in laser beam welding is very low because of the high reflectivity of metal surfaces to a laser beam. As much as 95% of the CO_2 beam power can be reflected by a polished metal surface. Reflectivity is slightly lower with a YAG laser beam. However, the reflectivity can be significantly reduced by surface modifications, such as roughing, oxidizing or coating [3]. In addition to altering the nature of the surface, the absorptivity of the laser beam by the workpiece is also affected by factors such as the temperature, the wavelength of the laser, the joint geometry, and the size and nature of the plasma present above the weld pool [1,4]. During conduction mode laser welding, the absorptivity is equivalent to the absorptivity of the metal. When a keyhole is formed, the absorptivity can be much higher than the absorptivity of the metal because of multiple reflections within the keyhole [2]. Understanding the nature of coupling between an incident laser beam and a metal under welding conditions provides insight into ways in which laser welding can be optimized. It also may suggest new directions for improvements in laser welding technology and how welding defects can be minimized.

For Nd:YAG laser welding of stainless steel, the reported values of the absorption coefficient vary significantly [5-9]. For example, Cremers, Lewis and Korzekwa [5] indicated that the absorption coefficient of Nd:YAG laser in 316 stainless steel was in the range of 0.21 to 0.62. Fuerschbach and Eisler found that the absorption of the pulsed Nd: YAG laser in 304 stainless steel tended to vary from 38% to 67% and to be relatively insensitive to beam intensity [6]. For laser welding, laser radiation incident on the surface of metal is absorbed by electrons. So with a clean metal surface, the absorptivity can be calculated from the electrical resistivity of the metal substrate. Bramson [9] related the absorptivity to the substrate resistivity and the wavelength of the laser radiation:

$$\eta(T) = 0.365\left(\frac{\alpha}{\lambda}\right)^{1/2} - 0.0667\left(\frac{\alpha}{\lambda}\right) + 0.006\left(\frac{\alpha}{\lambda}\right)^{3/2} \qquad (2.1)$$

where λ is the wavelength, α is the electrical resistivity of the materials. Equation 2.1 is accurate when the metal surface is clean and a plasma plume does not affect the absorption of the laser beam.

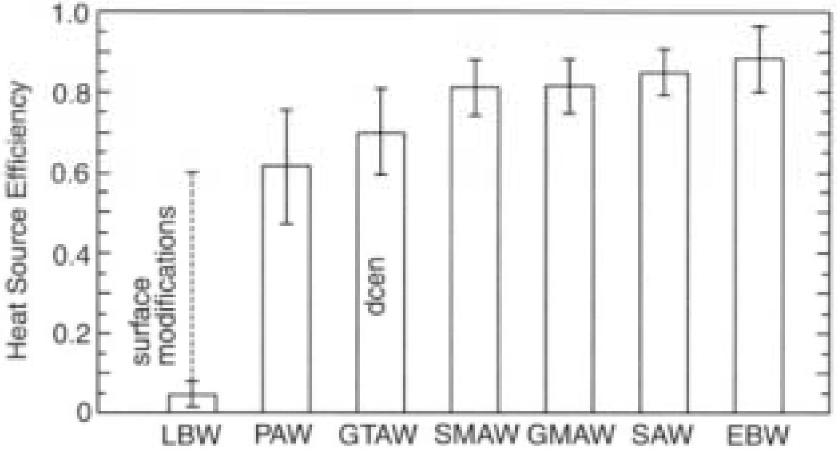

Fig. 2.1: Heat source efficiencies in several welding processes [10].

2.1.2 Heat Conduction in Welding

Fig. 2.2 is a schematic diagram showing the welding of a stationary workpiece. As shown in this figure, there are three distinct regions in the weldment: the fusion zone (FZ), the heat affected zone (HAZ) and the base material.

Except for the initial and final transients of welding, heat flow in a workpiece of sufficient length is steady, or quasi-stationary, with respect to the moving heat source. In other words, the temperature distribution and the pool geometry do not change with time. By assumption of steady state, point heat source and ignoring the convection in the weld pool, the analytical solution derived by Rosenthal for three-dimensional heat flow in a semi-infinite workpiece is as follows [10]:

$$\frac{2\pi(T - T_0)kR}{Q} = \exp\left(\frac{-V(R - x)}{2\alpha}\right) \tag{2.2}$$

where T is the temperature, T_0 is the workpiece temperature before welding, k is the thermal conductivity, R is the radial distance from the origin, where the axis of the heat source meets the workpiece, namely, $(x^2 + y^2 + z^2)^{1/2}$, Q is the heat transferred form heat source to workpiece, V is the welding speed, α is the thermal diffusivity, k/ρC, and ρ and C are density and specific heat, respectively. The Rosenthal's analytical solutions, though base on many simplifying assumptions, are easy to use and have been greatly appreciated by the welding industry.

Predicting or interpreting metallurgical transformations at a point in the solid material near a weld requires some knowledge of the peak temperature reached at a specific location. The peak temperature T_p on the workpiece surface (z = 0) at a distance y away from the fusion line (measured along the normal direction) is calculated by Adams' Equation [10]:

$$\frac{1}{T_p - T_0} = \frac{5.44\pi k\alpha}{QV}\left(2 + \left(\frac{Vy}{2\alpha}\right)^2\right) + \frac{1}{T_m - T_0} \tag{2.3}$$

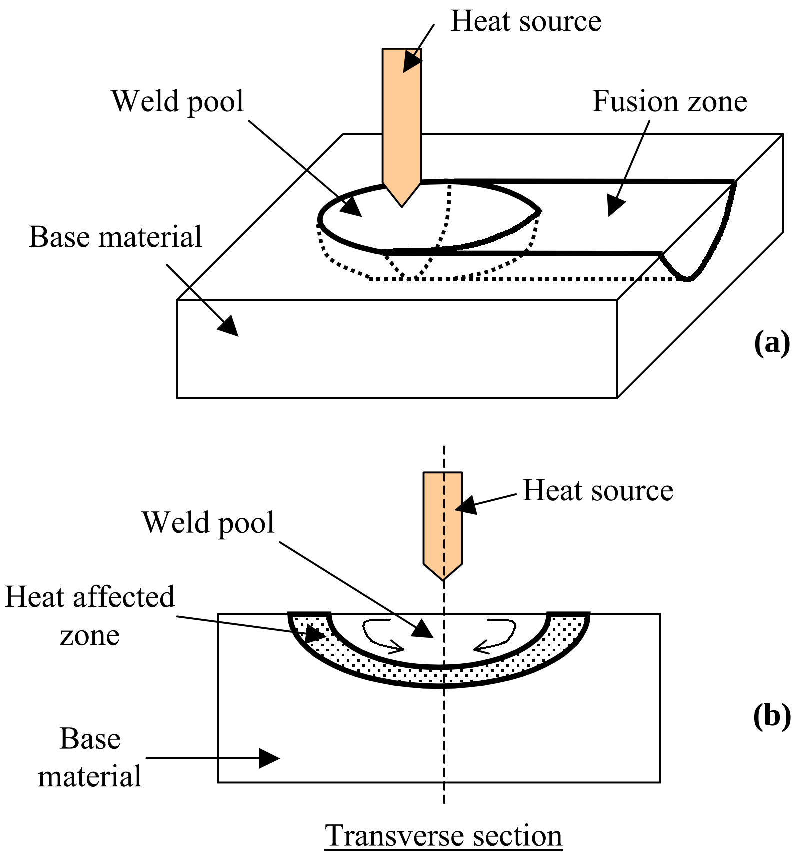

Fig. 2.2: Schematic plot depicting the fusion welding process. (a) Interaction between the heat source and the base material; and (b) the transverse section directly under the heat source [10].

2.1.2.1 Buoyancy Force

The buoyancy force is caused by density variations due to the temperature gradients within the weld pool, as shown in Fig. 2.3(a). The liquid metal rises along the pool center with low magnitude and falls along the pool boundary due to the local variation of density. This flow pattern is expected because the liquid metal near the heat source is at a relatively high temperature. It moves upwards because of its relatively low density. On the other hand, the liquid metal near the pool boundary has relatively low temperature, and it flows downward because of its high density.

The buoyancy force can be expressed as [14,15]:

$$F_b = \rho g \beta \left(T - T_{ref}\right) \tag{2.4}$$

where ρ is the density of the liquid metal, g is the acceleration due to gravity, β is the thermal expansion coefficient, T is the temperature of the liquid metal, and T_{ref} is an arbitrarily selected reference temperature.

2.1.2.2 Marangoni Shear Stress

Surface tension (γ) is a thermo-physical property of the liquid metal, which may generate a shear stress at the liquid/gas interface. The spatial gradient of surface tension is a stress, which is known as the Marangoni shear stress. This stress arises due to spatial variation of temperature and composition, which can be expressed as:

$$\tau = \frac{\partial \gamma}{\partial T}\frac{\partial T}{\partial r} + \frac{\partial \gamma}{\partial C}\frac{\partial C}{\partial r} \tag{2.5}$$

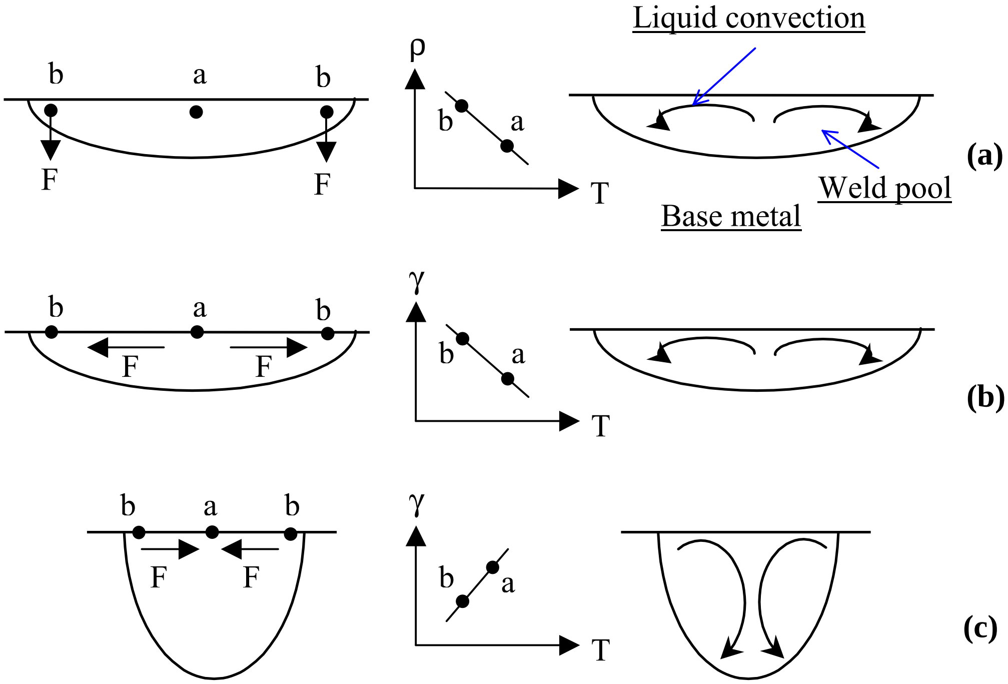

Fig. 2.3: Various driving forces and the resulting liquid convection in the weld pool [11]. (a) Buoyancy force, (b) surface tension gradient force with negative ∂γ/∂T, (c) surface tension gradient force with positive ∂γ/∂T. Symbol γ is the surface tension, ∂γ/∂T is the temperature coefficient of surface tension, T is the temperature, ρ is the density, a and b are two locations in the weld pool, and F is the driving force.

where τ is the shear stress due to surface tension, T is the temperature, r is the distance along the surface from the heat source, and C is the concentration of the surface active element. In most cases, the difference in surface tension is due to the spatial temperature variation. In other words, the $\partial\gamma/\partial C$ term in Equation 2.5 is zero, and the shear stress depends only on $\partial\gamma/\partial T$ and the spatial temperature gradient $\partial T/\partial r$ at the pool surface.

In the absence of a surface active element, the temperature coefficient of surface tension ($\partial\gamma/\partial T$) for many materials is less than zero. In other words, the higher the temperature, the lower the surface tension. Hence, at the weld pool top surface, the liquid metal flows radically outward since the warmer liquid metal of lower surface tension near the center of the pool is pulled outward by the cooler metal of higher surface tension at the pool edge [11]. Pushed by the strong outward flow at the top surface, the liquid metal is transported outwards from the middle of the weld pool and arises at the center of the pool, as shown in Fig. 2.3(b).

If a small yet significant amount of surface active elements such as sulfur and oxygen are presented in the weld pool, the value of $\partial\gamma/\partial T$ can be dramatically altered. For liquid material with a positive value of $\partial\gamma/\partial T$, the direction of the Marangoni shear stress and the resulting flow pattern are shown in Fig. 2.3(c). This flow pattern is expected since the cooler metal of lower surface tension at the pool edge is pulled inward by the warmer liquid metal of higher surface tension near the center of the pool. If the value of $\partial\gamma/\partial T$ in the weld pool is not always positive or negative, the resulting flow pattern may be even more complicated than those shown in Figs. 2.3(b) and 2.3(c), and four circulation loops may exist in the weld pool.

A relationship between the interfacial tension of a liquid metal and the surface active element can be expressed by using a combination of Gibbs and Langmuir absorption isotherms:

$$\gamma - \gamma^0 = -RT\Gamma_s \ln(1 + Ka_i) \qquad (2.6)$$

where γ^0 is the surface tension of pure metal at the reference temperature, R is the gas constant, T is the absolute temperature, Γ_s is the surface excess of the solute at saturation solubility, K is the adsorption coefficient, and a_i is the activity of species i in the solution.

Sahoo *et al.* [16] determined the $\partial\gamma/\partial T$ as a function of both temperature and composition, which is expressed as:

$$\frac{\partial\gamma}{\partial T} = A - R\Gamma_s \ln\left(1 + Ka_i\right) - \frac{Ka_i}{\left(1 + Ka_i\right)} \frac{\Gamma_s\left(\Delta H^o - \Delta\overline{H}_i^M\right)}{T} \qquad (2.7)$$

where A is the $\partial\gamma/\partial T$ value for a pure metal, ΔH^o is the standard heat of adsorption, and $\Delta\overline{H}_i^M$ is the partial molar enthalpy of mixing of species i in the solution.

2.1.3 Estimation of Scaling and Order of Magnitude

In order to understand the heat transfer and fluid flow behavior in the weld pool, it is useful to check some dimensionless numbers. These dimensionless numbers characterize the relative importance of the driving forces responsible for the motion of the fluid flow and the heat transfer mechanism.

2.1.3.1 Relative Importance of Driving Forces

Several dimensionless numbers have been used in the literature to determine the relative importance of different driving forces in the weld pool [17]. The ratio of buoyancy force to viscous force is determined by the Grashof number:

$$Gr = \frac{g\beta L_b^3 \Delta T \rho^2}{\mu^2} \qquad (2.8)$$

where g is the gravitational acceleration, β is the thermal expansion coefficient, L_b is a characteristic length for the buoyancy force in the liquid pool which is approximated by one eighth of the pool radius [17], ΔT is the temperature difference between the peak pool temperature and solidus temperature, ρ is the density, and μ is the viscosity. Surface tension Reynolds number, Ma, is used to describe the ratio of surface tension gradient force to viscous force, and is calculated as:

$$\mathrm{Ma} = \frac{\rho L_R \Delta T \left|\frac{\partial \gamma}{\partial T}\right|}{\mu^2} \qquad (2.9)$$

where L_R is the characteristic length of the weld pool and is assumed to be equal to half of the weld pool width.

The relative importance of the primary driving forces can be judged by the combination of these dimensionless numbers. The ratio of surface tension force to buoyancy force is expressed as:

$$R_{s/b} = \frac{\mathrm{Ma}}{\mathrm{Gr}} = \frac{L_R \left|\frac{\partial \gamma}{\partial T}\right|}{g\beta L_b^3 \rho} \qquad (2.10)$$

Such dimensionless numbers can be used to predict the size and shape of the FZ and HAZ. For instance, if the surface tension gradient force with negative $\partial\gamma/\partial T$ is largely responsible for the liquid motion, the resulting weld pool is expected to be wide and shallow.

2.1.3.2 Relative Importance of Heat Transfer by Conduction and Convection

In the weld pool, heat is transported by a combination of convection and conduction. The relative importance of convection and conduction in the overall transport of heat can be evaluated from the value of the Peclet number, Pe, which is defined by:

$$\mathrm{Pe} = \frac{\mathrm{heat}_{\mathrm{convection}}}{\mathrm{heat}_{\mathrm{conduction}}} = \frac{u\rho C_p \Delta T}{k\Delta T / L_R} = \frac{u\rho C_p L_R}{k} \qquad (2.11)$$

where u is the average velocity, L_R is the characteristic length taken as the pool radius at the top surface of the weld pool, C_p is the specific heat, and k is the thermal conductivity. When Pe is large, which in physical terms means large melt velocity, large weld pool and poor thermal conductivity, then the convective effects, i.e., the liquid metal circulation in the weld pool, markedly affects the weld pool geometry. In contrast, when Pe is small, i.e., much less than unity, the heat transport within the weld pool occurs primarily by conduction [1,10].

2.1.3.3 Order of Magnitude of the Maximum Velocity in the Weld Pool

When the surface tension force is the dominant driving force for convection in the weld pool, the order of the maximal velocity can be approximated by [1]:

$$u_m^{3/2} \approx \frac{d\gamma}{dT}\frac{dT}{dy}\frac{W^{1/2}}{0.664\rho^{1/2}\mu^{1/2}} \tag{2.12}$$

where dT/dy is the average temperature gradient in the weld pool, and W is the weld pool radius.

If the surface tension gradient is not considered and the buoyancy force is the only driving force for the liquid convection, an order of magnitude of the maximum velocity is given by [18]:

$$u_m = \sqrt{g\beta\Delta T D} \tag{2.13}$$

where D is the pool depth.

The foregoing dimensional analysis provides insights about the weld pool development during laser welding. It should be noted that these order of magnitude analyses cannot provide accurate and detailed information about the welding processes, which requires numerical calculation with very fine grids and small time steps.

2.1.4 Temperature and Velocity Fields

Temperature and velocity fields are very important parameters because they determine final weld pool geometry, microstructure, composition and weldment properties. Experimental measurements of temperature and velocity fields during laser spot welding are difficult to obtain because of the insufficient time for measurement and the highly transient nature of the welding process. In addition, the weld pool is often covered by a metal vapor plume. Because of these difficulties, few techniques have been developed to date to measure temperature and velocity fields in the weld pool during laser welding.

Schauer *et al*. [11] measured the temperature distribution in the keyhole during electron beam welding of several aluminum alloys, three steels and tantalum, using a narrow band infrared radiation pyrometer. It was shown that the peak temperature was the lowest for aluminum alloy welds and the highest for tantalum welds. Heiple and Roper [19] estimated the surface flow velocity of the GTA weld pool by measuring the motion of particles using a high-speed camera. They found that the velocities were in the range of 0.5 to 1.4 m/s, with an average value of 0.94 m/s. Kraus [20] obtained surface temperature profiles for GTA welding of some steels, using a non-contact laser reflectance measurement technique. The "measurement" of pool temperature involved extrapolation of temperature versus time data after the arc was totally extinguished based on the perceived transient temperature profile prior to this time period.

It is fair to say that reliable techniques for real time temperature measurement are still evolving. In the absence of adequate experimental work, numerical simulation of convective heat flow field has been relied on to obtain the information of temperature and velocity fields. In recent decades, numerical calculations of heat transfer and fluid flow have been utilized to understand the evolution of temperature and velocity fields. Such a computationally intensive investigation, requiring use of fine grids and very small time steps, has now become practical because of recent advances in the computational hardware and software. Zhang *et al*. [21] calculated the evolution of temperature and velocity fields during gas tungsten arc spot welding of AISI 1005 steel. They found the peak temperature in the weld pool to be about 2100 K and the maximum liquid velocity to be around 100 mm/s.

Several models have been developed to predict the temperature and velocity fields in the weld pool during laser welding [22-30]. Kou and Wang [22] simulated the three-dimensional convection during CO_2 laser welding of 6061 aluminum alloy and obtained a maximum flow velocity of 3000 mm/s and a maximum temperature of 2273 K under the conditions that CO_2 laser power is 1.3 kW and welding speed is 4.23 mm/s. The calculated and observed fusion boundaries were compared and very good agreement was obtained. Mundra and DebRoy [23] obtained the maximum liquid radial velocity in the order of 0.9 m/s during CO_2 laser welding of high-manganese 201 stainless steel.

Cline and Anthony [24] studied the effects of laser spot size, velocity and power level on the temperature distribution, cooling rate and depth of melting of 304 stainless steel. However, the convection in the weld pool was not considered in the model. Mazumder and Steen [25] developed a numerical model of the continuous laser welding process considering heat conduction. Frewin and Scott [26] used a finite element model of the heat flow during pulsed laser beam welding. The transient temperature profiles and the dimensions of the fusion zone and HAZ were calculated. Katayama and Mizutani [27] developed a heat conduction and solidification model considering the effects of microsegregation and latent heat. Recently, Chang and Na [28] applied the finite element method and neural network to study laser spot welding of 304 stainless steel. This combined model could be effectively applied for the prediction of bead shapes of laser spot welding. In summary, transport phenomena based numerical models have been successful in revealing special features for temperature and velocity fields in laser welding processes.

In laser processing of metals and alloys, the temperatures reached on the surface of the material often exceed the boiling point of the material [23,31-33]. von Allmen [31] determined molten pool temperatures in excess of boiling point for laser treatment of copper. Chan and Mazumder [32] also reported temperatures greater than boiling point for the laser irradiation of aluminum, titanium and a superalloy. Khan and DebRoy [33] indicated that the liquid pool surface temperatures were close to the boiling point. Mundra and DebRoy [23] simulated the temperature profile in carbon dioxide laser-welded stainless steels. They determined that the peak temperatures in the weld pool were higher than the boiling point of stainless steel under various welding conditions. In such situations, significant vaporization takes place from the weld pool surface, which will be discussed in next section.

2.2 Vaporization from the Weld Pool Surface

As stated in last section**,** in laser processing of metals and alloys, the temperatures reached on the surface of the material often exceed the boiling point of the metal. The pressures at the weld pool surface can be greater than the ambient pressure. This excess pressure provides a driving force for the vaporization. The vaporization of alloying elements has great effects on the final weld metal composition and mechanical properties.

2.2.1 Effects of Vaporization of Alloying Elements

2.2.1.1 Weld Metal Composition Change

During high energy laser beam welding of important engineering alloys, the metal in the weld pool can be heated to very high temperatures, and significant vaporization of volatile alloying elements often takes place from the weld pool surface [**23**,**33**,**34**-**41**]. The loss of alloying elements can result in a change in the composition of the weld metal, cause changes in the microstructure and degradation of mechanical properties of weldments, and is a serious problem in the welding of many important engineering alloys [**23**,**33**,**38**-**40**].

Blake and Mazumder [**37**] reported the loss of magnesium during laser welding of aluminum alloy 5083. Moon and Metzbower [**38**] investigated the change of composition of aluminum alloy before and after welding of aluminum alloy 5456 using a CO_2 laser with a helium gas shield. Cieslak and Fuerschbach [**39**] observed substantial magnesium vaporization during laser welding of aluminum alloys 6061, 5456 and 5086. The extent of vaporization was a function of the welding speed. It was shown that approximately 20% of the magnesium was lost during welding. Zhao and DebRoy [**40**] investigated the weld metal composition change of aluminum alloy 5182 during laser welding through experiments and computer modeling. It was found that the vaporization rate of magnesium was about two orders of magnitude greater than that of aluminum. The significant magnesium loss from the weld pool resulted in a lower magnesium concentration in the weld metal than was present in the base metal.

Several studies have also been carried out to investigate the vaporization loss from stainless steels. The weld metal composition changes of various grades of high-manganese stainless steels are indicated in Fig. **2.4**. The concentration of manganese in the base metal and weld zone, determined by electron probe microanalyses, is plotted as a function of distance. The severe depletion of manganese in the weld zone in each case is clearly evident. By in-situ monitoring of the alloying elements in the vapor phase by optical emission spectroscopy, it was found that the vapor consisted primarily of iron, manganese, chromium and nickel [**35**,**42**,**43**].

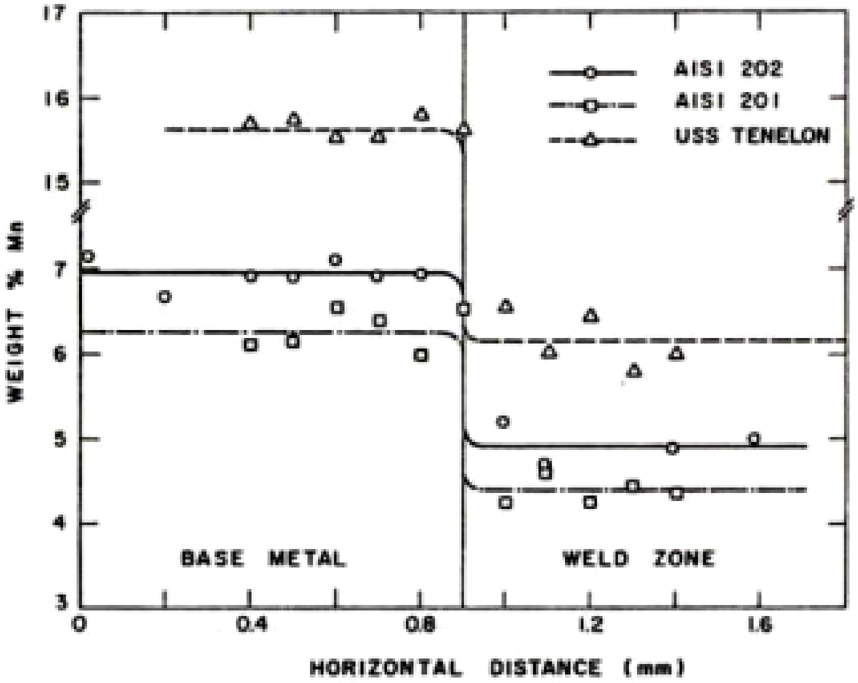

Fig. 2.4: Concentration profile of manganese in the weld zone and base metal for continuous wave carbon dioxide laser welding for AISI 201, AISI 202, and USS Tenelon stainless steels. Laser power: 560 W, welding speed: 3.5×10^{-3} m/s [41].

2.2.1.2 Mechanical Properties

It is fairly well documented that the changes in the composition of the weld metal due to vaporization of alloying elements can significantly affect the weld structure and properties of weldments. Blake and Mazumder [37] found that the loss of magnesium during CO_2 laser welding of aluminum alloy 5083 can result in reduced tensile strength. Moon and Metzbower [38] investigated the change of properties of aluminum alloy before and after welding using a CO_2 laser with a helium gas shield. In their experiments, a reduction of magnesium content from 5% in the base metal to 4% in the fusion zone was observed. They found that the tensile properties of the welds were inferior to the base metal, mainly because of magnesium depletion, loss of strain hardened structure, and porosity. Cieslak and Fuerschbach [39] investigated the property change of aluminum alloys 5456 and 5086. They found that the hardness of weld metal was lower than the base metal due to the magnesium vaporization. The loss of hardness was attributed to a reduction in the solid solution strengthening effect as a result of lower magnesium concentration. The correlation between the yield strength, tensile elongation and magnesium content for most of the common Al-Mg commercial alloys is shown in Fig. 2.5 [44]. It is observed that the tensile strengths of these alloys increase linearly with magnesium content. Due to its high vapor pressure and low boiling point, magnesium can be easily vaporized during laser welding, leading to reduction in the tensile strength of the weldments.

Denney and Metzbower [45] investigated the effects of laser welding on the mechanical properties of high strength low alloy steel A710/736. They found that there was a decrease in both the yield strength and the percent elongation in the welded specimen. Much of the strength and toughness of the A710/736 was a result of precipitates formed during solidification. Since these steels contain about 1.25% manganese, laser welding could cause a loss of manganese and, thus, a reduction in precipitation hardening and degradation of properties.

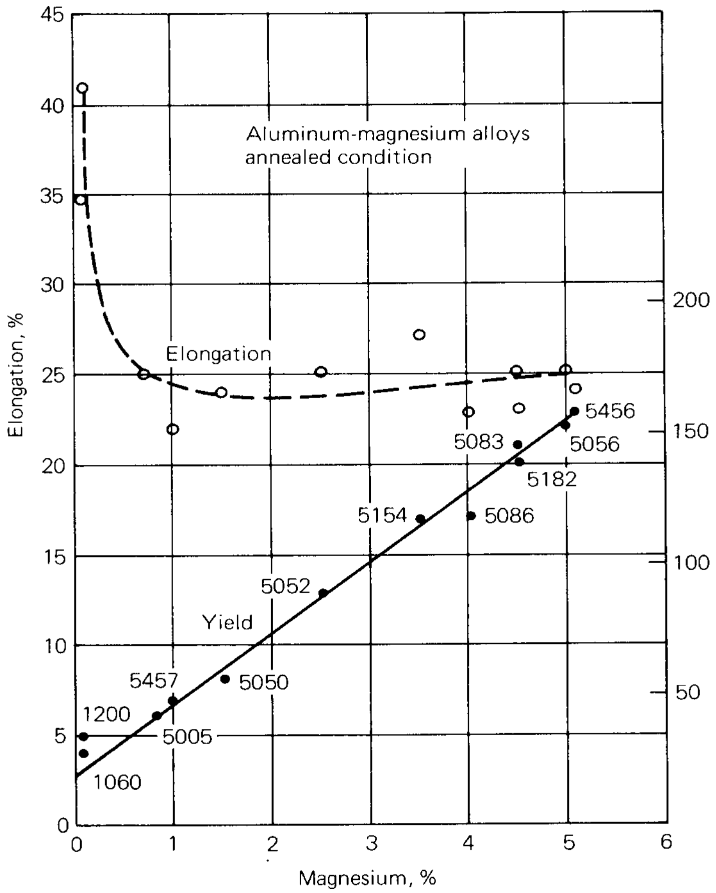

Fig. 2.5: Correlation between tensile yield and elongation and magnesium content for some commercial alloys [44].

2.2.2 Factors Affecting Vaporization

2.2.2.1 Weld Pool Temperature Distribution

Since partial pressures of vaporizing elements depend strongly on temperature, the rates of vaporization of various alloying elements from the weld pool are strongly dependent on the temperature distribution at the weld pool surface. The experimental data for equilibrium vapor pressures of various elements as a function of temperature are given in Fig. **2.6.** From this Figure, for the elements in stainless steel, manganese has the highest vapor pressure compared with that of iron and nickel. At around 1500 K, manganese has a vapor pressure of 1.3×10^{-3} atm. However, the vapor pressure of manganese increases by about two orders of magnitude to 0.13 atm when the temperature is increased to 2000 K.

2.2.2.2 Plasma

The presence of a plasma may have a significant effect on the vaporization rate of weld metal. Collar *et al*. [**41**] and Sahoo *et al*. [**47**] found that the presence of a plasma reduced the vaporization rate by about 10% to 50% for iron and about 60% to 80% for copper. The reduction in the vaporization rates was considered to be consistent with the enhanced condensation of metal vapor due to a space charge effect [**47**]. Fig. **2.7**(a) shows the effect of plasma on vaporization flux. It is observed that plasma lowers the vaporization rate significantly. In the plasma, both the excited neutral and the ionized metal and shielding gas species are present along with free electrons. In view of the high mobility of the electrons among the various species in the plasma, the surface of the metal becomes negatively charged since the electrons strike the metal surface at a faster rate than the ions, as shown in Fig. **2.7**(b). The attraction between the positively charged ions and the negatively charged surface leads to high condensation rates and, consequently, low vaporization rates in the presence of the plasma [**47**].

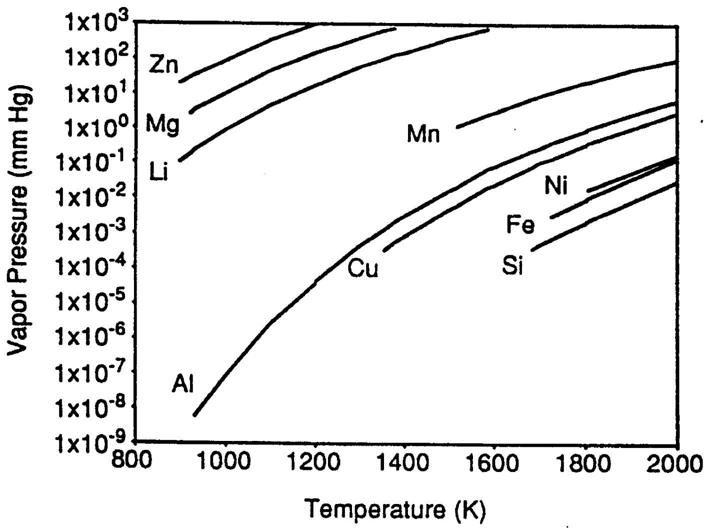

Fig. 2.6: Type Equilibrium vapor pressure as a function of temperature for various elements [46].

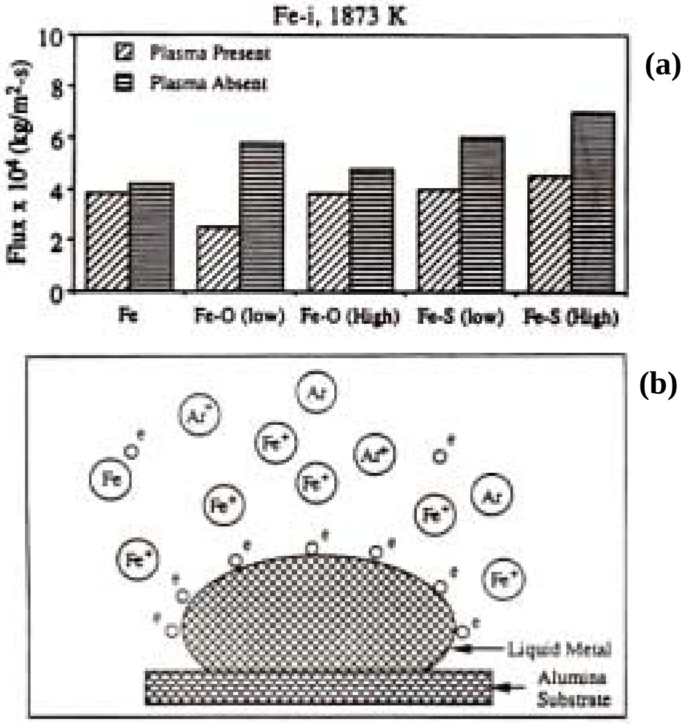

Fig. 2.7: (a) Vaporization flux for controlled laboratory experiments with metal drops in the presence and absence of plasma, and (b) schematic representation of the space charge effect [47].

2.2.2.3 Surface Active Alloying Elements

The presence of surface-active elements such as oxygen and sulfur can influence the rate of vaporization. It is possible that these elements block a portion of the liquid metal surface and reduce the vaporization rate [41]. They can also alter the temperature coefficient of surface tension, $\partial\gamma/\partial T$, where γ is the surface tension, and T is the temperature, as shown in Equation 2.6. As a result, they can affect the weld pool surface area and the temperature distribution [16,19], which in turn strongly influences the vaporization rates. Sahoo *et al*. [47] found that the presence of surface active elements in iron resulted in increased vaporization rates of the metals in their isotheral vaporization experiments, as shown in Fig. 2.7(a). One of the possible opposing effects could be the effect of interfacial turbulence [48] caused by the movements of surface active elements from inside to the surface of the liquid. The local movements of the interface increase surface area and, therefore, increase the rate of vaporization.

2.2.2.4 Welding Parameters

The most important laser welding parameters which influence the rate of vaporization are the factors which control the heat input. The temperature and the surface area of the molten pool depend on the energy input and its distribution, which in turn are influenced by the laser power, beam radius and welding speed. Therefore, laser power density and welding speed are the important process parameters which control the vaporization rate. The effect of laser power and welding speed on the vaporization rate has been investigated intensively on the laser welding for aluminum [40] and stainless steel [23,33,41]. In addition, the type and flow rate of the shielding gas also influence the vaporization rate. The diffusivities of the vaporizing species in the various shielding gases are different, and the flow rate of the shielding gas influences the mass transfer coefficient. Therefore, these two factors are also expected to have an influence on the rate of vaporization. Collar *et al*. [41] examined the effect of gas flow rate on the vaporization rate in helium, nitrogen and argon shielding gases, respectively. It was found that the vaporization rate was insensitive to changes in the diffusivity of the vaporizing species and flow rate, indicating that the gas phase mass transfer step did not contribute significantly to the overall vaporization rate.

2.3 Calculation of Vaporization Rate

A simple model for calculation of the vaporization flux of a pure metal in a vacuum is given by the Langmuir equation [49]:

$$J_i = \frac{P_i^0}{\sqrt{2\pi M_i RT}} \qquad (2.14)$$

where J_i is the vaporization flux of the element i, P_i^0 is the vapor pressure of i over the pure liquid, M_i is molecular weight of the vaporizing element i, R is the gas constant and T is the temperature. This equation shows that the vaporization rate is proportional to the equilibrium vapor pressure of the vaporizing element. For an alloy, the vaporization rate of each alloying element can be calculated separately. The overall vaporization rate of the alloy is the sum of the vaporization rates of all alloying elements. Assuming that the alloy is ideal at high temperatures, the equilibrium vapor pressures of the various species over the alloy can be expressed as:

$$P_i = X_i P_i^0 \qquad (2.15)$$

where X_i is the mole fraction of element i in the alloy.

Langmuir equation is accurate only at very low pressures where significant condensation of the vapor does not take place. As a result, when welding is conducted at one atmosphere, Equation 2.14 predicts a much higher vaporization rate than actually exists under the conditions. Mundra and DebRoy [23] compared the vaporization rate calculated from the Langmuir equation with experimentally determined values. It was found that the vaporization rate calculated from the Langmuir equation was significantly higher than the experimental value. However, the equation is useful in calculating the relative vaporization rates of alloying elements, as was previously indicated by the work of Block-Bolten and Eager [34].

Because the Langmuir equation overestimates vaporization rate, more comprehensive models have been tried to understand the vaporization of weld metal quantitatively. Aden *et al.* [50] investigated the laser-induced vaporization from steel and aluminum surfaces as a function of laser intensity and material properties. A material-dependent minimum laser intensity above which no further expansion of the metal vapor occurs was discussed. However, the model did not take into account the flow of liquid metal in the weld pool nor the detailed heat transfer in the weldment. Also, a theoretical model was developed by Dilthey *et al.* [51] to describe the vaporization of alloying elements during laser welding. Two important processes were analyzed: the diffusion of alloying elements from the interior to the weld surface and their subsequent vaporization from the weld pool surface. Both of the models ignored the condensation of the metal vapor. Anisimov [52] and Knight [53] derived expressions for the vapor temperature, density, velocity and the extent of condensation by solving the equations of conservation of mass, momentum and energy in a thin layer adjacent to the liquid-vapor interface, known as the Knudsen layer. Their approach has been incorporated into vaporization models [23,40] to calculate the laser-induced vaporization rate in this thesis.

2.4 Liquid Metal Expulsion

Pronounced vaporization of metal vapors from the weld pool surface occurs when very high power-density energy sources such as laser and electron beams are used for welding [23,][33-41]. If the weld pool temperatures are very high, the escaping vapor exerts a large recoil force on the weld pool surface and, as a consequence, liquid metal droplets may be expelled from the weld pool. There are two main mechanisms of removal of material for laser processing. One is vaporization which occurs in conduction mode laser welding; another is liquid metal expulsion by the vaporization–induced recoil pressure common in cutting, welding and drilling. Since the latent heat of vaporization does not need to be absorbed when liquid metal expulsion occurs, it is a very effective mechanism of material removal. The energy required to remove material by liquid metal expulsion is about one-quarter of that required to vaporize the same volume [54]. In some materials processing operations, such as laser drilling or cutting, liquid metal expulsion is desirable. On the other hand, liquid expulsion can result in irregular, asymmetric and poorly controlled hole dimensions. For several important metal processing operations such as welding, surface alloying and cladding, besides the poor liquid pool shape, the metal loss can adversely affect the weld geometry and weldment properties, so weld metal expulsion is undesirable. Therefore, it is important to understand various factors that affect liquid metal expulsion during high-power laser beam welding.

Most of the previous work on liquid metal expulsion focused on laser drilling. Voisey, Cheng and Clyne [54,55] found that the extent to which liquid expulsion occurs depends both on materials properties and laser parameters. Two complementary methods, high-speed photography and a particle stream interruption technique, were used to determine the ejection velocity. It was shown that increasing the pulse density increased the ejection velocity. The typical particle diameters appeared to be of the order of the molten layer thickness during drilling. Lu, Zheng and Song [56] developed a method to “capture” the particles ejected from the substrate due to laser irradiation. They found that the particles from a smooth substrate concentrated mostly on the center of the capturing surface, while those from a rough surface were ejected in more random directions. Yilbas [57] investigated the propagation velocity of the liquid-vapor interface during laser-metal interaction using a special photographic technique for four metals: titanium, tantalum, nickel and EN58B stainless steel. It was found that the particle velocity at a given laser output energy increased with the decrease in the thermal diffusivity of the material, and particle velocity increased with increase in laser energy. In experiments conducted by Chun and Rose [58] in which an aluminum target was irradiated by 30 kW laser pulse, it was observed that the fraction of material removed as liquid from the weld pool rose to 90% as pulse length was increase to 200 milliseconds. The fraction of material lost as liquid depends on laser pulse characteristics like average power density, pulse duration and peak power. It also depends on material constants like thermal conductivity, difference between melting and boiling points, and ratio of latent heats of vaporization and melting. Rodden *et al*. [**59**] measured the percentage of mass removed as liquid metal expulsion to be 90% for titanium during single pulse Nd:YAG laser drilling. High-speed photographs indicated that there were two distinct stages of liquid metal expulsion during drilling with a pulsed laser. There was an initial expulsion of small liquid particles, followed by the expulsion of larger particles of liquid near the end of the pulse.

Liquid metal expulsion has also been studied theoretically. von Allmen [**31**] suggested that vapor pressure acts like a piston that exerts a pressure onto the melt, squirting it out of the melt pool radially. He also developed a theoretical model to calculate drilling velocity and drilling efficiency as a function of the absorbed intensity [**60**]. Chan and Mazumder [**32**] developed a one-dimensional steady state model to describe the laser-induced damage caused by materials removal through vaporization and liquid metal expulsion. Results were obtained for three materials: aluminum, superalloy and titanium. For the power levels investigated, the material-removal rates were of the order of 1 m/s and increased with heat-flux intensity. Depending on the materials and beam power density, either vaporization or liquid expulsion was thought to be the dominant mechanism of material removal. Semak *et al*. [**61**] assumed that keyhole propagation was dominated by evaporation-recoil-driven melt expulsion from the beam interaction zone. Additionally, the role of recoil pressure in energy balance during laser material processing was analyzed theoretically by Semak *et al*. [**62**]. Basu and DebRoy [**63**] examined the conditions for the initiation of liquid metal expulsion during laser irradiation experimentally and theoretically. They proposed that liquid metal expulsion takes place when the vapor recoil force exceeds the surface tension force of the liquid metal at the periphery of the weld pool.

For laser welding, liquid metal expulsion is not desirable, especially for very small length scale, where the operation is often carried out in a clean room environment after the components have undergone significant prior processing.

2.5 References

1. T. DebRoy and S. A. David, *Rev. Mod. Phys.*, **67**, 85 (1995).
2. P. W. Fuerschbach, *Weld. J.*, **75**, 24s (1996).
3. J. Xie and A. Kar, *Weld. J.*, **78**, 343s (1999).
4. W. W. Duley, *Laser Welding* (New York: John Wiley & Sons, Inc, 1999).
5. D. A. Cremers, G. K. Lewis and D. R. Korzekwa, *Weld. J.* **70**, 159s (1991).
6. P. W. Fuerschbach and G. R. Eisler, *Sci. Technol. Weld. Joining*, **7**, 241 (2002).
7. W. Pitscheneder, *Ph. D thesis*, The University of Leoben, 2001.
8. J. F. Ready, *LIA Handbook of Laser Materials Processing* (Orlando: Magnolia Publishing, 2001).
9. M. A. Bramson, *Infrared Radiation: a Handbook for Applications* (New York: Plenum Press, 1968).
10. S. Kou, *Welding Metallurgy*, (New Jersey: John Wiley & Sons, 2003).
11. D. A. Schauer, W. H. Giedt and S. M. Shintaku, *Weld. J.*, **57**, 127s (1978).
12. K. Easterling, *Introduction to the Physical Metallurgy of Welding* (Oxford: Butterworth-Heinemann, 1992).
13. Ø. Grong, *Metallurgical Modeling of Welding*, (London: The Institute of Materials, 1997).
14. K. Mundra, T. DebRoy and K. Kelkar, *Numer. Heat Transfer A*, **29**, 115 (1996).
15. S. Kou and Y. H. Wang, *Metall. Trans. A*, **17A**, 2271 (1986).
16. P. Sahoo, T. DebRoy and M. J. McNallan, *Metall. Trans. B*, **19B**, 483 (1988).
17. Z. Yang, *Ph. D. thesis*, The Pennsylvania State University, 2000.
18. G. M. Oreper and J. Szekely, *Metall. Trans. A*, **18A**, 1325 (1987).

19. C. R. Heiple and J. R.Roper, in *Trends in welding research in the United States: proceedings of a conference*, edited by S. A. David (Metals Park: American Society for Metals, 1982).

20. H. G. Kraus, *Weld. J.*, **68**, 269s (1989).

21. W. Zhang, G. G. Roy, J. W. Elmer and T. DebRoy, *J. Appl. Phys.*, **93**, 3022 (2003).

22. S. Kou and Y. H. Wang, *Metall. Trans. A*, **17A**, 2265 (1986).

23. K. Mundra and T. DebRoy, *Metall. Trans. B*, **24B**, 145 (1993).

24. H. E. Cline and T. R. Anthony, *J. Appl. Phys.*, **48**, 3895 (1977).

25. J. Mazumder and W. M. Steen, *J. Appl. Phys.*, **51**, 941 (1980).

26. M. R. Frewin and D. A. Scott *Weld. J.*, **78**, 15s (1999).

27. S. Katayama, M. Mizutani and A. Matsunawa, *Sci. Technol. Weld. Joining*, **2**, 1 (1997).

28. W. S. Chang and S. J. Na, *Metall. Trans. B*, **32B**, 723 (2001).

29. G. M. Oreper, J. Szekely and T. W. Eager, *Metall. Trans. B*, **17B**, 735 (1986).

30. L. A. Betram, *J. Eng. Mater. Technol.*, **115**, 24 (1993).

31. M. von Allmen, *Laser-beam Interactions with Materials*, (New York: Springer Verlag, 1987).

32. C. L. Chan and J. Mazumder, *J. Appl. Phys.*, **62**, 4579 (1987).

33. P. A. A. Khan and T. DebRoy, *Metall. Trans. B*, **15B**, 641 (1984).

34. A. Block-Bolten and T. W. Eager, *Metall. Trans. B*, **15B**, 461 (1984).

35. G. J. Dunn, C.D. Allemand and T. W. Eagar, *Metall. Trans. A*, **17A**, 1851 (1986).

36. G. J. Dunn and T. W. Eagar, *Metall. Trans. A*, **17A**, 1865 (1986).

37. A. Blake and J. Mazumder, *J. Eng. Ind.*, **107**, 275 (1985).

38. D. W. Moon and E. A. Metzbower, *Weld. J.*, **62**, 53s (1983).

39. M. J. Cieslak and P. W. Fuerschbach, *Metall. Trans. B* **19B**, 319 (1988).

40. H. Zhao and T. DebRoy, *Metall. Trans. B*, **32B**, 163 (2001).

41. M. M. Collur, A. Paul and T. DebRoy, *Metall. Trans. B*, **18B**, 733 (1987).

42. M. M. Collur and T. DebRoy, *Metall. Trans. B*, **20B**, 277 (1989).

43. R. Miller and T. DebRoy, *J. appl. Phys.*, 68, 2045 (1990).

44. L. R. Morris, R. Iricibar, J. D. Embury and J. L. Duncan, in *Aluminum Transformation Technology and Applications*, edited by C. A. Pampillo, H. Biloni, L. F. Mondolfo and F. Sacchi (Metals Park: American Society for Metals, 1982)

45. P. E. Denney and E. A. Metzbower, in *International Congress on the Applications of Lasers and Electro-optics* (Los Angeles: Laser Institute of America, 1983).

46. T. Iida, *The Physical Properties of Liquid Metals* (Oxford: clarendon Press, 1993).

47. P. Sahoo, M. M. Collar and T. DebRoy, *Metall. Trans. B*, **19B**, 967 (1988).

48. F. D. Richardson, Physical Chemistry of Melts in Metallurgy (Academic Press, 1974).

49. S. Dushman, *Scientific Foundations of Vacuum Technique* (New York: Wiley, 1962).

50. M. Aden, E. Beyer, G. Herziger and H. Kunze, *J. of Phys. D: Appl. Phys.*, **25**, 57 (1992).

51. U. Dilthey, A. Goumeniouk, V. Lopota, G. Turichin and E. Valdaitseva, *J. of Phys. D: Appl. Phys.*, **34**, 81 (2001).

52. S. I. Anisimov and A. Kh Rakhmatulina, *Soviet Physics – JETP*, **37**, 441 (1973).

53. C. J. Knight, *AIAA J.*, **17**, 519 (1979).

54. K. T. Voisey, C. F. Cheng and T. W. Clyne, in *Laser-solid Interactions for Materials Processing*, edited by D. Kumar (San Francisco: Materials Research Society, 2001) pJ5.6.1.

55. K. T. Voisey, S. S. Kudesia, W. S. O. Rodden, D. P. Hand, J. D. C. Jones and T. W. Clyne, *Mater. Sci. Eng. A*, **356**, 414 (2003).

56. Y. F. Lu, Y. W. Zheng and W. D. Song *J. Appl. Phys.*, **87**, 549 (2000).

57. B. S. Yilbas, *J. Laser Appl.*, **7**,147 (1995).

58. M. K. Chun and K. Rose, *J. Appl. Phys.*, **11**, 614 (1970).

59. W. S. O. Rodden, P. Solana, S. S. Kudesia, D. P. Hand, P. Kapadia, J. Kowden and J. D. C. Jones, in *International Congress on Applications of Lasers and Electro-optics* (San Diego: Laser Institute of American, 1999).

60. M. von Allmen, *J. Appl. Phys.,* **47**, 5460 (1976).

61. V. V. Semak, W. D. Bragg, B. Damkroger and S. Kempka, *J. Phy. D: Appl. Phys.*, **32**, L61 (1999).

62. V. V. Semak and A. Matsunawa, *J. Phy. D: Appl. Phys.*, **30**, 2541 (1997).

63. S. Basu and T. DebRoy, *J. Appl. Phys.*, **72** 3317 (1992).

Chapter 3

MATHEMATICAL MODELS

In this chapter, the models used in the present study: a three-dimensional heat transfer and fluid flow model, and a model for the calculation of vaporization, are described.

3.1 Heat Transfer and Fluid Flow Model

As discussed previously, direct experimental measurement of various physical processes during welding is very difficult. A practical recourse is to utilize transport phenomena based models to accurately calculate the temperature and velocity fields in the weld pool. These transport phenomena based models involve the numerical solution of governing conservation equations including the mass, momentum and energy conservation equations.

3.1.1 Governing Equations

The numerical solution of heat transfer, fluid flow and other related processes can begin with the mathematical forms in which the physical laws governing these processes have been expressed. The mathematical forms of the transport processes are often expressed as differential equations, which define certain conservation principles. Each equation employs a certain physical quantity as its dependent variable and implies that there must be a balance among the various factors that influence the variable [1]. Examples of the physical quantity are mass, velocity and enthalpy. If the dependent variable is denoted by ϕ, the general differential equation is given as:

$$\rho\frac{\partial\phi}{\partial t}+\rho\frac{\partial(u_i\phi)}{\partial x_i}=\frac{\partial}{\partial x_i}\left(\Gamma\frac{\partial\phi}{\partial x_i}\right)+S \tag{3.1}$$

where ρ is the density, t is the time, u_i is the liquid velocity along i direction, Γ is the general diffusion coefficient, and S is the source term, which includes all effects that are not included in the other three terms. For example, S may include forces acting on the fluid elements, such as the buoyancy force. The quantities Γ and S are specific to a particular meaning of ϕ. For instance, if ϕ denotes a velocity component, Γ is then the viscosity of the liquid, and S has the unit of force per unit volume. The four terms in Equation 2.1 are the unsteady term, the convection term, the diffusion term and the source term [1].

The conservation equations of mass, momentum and energy can be expressed as:

$$\frac{\partial\rho}{\partial t}+\frac{\partial(\rho u_i)}{\partial x_i}=0 \tag{3.2}$$

$$\frac{\partial(\rho u_j)}{\partial t}+\frac{\partial(\rho u_i u_j)}{\partial x_i}=\frac{\partial}{\partial x_i}\left(\mu\frac{\partial u_j}{\partial x_i}\right)+S_{ui} \tag{3.3}$$

$$\frac{\partial(\rho h)}{\partial t}+\frac{\partial(\rho u_i h)}{\partial x_i}=\frac{\partial}{\partial x_i}\left(\frac{k}{C_p}\frac{\partial h}{\partial x_i}\right)+S_h \tag{3.4}$$

where μ is the effective viscosity, k is the thermal conductivity, and C_p is the specific heat. The source terms S_{ui} and S_h are given as:

$$S_{ui}=-\frac{\partial p}{\partial x_i}+\frac{\partial}{\partial x_j}\left(\mu\frac{\partial u_j}{\partial x_i}\right)-V\frac{\partial(\rho u_i)}{\partial x_i}-C\left(\frac{(1-f_l)^2}{f_l^{\,3}+B}\right)u_i+\rho g\beta(T-T_{ref}) \tag{3.5}$$

$$S_h=-\frac{\partial(\rho\Delta H)}{\partial t}-\frac{\partial(\rho u_i\Delta H)}{\partial x_i}-V\frac{\partial(\rho h)}{\partial x_i}-V\frac{\partial(\rho\Delta H)}{\partial x_i} \tag{3.6}$$

where p is the pressure, V is the welding speed, f_l is the liquid fraction, B is a very small positive constant introduced to avoid division by zero, C is a constant that takes into account mushy zone morphology [2], β is the coefficient of volume expansion, and T_{ref} is a reference temperature.

In order to trace the weld pool liquid/solid interface, i.e., the phase change, the total enthalpy H is represented by a sum of sensible heat h and latent heat content ΔH, i.e., $H = h + \Delta H$ [2,3]. The sensible heat h is expressed as $h = \int C_p dT$. The latent heat content ΔH is given as $\Delta H = f_L L$, where L is the latent heat of fusion. The liquid fraction f_L is assumed to vary linearly with temperature [4]:

$$f_L = \begin{cases} 1 & \text{for} \quad T > T_{Lt} \\ \dfrac{T - T_S}{T_L - T_S} & \text{for} \quad T_S < T \le T_L \\ 0 & \text{for} \quad T \ge T_S \end{cases} \tag{3.7}$$

where T_L and T_S are the liquidus and solidus temperatures, respectively. After obtaining the values of the sensible enthalpy, h, on the computational domain, temperature can be expressed as:

$$T = \begin{cases} T_{solid} + \dfrac{h - H_{melt}}{C_{ps}} & \text{for} \quad h \le H_{melt} \\ T_{solid} + \dfrac{h - H_{melt}}{C_{pa}} = T_{solid} + \dfrac{h - H_{melt}}{H_{cal} - H_{melt}}\left(T_{liquid} - T_{solid}\right) & \\ \qquad\qquad\qquad\quad = T_{solid} + f_l \times \left(T_{liquid} - T_{solid}\right) & \\ & \text{for} \quad H_{melt} < h < H_{cal} \\ T_{liquid} + \dfrac{h - H_{cal}}{C_{pl}} & \text{for} \quad h \ge H_{cal} \end{cases} \tag{3.8}$$

where H_{melt} is the total enthalpy at the liquidus temperature, C_{ps} and C_{pl} are the specific heats of solid and liquid, respectively. The specific heat, C_{pa}, in the mushy zone was calculated by:

$$C_{pa} = (C_{ps} + C_{pl}) / 2 \tag{3.9}$$

H_{cal} is given as:

$$H_{cal} = H_{melt} + C_{pa} \times (T_{liquid} - T_{solid}) \tag{3.10}$$

3.1.2 Boundary Conditions

Because of the axisymmetric nature of spot welding, the governing equations can be solved in a two-dimensional system. However, laser welding with a moving heat source is also investigated here, which is a three-dimensional problem. So the same three-dimensional heat transfer and fluid flow model is used in the calculation. Only half of the workpiece is considered since the weld is symmetrical about the weld center line.

3.1.2.1 Top Surface

The weld top surface is assumed to be flat. The velocity boundary condition is give as [5]:

$$\begin{aligned} \mu\frac{du}{dz} &= f_l\frac{d\gamma}{dT}\frac{dT}{dx} \\ \mu\frac{dv}{dz} &= f_l\frac{d\gamma}{dT}\frac{dT}{dy} \\ w &= 0 \end{aligned} \qquad (3.11)$$

where u, v and w are the velocity components along x, y and z directions, respectively, $\frac{d\gamma}{dT}$ is the temperature coefficient of surface tension. As shown in this equation, the u and v velocities are determined from the Marangoni effect. The w velocity is equal to zero since there is no flow of liquid metal perpendicular to the pool top surface.

The heat flux at the top surface is given as:

$$k\frac{\partial T}{\partial z} = \frac{fQ\eta}{\pi r_b^2}\exp\left(-\frac{f\left(x^2+y^2\right)}{r_b^2}\right) - \sigma\varepsilon\left(T_4 - T_a^4\right) - h_c\left(T - T_a\right) \qquad (3.12)$$

where Q is the laser power, η is the absorption coefficient, r_b is the beam radius, σ is the Stefan-Boltzmann constant, h_c is the heat transfer coefficient, T_a is the ambient temperature, and f is the heat distribution factor. For laser welding, distribution factor f is taken as 3.0 [6]. The first term on the right hand side is the heat input from the heat source, which is assumed to have Gaussian distribution [7]. The second and third terms represent the heat loss by radiation and convection, respectively. The reported values of the absorption coefficient vary significantly [8-9]. For example, Cremers, Lewis and Korzekwa [8] indicated the absorption coefficient of Nd:YAG laser in 316 stainless steel to be in the range of 0.21 to 0.62. The absorption coefficient has been related to the substrate resistivity and the wavelength of the laser radiation by the following relation [9]:

$$\eta(T) = 0.365\left(\frac{\alpha}{\lambda}\right)^{1/2} - 0.0667\left(\frac{\alpha}{\lambda}\right) + 0.006\left(\frac{\alpha}{\lambda}\right)^{3/2} \qquad (3.13)$$

where λ is the wavelength, and α is the electrical resistivity of the materials.

3.1.2.2 Symmetric Surface

The boundary conditions are defined with zero flux across the symmetric surface as:

$$\frac{du}{dy} = 0\,,\ v = 0\,,\ \frac{dw}{dy} = 0 \qquad (3.14)$$

$$\frac{dh}{dy} = 0 \qquad (3.15)$$

3.1.2.3 Other Surfaces

On all other surfaces, temperatures are set at ambient temperature, and the velocities are set to be zero.

3.1.3 Discretization of Governing Equations

The governing equations are discretized using the control volume method, where a rectangular computational domain is divided into small rectangular control volumes. A scalar grid point is located at the center of each control volume, storing the values for scalar variables such as pressure and enthalpy. In order to ensure the stability of numerical calculation, velocity components are arranged on different grid points, staggered with respect to scalar grid points. In other words, velocity components are calculated for the points that lie on the faces of the control volumes. Thus, the control volumes for scalars are different from those for the vectors. Discretized equations for a variable are formulated by integrating the corresponding governing equation over the three dimensional control volumes. The final discretized equation takes the following form [1]:

$$a_P\phi_P = a_E\phi_E + a_W\phi_W + a_N\phi_N + a_S\phi_S + a_T\phi_T + a_B\phi_B + a_P^0\phi_P^0 + S_U\Delta V \qquad (3.16)$$

where subscript P represents a given grid point, while subscripts E, W, N, S, T and B represent the east, west, north, south, top and bottom neighbors of the given grid point P, respectively. The symbol ϕ represents a dependant variable such as velocity or enthalpy, a is the coefficient calculated based on the power law scheme, ΔV is the volume of the control volume, a_P^0 and ϕ_P^0 are the coefficient and value of the dependant variable at the previous time step, respectively. S_U is the constant part of the source term S, which can be expressed as:

$$S = S_U + S_P\phi_P \qquad (3.17)$$

The coefficient a_P is defined as:

$$a_P = a_E + a_W + a_N + a_S + a_T + a_B + a_P^0 + S_P\Delta V \qquad (3.18)$$

The governing equations are then solved iteratively on a line-by-line basis using a Tri-Diagonal Matrix Algorithm (TDMA). The detailed procedure to solve the equations is described in reference [1].

3.1.4 Convergence Criteria

In the present model, two convergence criteria are used: residuals and heat balance. The residuals for velocities and enthalpy are defined as:

$$R = \frac{\sum\limits_{\text{domain}} \left| \frac{\sum\limits_{\text{nb}} (a_{\text{nb}} \phi_{\text{nb}}) + a_P^0 \phi_P^0 + S_U \Delta V}{a_P} - \phi_P \right|}{\sum\limits_{\text{domain}} |\phi_P|} \qquad (3.19)$$

where subscript nb represents the neighbors of the given grid point P. The residual values should be very small when a converged solution is obtained. In addition, the following heat balance criterion for the convergence of the computed temperature profiles is also checked:

$$\theta = \left| \frac{\text{net heat input}}{\text{total heat output} + \text{heat accumulation}} \right| \qquad (3.20)$$

Upon convergence, heat balance ratio θ should be very close to 1. In the present study, the convergence criterion used is $0.999 \leq \theta \leq 1.001$. More restrictive convergence conditions do not change the final results while increasing the computational time significantly.

3.1.5 Calculation of Thermal Cycles

After calculating the steady state temperature field, the weld thermal cycle at any given location (x,y,z) is calculated as:

$$T(x, y, z, t_2) = \frac{T_S(\zeta_2, y, z) - T_S(\zeta_1, y, z)}{\zeta_2 - \zeta_1} V(t_2 - t_1) + T(x, y, z, t_1) \qquad (3.21)$$

where $T(x, y, z, t_2)$ and $T(x, y, z, t_1)$are the temperatures at time t_2 and t_1, respectively, $T_S(\zeta_2, y, z)$ and $T_S(\zeta_1, y, z)$ are the steady-state temperatures at locations (ζ_2, y, z) and

(ζ_1, y, z), respectively, V is the welding speed and $(\zeta_2 - \zeta_1)$ is the length welded in time $(t_2 - t_1)$.

3.2 A Model for the Calculation of Vaporization

During laser welding, the peak temperature of the weld pool can exceed the boiling point of the alloys [12-15]. As a result, the pressures at the weld pool surface are higher than the ambient pressure, and the excess pressure provides a driving force for the vapor to move away from the pool surface. In addition, the concentrations of alloying elements at the pool surface are higher than those in the bulk shielding gas, and the concentration gradient also provides a driving force for the vapor to move away from the pool surface. In the model, the vapor flux of each vapor species is considered to be the sum of two fluxes driven by pressure and concentration gradients.

3.2.1 Vaporization due to Concentration Gradient

On the weld pool surface, the concentrations of the alloying elements in the vapor are higher than those in the bulk shielding gas. The diffusive vaporization flux of element i, J_{ci}, can be defined as:

$$J_{ci} = K_{gi}\left(M_i \frac{a_i P_i^0}{RT_l} - C_i^s\right) \tag{3.22}$$

where K_{gi} is the mass transfer coefficient of element i between the weld pool surface and the shielding gas. Its value is calculated from the graphical results of Schlunder and Gniclinski [16] for a jet impinging on a flat surface and can be expressed by:

$$K_{gi} = \frac{2Sc^{0.42}\,Re^{0.5}\,D_i}{d}\left(1 + \frac{Re^{0.55}}{200}\right)^{0.5}\left[0.483 - 0.108\frac{r}{d} + 7.71x10^{-3}\left(\frac{r}{d}\right)^2\right] \tag{3.23}$$

where M_i is the molecular weight of the element i, a_i is the activity of element i in the liquid metal, P_i^0 is the equilibrium vapor pressure of element i over its pure liquid, R is the gas constant, T_l is the temperature on the weld pool surface and is obtained from the transient heat transfer and fluid flow model, C_i^s is the concentration of element i in the shielding gas, Sc is the Schmidt number, Re is the Reynolds number at the nozzle exit, D_i is the average diffusivity of element i in the shielding gas, d is the diameter of the nozzle, and r is the radial distance cross the weld pool surface.

3.2.2 Vaporization due to Pressure Gradient

During laser welding, the peak temperature reached on the weld pool surface often exceeds the boiling point of the alloy. As a result, the vapor pressure on the weld pool surface can be higher than the ambient pressure, and the excess pressure provides a driving force for the vapor to move away from the surface. Therefore, the convective flux of the vaporized elements as driven by the excess pressure is an important contributor to the overall vaporization flux.

The velocity distribution functions of the vapor molecules, f_1, f_2 and f_3, escaping from the weld pool surface at various locations are shown schematically in Fig. 3.1. On the weld pool surface, the molecules cannot travel in the negative direction, and, as a consequence, the velocity distribution is half-Maxwellian. Close to the weld pool, there exists a space of several molecular mean free paths length, known as the Knudsen layer, at the outer edge of which the velocity distribution just reaches the equilibrium distribution. A portion of the vaporized material condenses on the liquid surface. The rate of condensation will be taken into account in the model.

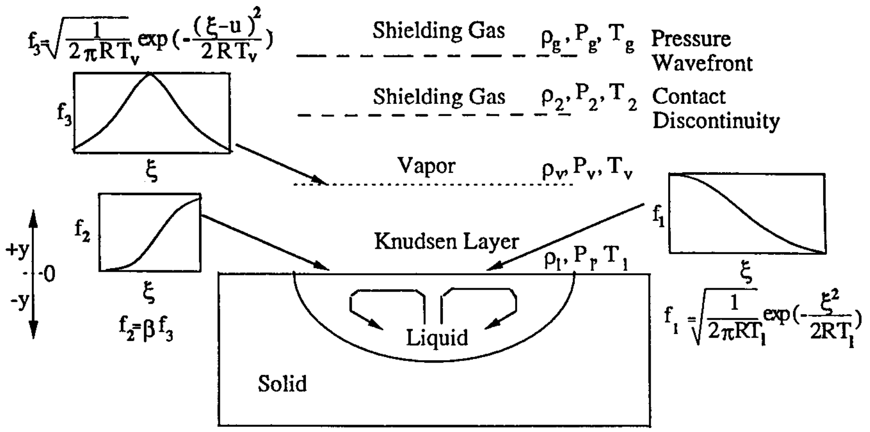

Fig. 3.1: A schematic diagram of the velocity distribution functions in the Knudsen layer and in adjacent regions [17].

The temperature T_v, density ρ_v, pressure P_v and the mean velocity u of the vapor at the edge of the Knudsen layer can be related to temperature T_l, density ρ_l and pressure P_l of the vapor on the liquid surface by treating the Knudsen layer as a gas dynamic discontinuity. Anisimov and Rakhmatulina [18] and knight [19] derived expressions for the vapor temperature, density, velocity and the extent of condensation across the Knudsen layer by solving the equations of conservation of mass, momentum and translational kinetic energy. The derived jump conditions across the Knudsen layer are given by:

$$\frac{T_v}{T_l} = \left[\sqrt{1+\pi\left(\frac{\gamma_v - 1}{\gamma_v + 1}\frac{m}{2}\right)^2} - \sqrt{\pi}\frac{\gamma_v - 1}{\gamma_v + 1}\frac{m}{2}\right]^2 \tag{3.24}$$

$$\frac{\rho_v}{\rho_l} = \sqrt{\frac{T_l}{T_v}}\left[\left(m^2 + \frac{1}{2}\right)e^{m^2}\operatorname{erfc}(m) - \frac{m}{\sqrt{\pi}}\right] + \frac{1}{2}\frac{T_l}{T_v}\left[1 - \sqrt{\pi}me^{m^2}\operatorname{erfc}(m)\right] \tag{3.25}$$

$$\beta = \left[(2m^2+1) - m\sqrt{\pi\frac{T_l}{T_v}}\right]e^{m^2}\frac{\rho_l}{\rho_v}\sqrt{\frac{T_l}{T_v}} \tag{3.26}$$

where $m = u/\sqrt{2R_vT_v}$, $R_v = R/M_v$, R is the gas constant, M_v is the average molecular weight of the vapor, γ_v is the ratio of specific heat of the vapor, which is treated as a monatomic gas, erfc is the complimentary error function, and β is the condensation factor. There are four unknowns in Equation 3.24 through **3.26,** namely, T_v, ρ_v, β and m. Therefore, an additional equation is required to obtain the unique values of these variables. The necessary equation is obtained by applying the Rankine-Hugoniot relation [20] to relate the pressure at the edge of the Knudsen layer to the ambient conditions:

$$\frac{P_l}{P_g}\frac{P_2}{P_l} = 1 + \gamma_g M\Gamma\left[\frac{\gamma_g+1}{4}M\Gamma + \sqrt{1+\left(\frac{\gamma_g+1}{4}M\Gamma\right)^2}\right] \tag{3.27}$$

where P_g and P_2 are the pressures in front of and behind the wavefront, respectively, $P_2 = P_v$, γ_g is the ratio of specific heats for shielding gas, $\Gamma = \sqrt{\gamma_v R_v T_v}/\sqrt{\gamma_g R_g T_g}$, and M is the Mach number which is related to m by the relation [17]:

$$m = M\sqrt{\frac{\gamma_v}{2}} \qquad (3.28)$$

The Mach number M and the density ρ_v, obtained by solving the above equations, can be used to calculate the vaporization flux due to pressure gradient on the weld pool surface corresponding to a local surface temperature T_l:

$$J_p = \rho_v MS \qquad (3.29)$$

where S is the speed of sound in the vapor at temperature T_v. Since the rate of vaporization of an alloying element is proportional to its partial pressure over the weld pool, the vaporization flux of element i, J_{pi}, due to pressure gradient can be given by [17]:

$$J_{pi} = a_i \frac{P_i^0}{P_l} \frac{M_i}{M_v} J_p \qquad (3.30)$$

3.2.3 Vaporization Rate and Composition Change

The total vaporization flux for element i is the sum of diffusion driven flux, J_{ci}, and pressure driven vapor flux, J_{pi}, and can be given by:

$$J_i = J_{ci} + J_{pi} \qquad (3.31)$$

The vaporization rate is obtained by integrating the vapor flux over the entire weld pool surface. The vaporization rate of element i is given by:

$$G_i = \iint_s J_i dxdy \qquad (3.32)$$

where s indicates the weld pool surface. The weight loss of element i can be calculated by:

$$\Delta m_i = \sum_t \iint_s J_i \Delta t dxdy \qquad (3.33)$$

where Δt is the time step. The initial weight percent of element i is chosen to be that of the base metal, indicated by W_{bi}. The weight percent of element i, W_i, in the weld pool can be calculated by:

$$W_i = \frac{V\rho W_{bi} - \Delta m_i}{V\rho - \sum_{i=1}^{n} \Delta m_i} \times 100\% \tag{3.34}$$

where V is the volume of the weld pool, ρ is the density of the liquid metal, and the variable n indicates the number of elements in the vapor. The final composition in the weld pool is calculated by an iterative scheme. After each iteration, the composition of alloying elements in the weld pool is updated. Using the new values of composition of alloying elements, all calculations are repeated until the calculated composition in the weld pool converges. The concentration change of element i reflects the difference of final weight percent in the weld pool and weight percent of element i in the base metal:

$$\Delta W_i = W_i - W_{bi} \tag{3.35}$$

3.3 Modeling Procedure

To systematically simulate vaporization rate and composition change, the mathematical models described in the previous sections need to be coupled. Fig. 3.2 shows the flow chart of the integration of these models. Starting from the calculation heat transfer and fluid flow in the weld pool, the temperature and velocity fields and the weld thermal cycles can be obtained. From the calculated temperature fields, the vaporization rate and composition change can be computed.

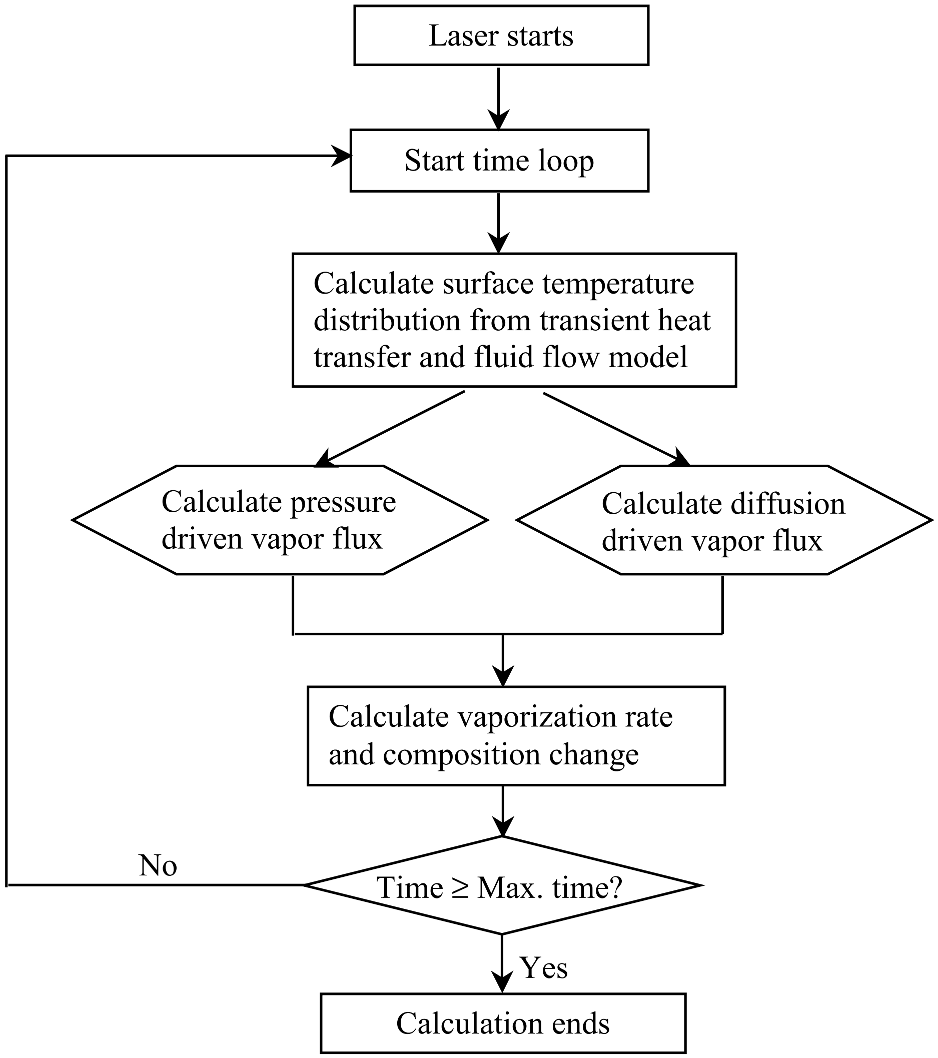

Fig. 3.2: Flow chart of the comprehensive model.

To check the capability of the mathematical models, in later chapters, these models will be applied to predict the weld pool geometry, vapor composition, weld pool composition change, and mass loss caused by vaporization under different welding conditions. The predicted results will be compared with the corresponding experimental results.

3.4 References

1. S. V. Patankar, *Numerical Heat Transfer and Fluid Flow* (New York: Hemisphere Publishing Corporation, 1980)
2. A. D. Brent, V. R. Voller and K J Reid, *Numer. Heat Transfer*, **13**, 297 (1988).
3. V. R. Voller and C. Prakash, *Int. J. Heat Mass Transfer*, **30**, 2690 (1987).
4. S. Kou and D. K. Sun, *Metall. Trans. A*, **16A**, 203 (1985).
5. K. Mundra, T. DebRoy and K. M. Kelkar, *Numer. Heat Transfer, Part A*, **29**, 115 (1996).
6. C. L. Chan, R. Zehr, J. Mazumder and M. M. Chen, *Modeling and Control of Casting and Welding Processes*, edited by S. Kou and R. Mehrabian (Warrendale: TMS, 1986) p229.
7. N. S. Tsai and T. W. Eagar, *Metall. Trans. B*, **16B,** 841 (1985).
8. D. A. Cremers, G. K. Lewis and D. R. Korzekwa, *Weld. J.*, **70**, 159s (1991).
9. W. Pitscheneder, *Ph.D. thesis*, The University of Leoben, 2001.
10. J. F. Ready, *LIA Handbook of Laser Materials Processing* (Orlando: Magnolia Publishing, 2001).
11. M. A. Bramson, *Infrared Radiation: a Handbook for Applications* (New York: Plenum Press, 1968).
12. K. Mundra and T. DebRoy, *Metall. Trans. B*, **24B**, 145 (1993).
13. M. von Allmen, *Laser-beam Interactions with Materials*, (New York: Springer Verlag, 1987).
14. C. L. Chan and J. Mazumder, *J. Appl. Phys.*, **62**, 4579 (1987)

15. P. A. A. Khan and T. DebRoy, *Metall. Trans. B*, **15B**, 641 (1984)

16. E. U. Schlunder and V. Gniclinski, *Chem. Ing. Technol.* **39**, 578 (1967).

17. T. DebRoy, S. Basu and K. Mundra, *J. Appl. Phys.*, **70**, 1313 (1991).

18. S. I. Anisimov and A. Kh Rakhmatulina, *Soviet Physics – JETP* **37**, 441 (1973).

19. C. J. Knight, *AIAA J.*, **17**, 519 (1979).

20. W. G. Vincenti and C. H. Kruger, *Introduction to Physical Gas Dynamics* (New York: Wiley, 1965).

Chapter 4

HEAT TRANSFER AND FLUID FLOW

In recent years, pulsed Nd:YAG lasers have been widely used for assembly and closure of high reliability electrical and electronic packages for the telecommunications, defense, aerospace and medical industries, where joining of smaller components is of interest [1-3]. Most previous research on welding with very small length scale has focused on welding methods, weld quality and weld properties [3-6]. However, very little effort has been made to understand the physical processes. During laser welding with small length scale, the interaction of the heat source and the material results in rapid heating, melting and circulation of molten metal in the weld pool aided by surface tension gradient and buoyancy forces. The resulting flow of liquid metal and heat transfer determine the changes in temperature with time, i.e., the thermal cycles, and the resulting structure and properties of the welds. The experimental measurements of the temperature and velocity fields during laser welding are difficult because of the small size of the weld pool, insufficient time for measurement, and high heating and cooling rates.

In recent decades, the application of numerical transport phenomena has resulted in useful information about the thermal cycles and weld pool geometry in both linear and spot welding. A numerical model to simulate heat transfer and fluid flow during steady and transient fusion welding has been developed and refined during the past 20 years at Penn State. The model has been used to calculate weld pool geometry, temperature and velocity fields during welding of pure iron [7,8], stainless steel [9-12], low alloy steel, [13,14] aluminum alloys [15] and titanium alloys [16] under different welding conditions. Calculations have been done for both moving and stationary heat sources and for laser beam as well as arc welding. Computed temperatures have been used to understand the evolution of phase composition [17-19], grain structure [16,20,21], inclusion structure [14,22,23], and weld metal composition change owing to both the evaporation of alloying elements [8,12,15] and the dissolution of gases [24,25]. However, most of these studies were concerned with relatively large welds. The heat transfer and fluid flow in the laser welding with small length scale have not received much attention in the literature.

In this chapter, the heat transfer and fluid flow in linear and spot Nd:YAG laser welding of 304 stainless steel with small length scale are simulated using a well tested, three-dimensional, transient, numerical heat transfer and fluid flow model. The model is applied to understand the evolution of the temperature field and the weld dimensions for various laser welding conditions. Dimensional analysis is carried out to understand the importance of the various driving forces for the liquid pool convection. Several important solidification parameters, including solidification rate R and temperature gradient G at the mushy zone/liquid front, are calculated. These parameters are useful for determining the solidification morphology and the scale of the solidification substructure. The effects of laser power, laser beam radius and welding speed on the heat transfer and fluid flow are also analyzed. The temperature and velocity fields, weld pool geometry, weld thermal cycle, temperature gradient, the solidification and cooling rates during spot and linear laser welding are compared to better understand these processes.

4.1 Laser Spot Welding

Laser spot welding has an important advantage for these applications because it can deliver a minimum amount of energy to very small components with high precision. Laser spot welds behave very differently from their moving weld counterparts because the temperature profiles never reach a steady state and the heating and cooling rates for these welds are much higher than those of linear welds.

Laser spot welds are characterized by small weld pool size, rapid changes of temperature and very short duration of the process. These characteristics make physical measurements of important parameters such as temperature and velocity fields, solidification rate and thermal cycles during laser spot welding very difficult. These parameters are important because the weld pool convection patterns and the heating and cooling rates determine the geometry, composition, structure and the resulting properties of the spot welds. Understanding the formation of non-equilibrium phases and solidification cracking based on fundamental principles requires knowledge of the heating and cooling rates. In recent decades, numerical calculations of heat transfer and fluid flow have been utilized to gain understanding in the evolution of temperature and velocity fields and weld geometry that cannot be obtained otherwise. However, most of these studies were concerned with arc welds where the time scale and length scale are much larger than those for laser welds. The heat transfer and fluid flow for laser spot welding will be discussed in this section.

4.1.1 Experimental Procedure

Multiple 304 stainless steel pulse Nd:YAG laser spot welds were produced at the Sandia National Laboratories. The steel had the following composition: 1 wt% Mn, 18.1 wt% Cr, 8.6 wt% Ni, 0.012 wt% P, 0.003 wt% S, and balance Fe. A Raytheon SS 525 laser was used for laser spot welding with pulse energies between 2.1 J and 5.9 J, and pulse durations of 3.0 ms and 4.0 ms. No temporal pulse shaping was employed. The laser beam was focused inside the quartz tube with a 100 mm focal length lens. For each combination of energy and duration, the laser beam was defocused to different extents to obtain various spot diameters and power densities. By controlling the beam shutter, individual spot welds from the pulsed laser beam were made on 3 mm × 10 mm × 17 mm EDM wire cut samples. Up to 15 individual spot welds were made on each of the samples. Laser spot size was measured with 50 μm Kapton film using the method described elsewhere [26]. Supplementary argon shielding of the plate surface during welding was provided to reduce oxide formation and for protection of the lens. Longitudinal metallographic cross-section measurements through several collinear welds for each plate were averaged to determine weld pool width and depth. The experimental conditions are indicated in Table 4.1.

Table 4.1: The experimental conditions.

Material	304 stainless steel
Pulse energy	2.1, 3.2, 5.9 J
Pulse power	0.53, 1.0, 1.9 kW
Pulse duration	3.0, 4.0 ms
Spot radius	0.159 - 0.57 mm
Spot welds	15 per plate
Shielding gas	Argon

4.1.2 Mathematical Modeling

As discussed in 3.1.2, the three-dimensional transient heat transfer and fluid flow model was used to calculate the temperature and velocity field, weld pool geometry, weld thermal cycle and some solidification parameters for laser spot welding. The liquid metal was assumed to be an incompressible Newtonian fluid. A very fine grid system and small time step were used to improve the computation accuracy. A typical grid system used contained 83 × 45 × 60 grid points, and the corresponding computational domain had dimensions of 30 mm in length, 15 mm in width and 15 mm in depth. Spatially non-uniform grids were used for maximum resolution of variables. A finer grid spacing was used near the heat source. The minimum grid space along the x, y and z directions were about 17, 17 and 10 μm, respectively. The time step used in the heating part was 0.05 ms, while the time step for the cooling part was 0.005 ms to obtain more accurate results.

The data used for calculations [26-30] are presented in Table 4.2.

Table 4.2: Data used for calculations [26-30].

Property/Parameter	Value
Density of liquid metal (kg/m^3)	7.2×10^3
Absorption coefficient	0.27
Effective viscosity (kg/m-sec)	0.1
Solidus temperature (K)	1697
Liquidus temperature (K)	1727
Enthalpy of solid at melting point (J/kg)	1.20×10^6
Enthalpy of liquid at melting point (J/kg)	1.26×10^6
Specific heat of solid (J/kg-K)	711.8
Specific heat of liquid (J/kg-K)	837.4
Thermal conductivity of solid (J/m-sec-K)	19.26
Effective thermal conductivity of liquid (J/m-sec-K)	209.3
Temperature coefficient of surface tension (N/m-K)	-0.43×10^{-3}
Coefficient of thermal expansion	1.96×10^{-5}

4.1.3 Results and Discussion

4.1.3.1 Comparison between Calculated and Experimental Results

The comparison between the measured and calculated geometry of weld pool cross sections is shown in Fig. 4.1. It is observed that the calculated weld pool geometry and dimensions agree well with the experimental results. Both the experimental and the measured weld pool geometries show that with the increase in the beam diameter, the weld pool becomes wider and shallower. This observation is consistent with distribution of energy over a wider area with the increase in the beam diameter. Since the temperature coefficient of surface tension is negative, the molten metal on the surface flows from the center to the periphery of the pool. As a result, the convection in the weld pool aids in the transport of heat from the middle to the periphery of the weld pool. The role of convection in the heat transfer will be discussed in more details later in this paper. The experimental values of weld pool depth and width for various laser power densities agree well with the corresponding calculated values as shown in Fig. 4.2. The fair agreement indicates validity of the transient heat transfer and fluid flow model.

4.1.3.2 Temperature and Velocity Fields

Figs. 4.3(a)-(e) show the computed temperature and velocity fields as a function of time. The contour values in the figures represent temperatures in K. In the initial period, the weld pool expands rapidly in size and the temperatures and velocities increase with time. At the end of the pulse, the peak temperature drops and the weld pool shrinks rapidly, as shown in Figs. 4.3(d) and 4.3(e). The liquid flow during heating is mainly driven by the force of surface tension and to a much less extent by the buoyancy force. This matter will be discussed more fully using dimensionless numbers in later sections. The calculations show that the weld pool solidifies completely in about 1.7 ms after the laser pulse is switched off. The maximum velocity in the weld pool is about 95 cm/s, while at the time of 5.0 ms (1.0 ms after the laser is switched off), the maximum velocity is still about 0.4 cm/s driven mainly by inertia.

A two-phase solid-liquid mushy zone exists in the thin region between the solidus (1697 K) and liquidus (1727 K) isotherms. The size of this zone is very small during heating as shown in Figs. 4.3(a)-(c). At the end of the pulse, the size of the mushy zone increases significantly as can be observed from Figs. 4.3(d) and 4.3(e). The evolution of the mushy zone during laser spot welding is discussed in detail in a later section.

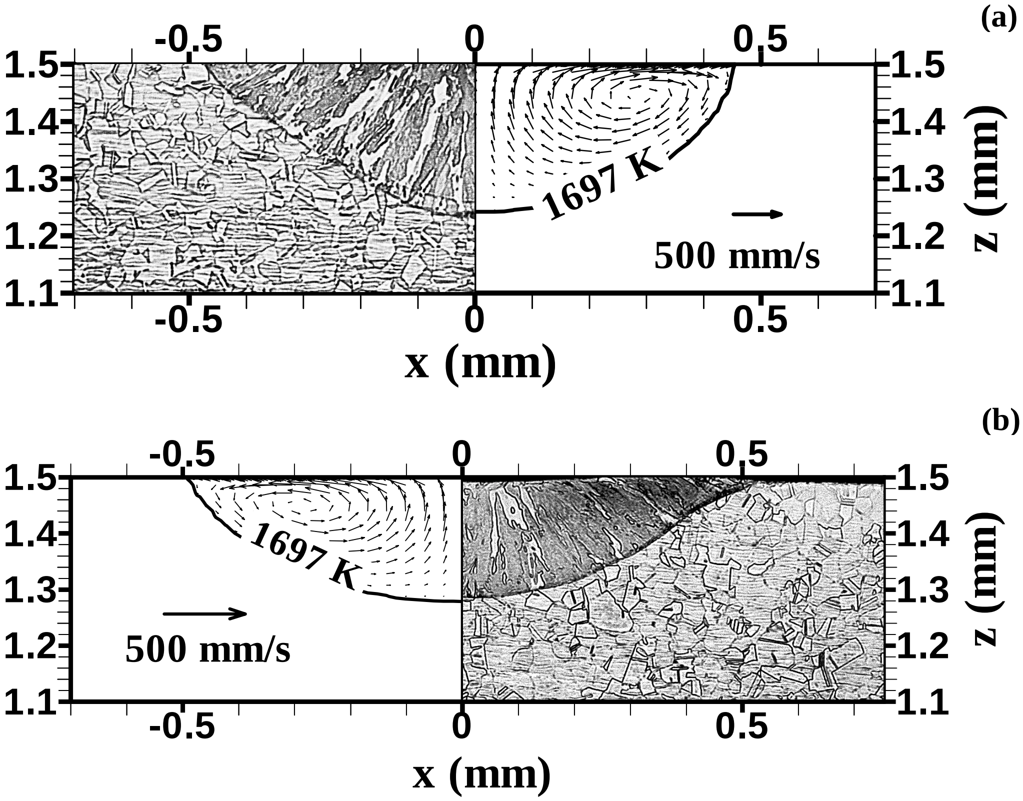

Fig. 4.1: Experimental and calculated weld pool cross sections for laser power of 1067 W and pulse duration of 3 ms. (a) beam radius: 0.428 mm; (b) beam radius: 0.57 mm. Data used in calculation are shown in Table 4.2.

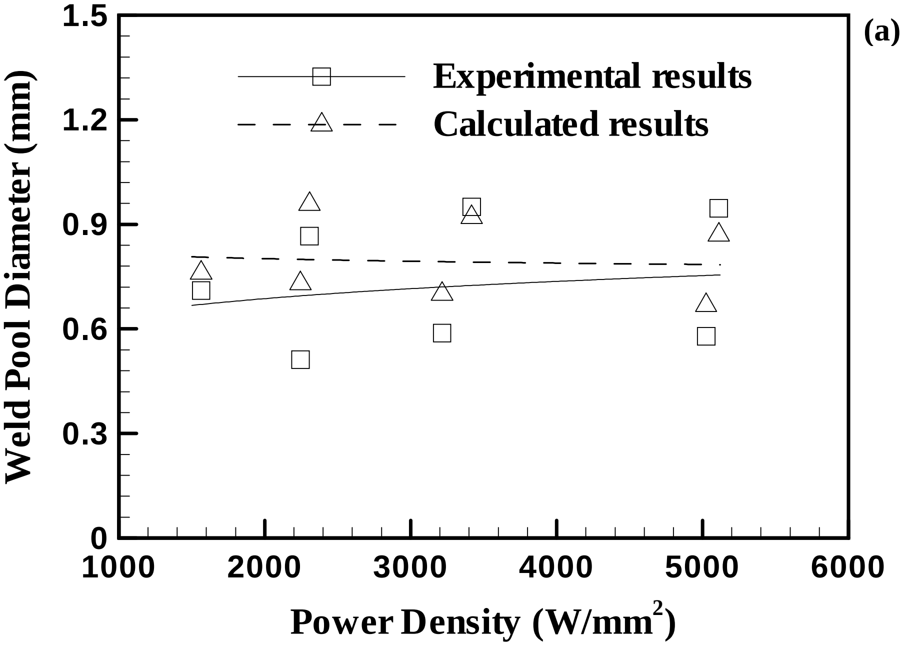

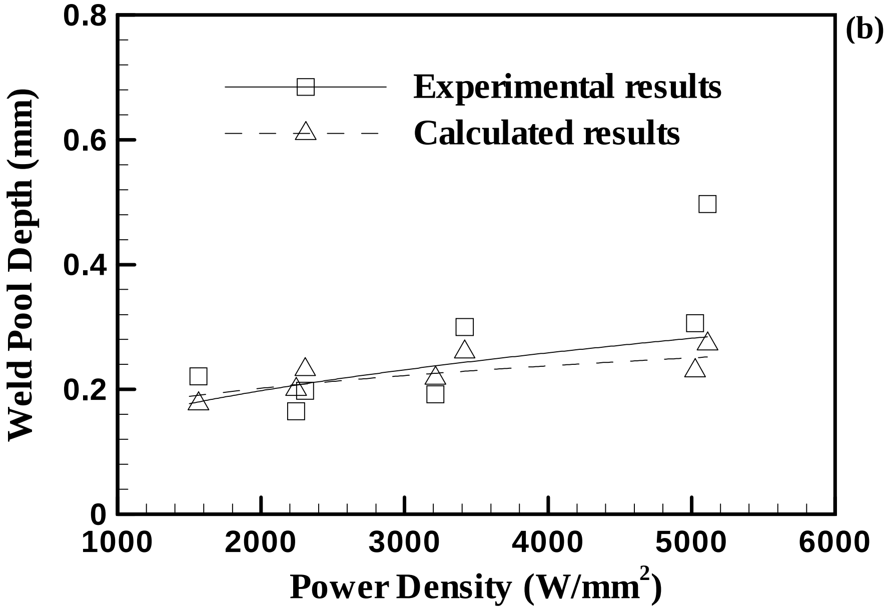

Fig. 4.2: The experimental and calculated results of effects of laser power density on (a) the weld pool diameter and (b) the weld pool depth. The power density is defined as the ratio of power and the laser beam area of cross section. Pulse duration: 3 ms. Welding parameters are shown in Table 4.1. Data used in calculation are shown in Table 4.2.

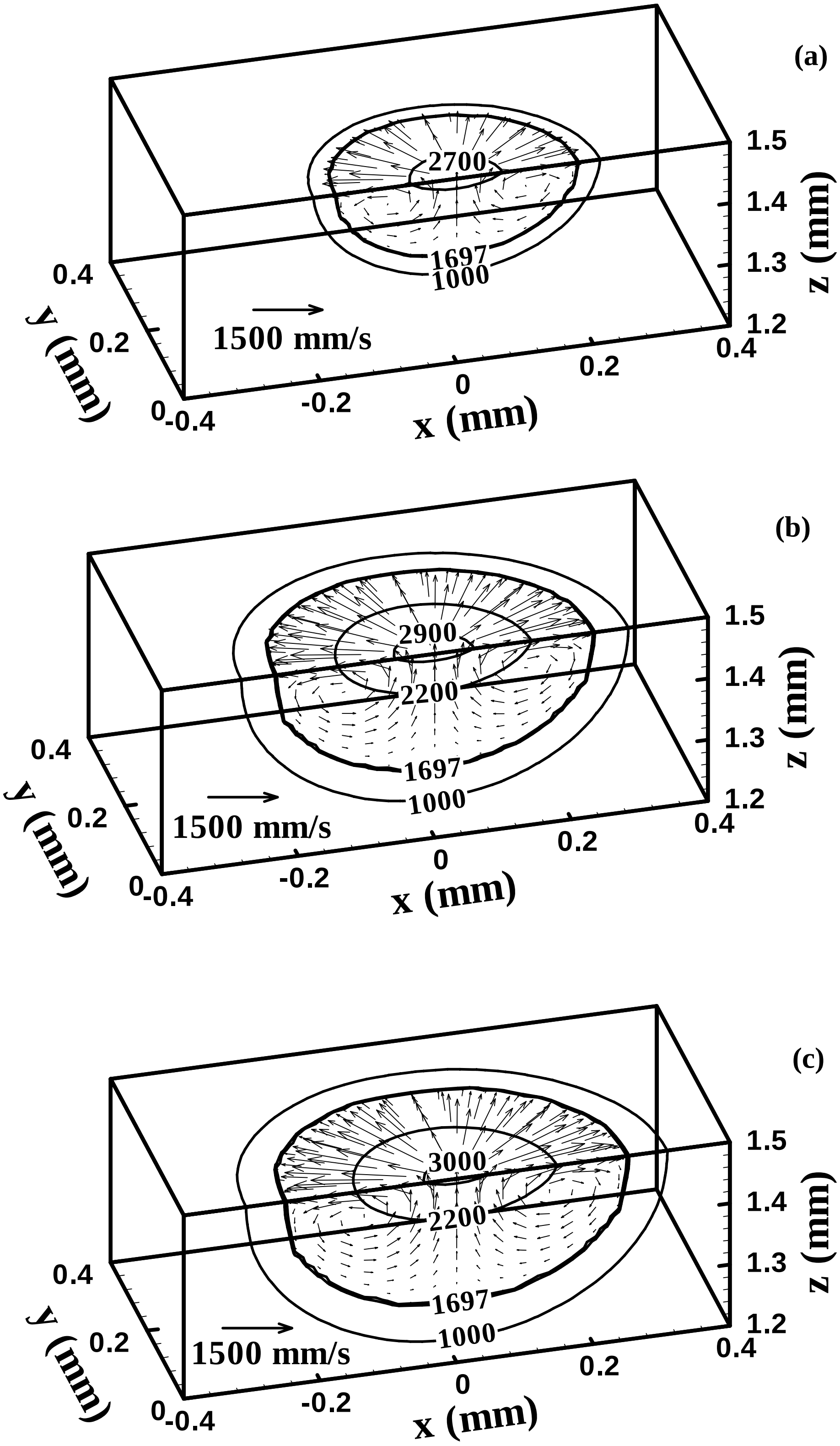
(a)
2700
1697
1000
1500 mm/s
x (mm)
y (mm)
z (mm)
-0.4
-0.2
0
0.2
0.4
0
0.2
0.4
1.2
1.3
1.4
1.5
(b)
2900
2200
1697
1000
1500 mm/s
x (mm)
y (mm)
z (mm)
(c)
3000
2200
1697
1000
1500 mm/s
x (mm)
y (mm)
z (mm)

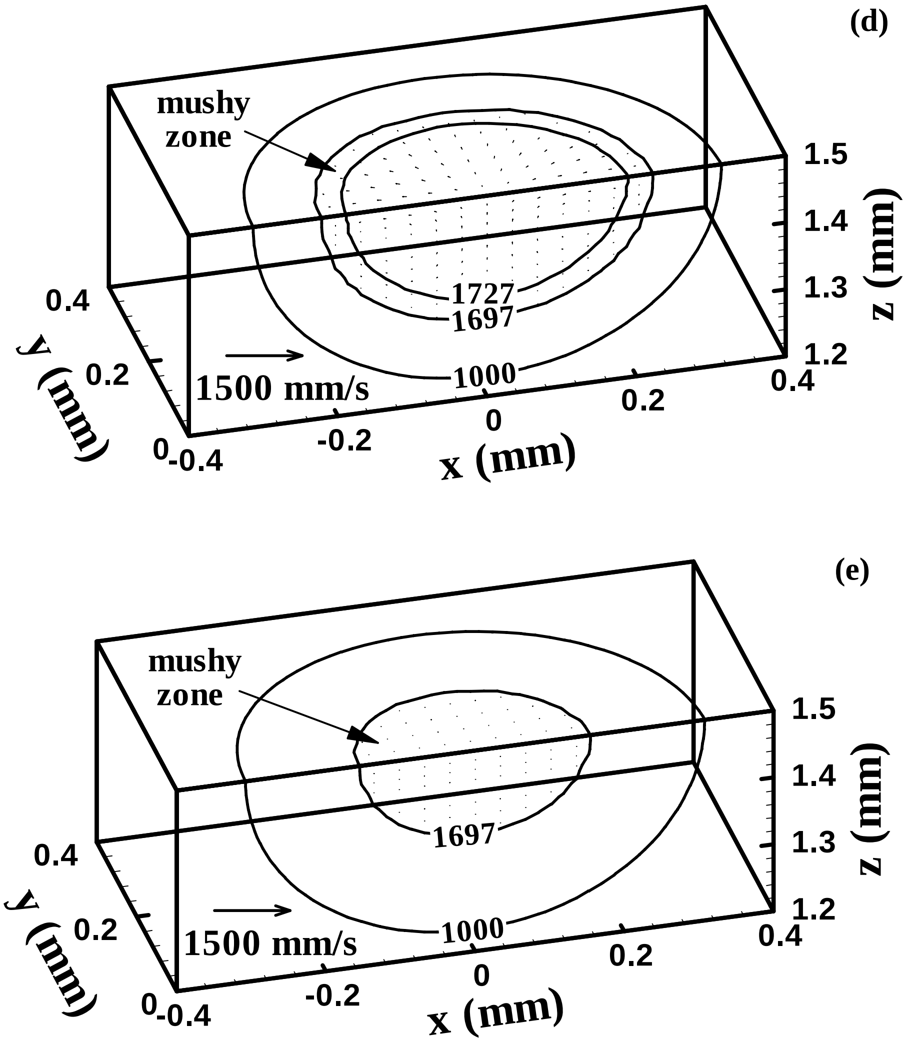

Fig. 4.3: Computed temperature and velocity fields at different times: (a) t = 1 ms, (b) t = 3 ms, (c) t = 4 ms, (d) t = 4.5 ms and (e) t = 5 ms. Laser power: 530 W, pulse duration: 4.0 ms, and beam radius: 0.159 mm. Data used in calculation are shown in Table 4.2.

4.1.3.3 Weld Thermal Cycle

Fig. 4.4 shows the changes in the computed temperatures at various monitoring locations. The monitoring locations 2, 3 and 4 are at 0.1 mm distance from the weld center but at 0°, 45° and 90° planes, respectively. Similarly, monitoring locations 5, 6 and 7 are at 0.2 mm from the weld center along 0°, 45° and 90° planes, respectively. The results indicate that initially the heating rate in the weld pool is very fast. With the increase in temperature, the heating rate decreases gradually until the laser is switched off. When the solidification starts, the temperature decreases quickly until it is close to the liquidus temperature. At this temperature, there is a plateau in the thermal cycle curves indicating a very low cooling rate due to the release of the latent heat of fusion, as discussed in the next section. When the weld pool cools below the liquidus temperature, the temperature decreases gradually.

From Fig. 4.4, it can also be seen that the thermal cycles at locations equidistant from the weld center show considerable variation. At the top surface, i.e., the x-y plane, the shape of the weld pool is close to a circle. As a result, the temperatures at different locations equidistant to the weld center are the same. However, in the x-z plane, the temperatures at the 0° plane, represented by curve 2 are higher than those at the 90° plane represented by curve 4, although both locations are at a distance of 0.1 mm from the location of the laser beam axis. This variation is mainly due to the shallow pool geometry which increases the temperature gradient along the 90° plane in comparison with the 0° plane. The average temperature gradient in the weld pool at the 90° location is higher than that at the 0° plane since the weld pool is shallow and wide. For locations equidistant from the weld center, the higher the average temperature gradient, the lower the temperature. Therefore, at these locations, the temperatures at the 0° plane are the highest and those at the 90° plane are the lowest. A similar observation was also made by Zhang *et al*. [31] while studying GTA spot welding.

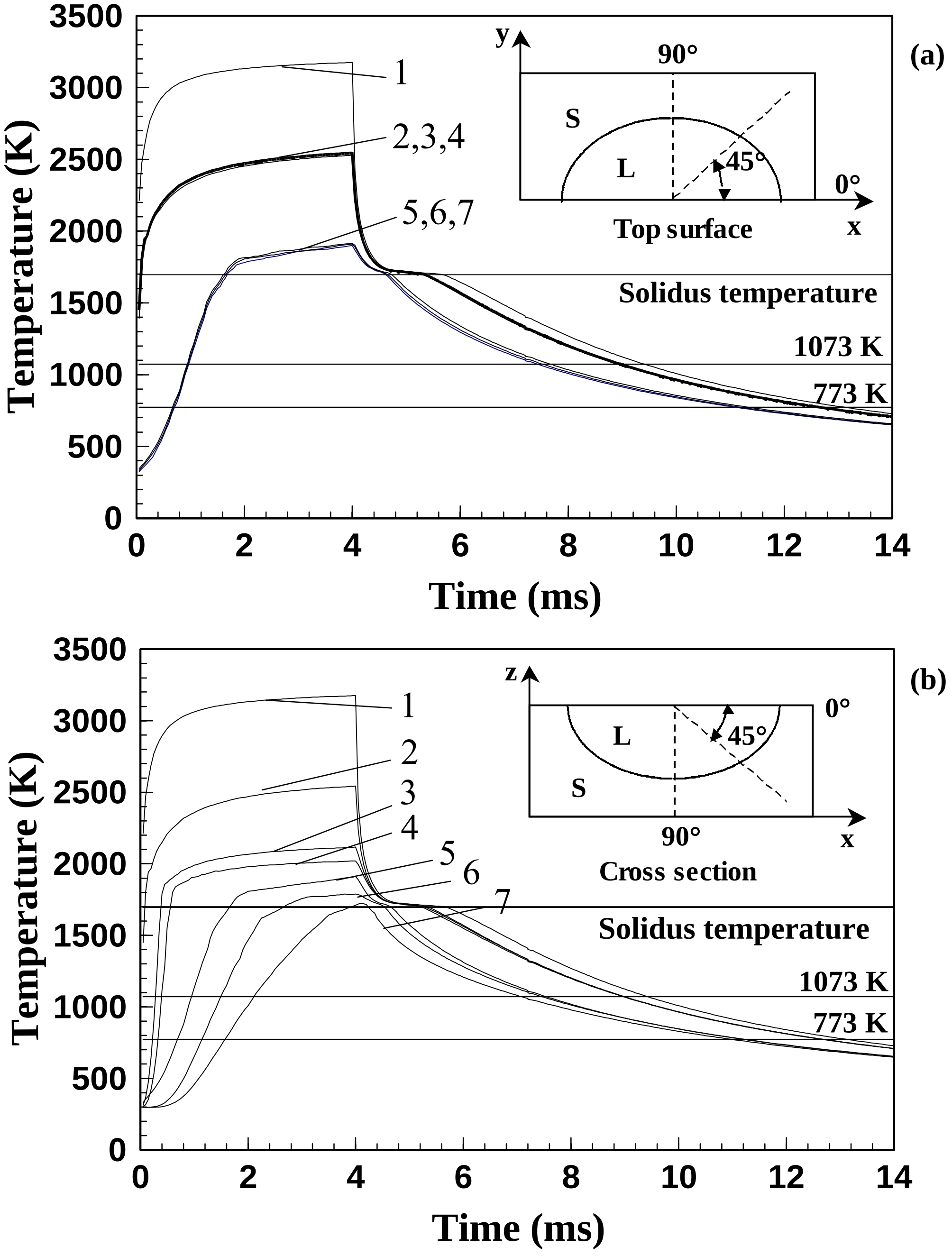

Fig. 4.4: Weld thermal cycles at different locations: (a) top surface; (b) cross section. Distance from the weld center: 1: 0.0 mm; 2: 0.1 mm at 0°; 3: 0.1 mm at 45°; 4: 0.1 mm at 90°; 5: 0.2 mm at 0°; 6: 0.2 mm at 45°; and 7: 0.2 mm at 90°, as shown in the small figure. Calculated weld pool radius is 0.254 mm and the depth is 0.202 mm. So all points are in the weld pool at some time. The solid horizontal lines indicate solidus temperature. Laser power: 530 W, pulse duration: 4.0 ms, and beam radius: 0.159 mm. Data used in calculation are shown in Table 4.2.

The peak temperatures and the heating rates vary significantly depending on the location. Similarly, the cooling rates above the liquidus temperature vary significantly. However, as the weld metal cools, the spatial variation of the cooling rates decreases. In the range of 1073 K to 773 K (800 °C to 500 °C), the cooling rate is almost independent of position, which is due to nearly constant outward heat loss from all locations of the weld. Thus in steels, where much of the final microstructure is determined by the cooling rate through this temperature range, the spatial variation of microstructures is expected to be small. However, there are certain alloys whose microstructures are highly sensitive to cooling rates [13]. In such cases, the spatial variation of cooling rates should be considered carefully.

4.1.3.4 Role of Convection from Dimensionless Numbers

1) Relative importance of heat transfer by conduction and convection

In the weld pool, heat is transported by a combination of convection and conduction. The relative importance of convection and conduction in the overall transport of heat can be evaluated from the value of the Peclet number, Pe, which is defined in Equation 2.11. When Pe is much smaller than one, the heat transport within the weld pool occurs primarily by conduction. When Pe is much higher than 1, the primary mechanism of heat transfer is convection. For spot welding, the value of the Peclet number is a function of time since both u and L_R depend on time. Fig. 4.5 shows the change of maximum Peclet number with time in the weld pool. It can be seen that at the beginning of pulse cycle, the Peclet number is low and conduction is the primary mechanism of heat transfer. With time, the Peclet number increases and convection becomes the more important heat transport mechanism in the weld pool. When the pulse is switched off, the Peclet number drops to a very low value very quickly and conduction becomes the main mechanism of heat transfer again due to rapid decrease in velocity.

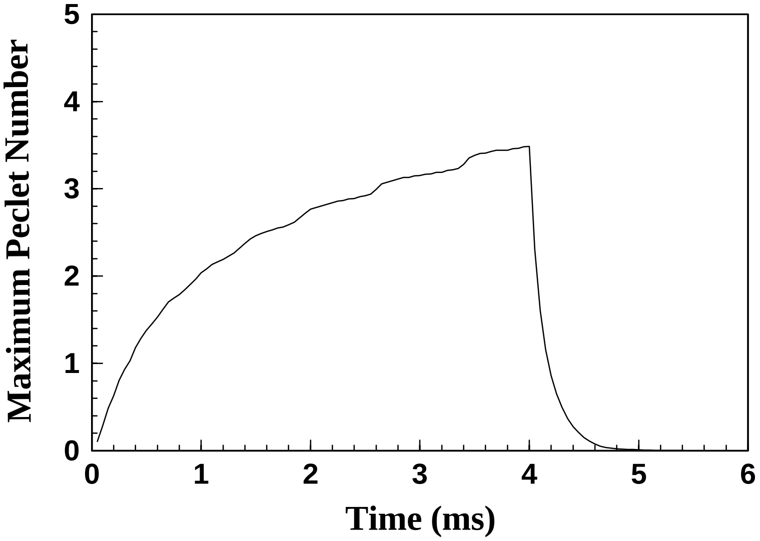

Fig. 4.5: The variation of maximum Peclet number with time. Laser power: 530 W, pulse duration: 4.0 ms, and beam radius: 0.159 mm. Data used in calculation are shown in Table 4.2.

2) Relative importance of different driving forces

The driving forces for the liquid flow in the weld pool considered in present study include surface tension gradient and buoyancy force. As discussed in Chapter 2, the relative importance of these driving forces can be estimated using several dimensionless numbers defined in Equation 2.8 to 2.10. Using the physical properties listed in Table 4.2 and the experimental conditions of Fig. 4.3, the calculated dimensionless number at t = 4 ms (i.e., just before the laser is switched off) are listed in Table 4.3. It can be expected that the liquid flow is mainly driven by Marangoni convection and to a much less extent by the buoyancy force.

Table 4.3: Dimensionless numbers calculated in the weld pool just before the laser is switched off.

Dimensionless number	Description	Value
Gr	Ratio of buoyancy to viscous force	3.7×10^{-4}
Ma	Ratio of surface tension to viscous force	111.0
$R_{s/b}$	Ratio of surface tension to buoyancy force	3.0×10^{5}

3) Order of magnitude of maximum velocity in the weld pool

Since the surface tension force is the dominant driving force for convection in the weld pool, the order of the maximal velocity can be approximated by Equation 2.12. The maximum liquid velocity in the weld pool estimated using Equation 2.12 is found to be 84.1 cm/s. This value is in good agreement with that calculated using the transient three-dimensional heat transfer and fluid flow model, where the maximum velocity at t = 4 ms was found to be about 95 cm/s.

The foregoing dimensional analysis provides insights about the weld pool development during laser spot welding. It should be noted that these order of magnitude analyses cannot provide accurate and detailed information about the spot welding processes, which requires numerical calculation with very fine grids and small time steps.

4.1.3.5 Solidification

During the rapid solidification of the weld pool, the critical parameters in determining the fusion zone microstructure are temperature gradient (G), solidification growth rate (R), undercooling (ΔT) and alloy composition. Undercooling, ΔT, indicates how far a liquid alloy of a given composition is cooled below its equilibrium liquidus temperature. Since weld solidification proceeds from the preexisting solid substrate, only undercooling associated with growth is important. The undercooling is comprised of contributions from thermal, constitutional, kinetic and solid curvature effects [32]. In this study, in order to simplify the calculations, no undercooling is considered. The solidification parameters are calculated by considering only the heat transfer and fluid flow in the weld pool. In other words, the equilibrium liquidus isotherm is assumed to represent the liquid/mushy zone boundary, while the equilibrium solidus isotherm is assumed to be the mushy zone/solid boundary. So the calculations underpredicted the mushy zone size.

The evolution of mushy zone size during the laser spot welding is shown in Fig. 4.6. During heating, the liquidus and solidus isotherms are very close and the resulting size of the mushy zone is very small. After the pulse is switched off, the mushy zone expands initially, and the maximum size of the mushy zone is reached when the pure liquid region diminishes. The size of the mushy zone then decreases as solidification proceeds further.

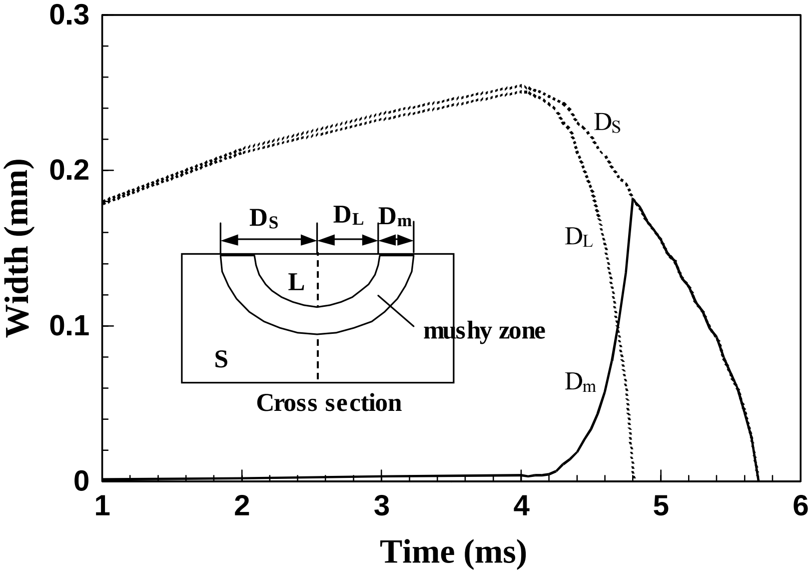

Fig. 4.6: Evolution of the mushy zone size during laser spot welding. The symbols D_L and D_S are the distances from the weld center to the liquid/mushy zone and mushy zone/solid interfaces at the pool top surface, respectively. The size of the mushy zone, D_m, is defined as the difference between D_L and D_S, as shown in the small figure. Laser power: 530 W, pulse duration: 4.0 ms, and beam radius: 0.159 mm. Data used in calculation are shown in Table 4.2.

The initial expansion of mushy zone size could be explained by considering the effect of the latent heat of fusion. When the temperature is higher than the liquidus temperature, the heat loss is accompanied by a decrease in temperature. As the temperature drops between the liquidus and solidus temperatures, the heat loss comes mainly from the release of the latent heat of fusion, and the temperature decrease is very slow. As a result, the liquidus isotherm moves faster than the solidus isotherm until the pure liquid region vanishes and the entire weld pool is transformed to mushy region. The evolution of the mushy zone during solidification is demonstrated more clearly in Fig. 4.7. As shown in this figure, the pure liquid region disappears about 0.8 ms after the solidification starts, and the mushy zone exists for about another 0.9 ms before the weld pool solidifies completely. The existence of a large mushy region is a unique feature of the solidification during spot welding [33].

Fig. 4.8 shows the distances of the mushy zone/liquid interface from the weld center as a function of time for two laser power densities (cases A and B). The symbols D_0 and D_{90} represent the distances between the mushy zone/liquid front and weld center at 0° and 90° planes. It is observed that for case A, D_0 and D_{90} are very close to each other, while for case B, D_0 is twice that of D_{90} due to the use of a larger beam radius. From this figure, the solidification rate, defined as the rate at which the mushy zone/liquid interface in the weld pool advances, can be calculated as the slopes of distance versus time. Figs. 4.9 and 4.10 show the four important parameters of solidification, temperature gradient (G), solidification rate (R) and their combinations GR and G/R as functions of the time at the 0° and 90° planes for cases A and B, respectively. The temperature gradients, G_0 and G_{90}, are evaluated in the mushy zone at the mushy zone/liquid interface. The figures show that G_0 and G_{90} at both planes decrease with time, while the solidification rates at both planes increase with time. The maximum solidification rate is reached when the weld pool solidifies completely. In order to understand the solidification phenomena, let us consider the following heat balance equation [31]:

$$R = \frac{dr}{dt} = \frac{k_S G_S - k_L G_L}{f_L L} \tag{4.1}$$

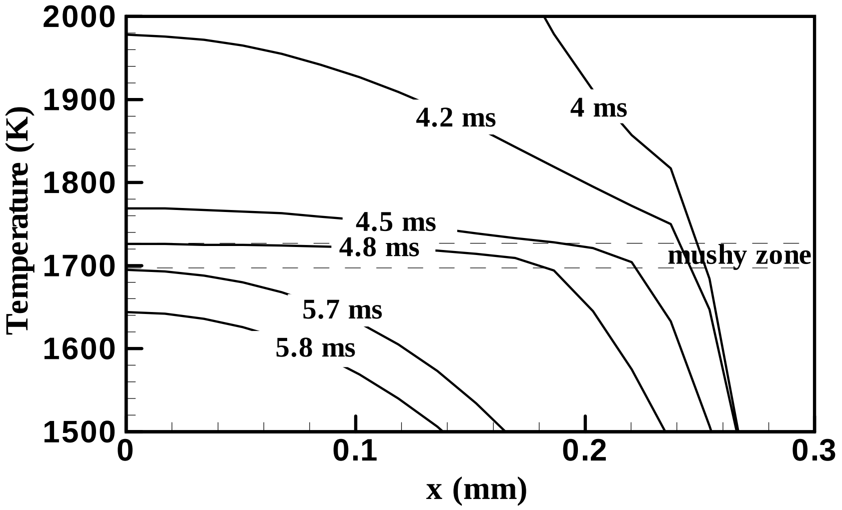

Fig. 4.7: Distribution of temperature at the pool top surface at various solidification times. Time equal to 4 ms corresponds to the time when solidification starts. Laser power: 530 W, pulse duration: 4.0 ms, and beam radius: 0.159 mm. Data used in calculation are shown in Table 4.2.

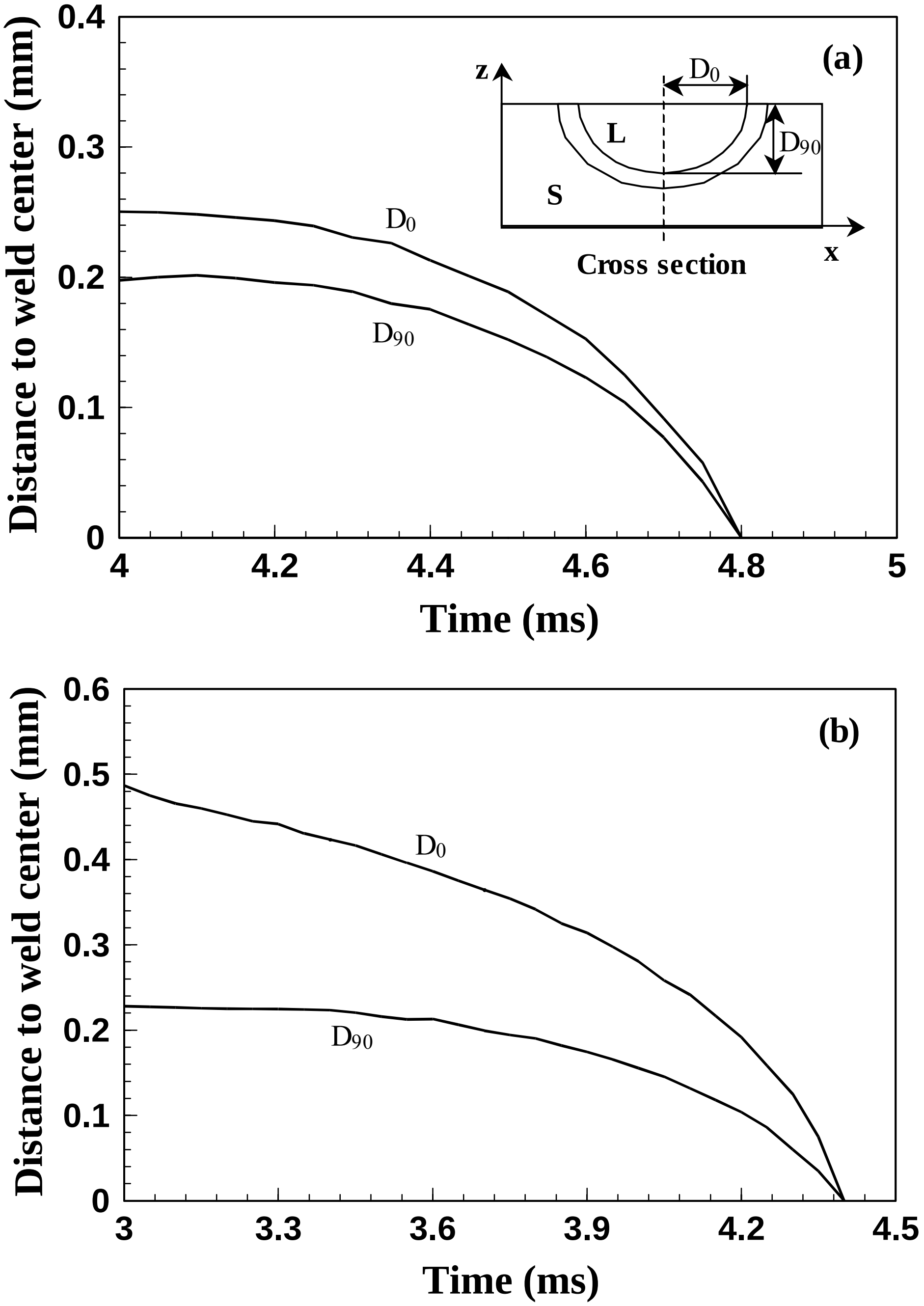

Fig. 4.8: Distance between the mushy zone/liquid front and weld center as a function of time. (a) Laser power: 530 W, pulse duration: 4.0 ms, and beam radius: 0.159 mm. (b) Laser power: 1967 W, pulse duration: 3.0 ms, and beam radius: 0.57 mm. Data used in calculation are shown in Table 4.2.

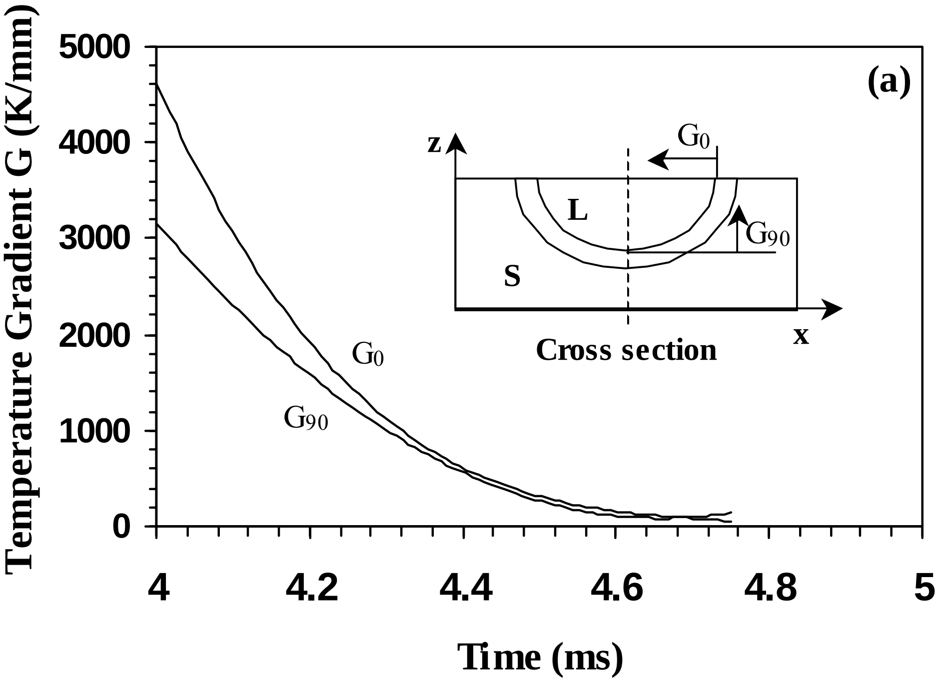
Temperature Gradient G (K/mm)
5000
4000
3000
2000
1000
0
4
4.2
4.4
4.6
4.8
5
Time (ms)
(a)
z
G0
L
G90
S
x
Cross section
G0
G90

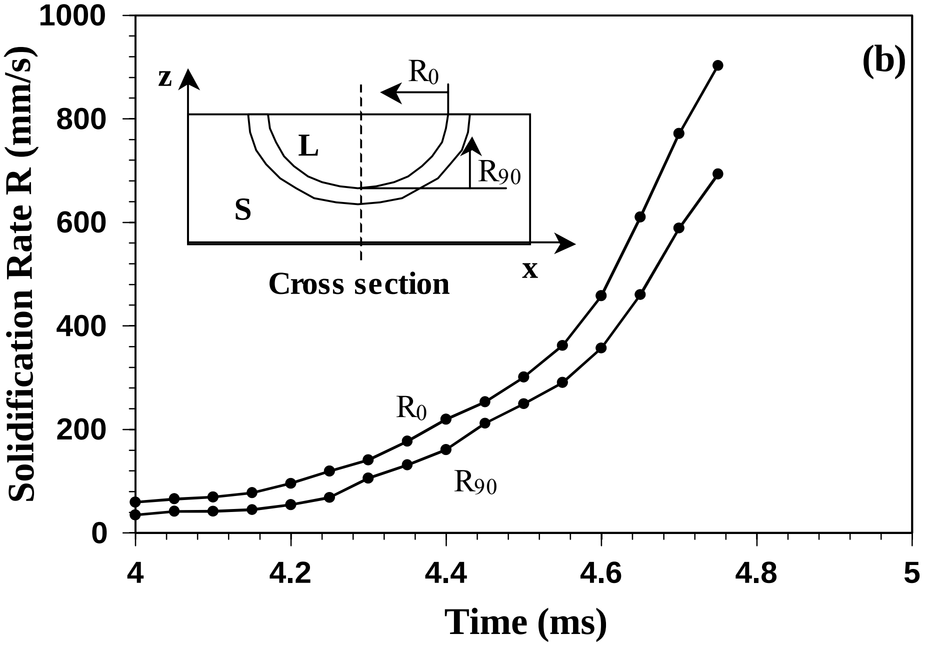
Solidification Rate R (mm/s)
1000
800
600
400
200
0
4
4.2
4.4
4.6
4.8
5
Time (ms)
(b)
z
R0
L
R90
S
x
Cross section
R0
R90

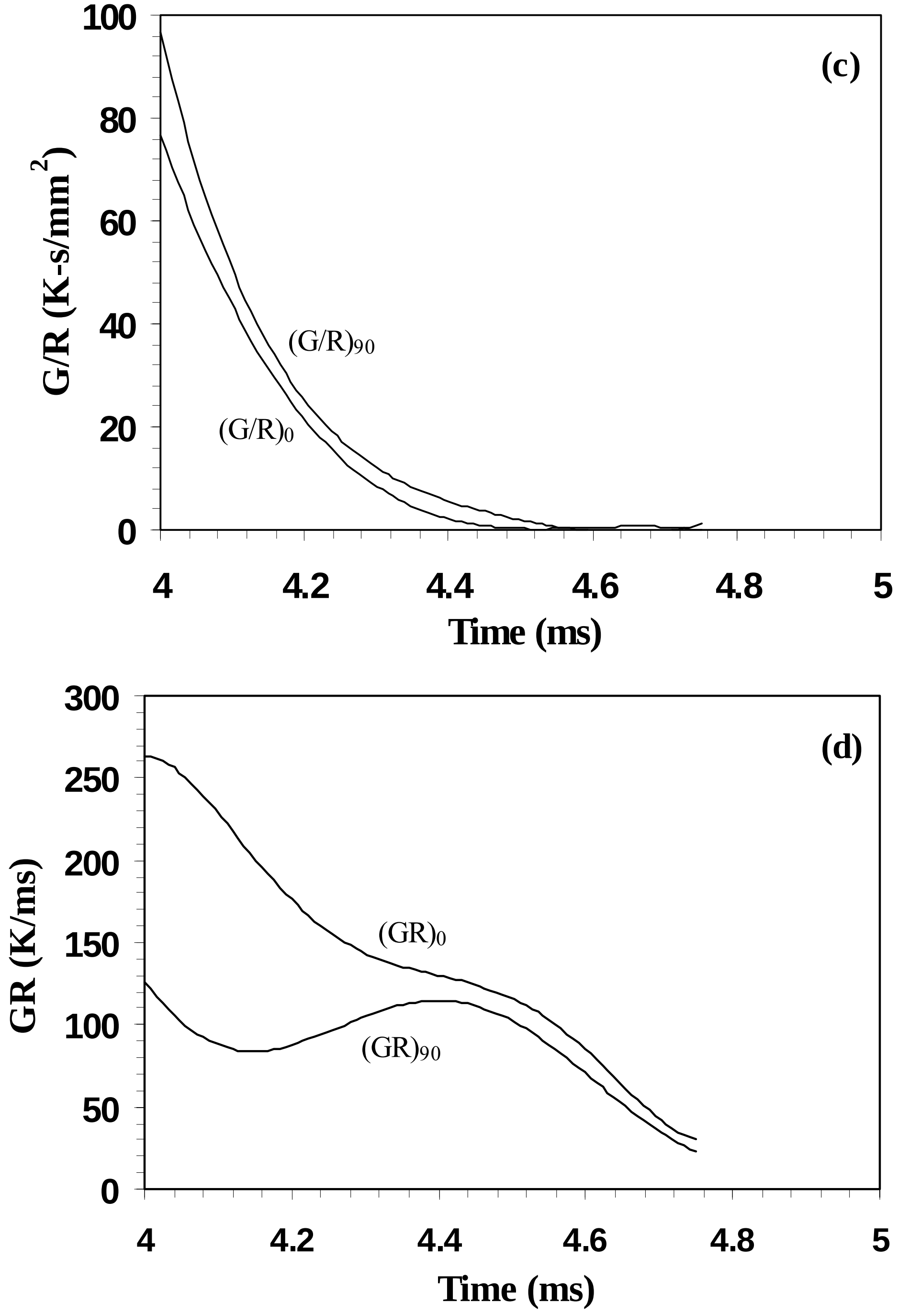

Fig. 4.9: The value of G, R, G/R, GR along 0° and 90° planes at the mushy zone-liquid interface as a function of time. (a) G; (b) R; (c) G/R; (d) GR. Laser power: 530 W, pulse duration: 4.0 ms, and beam radius: 0.159 mm. Data used in calculation are shown in Table 4.2.

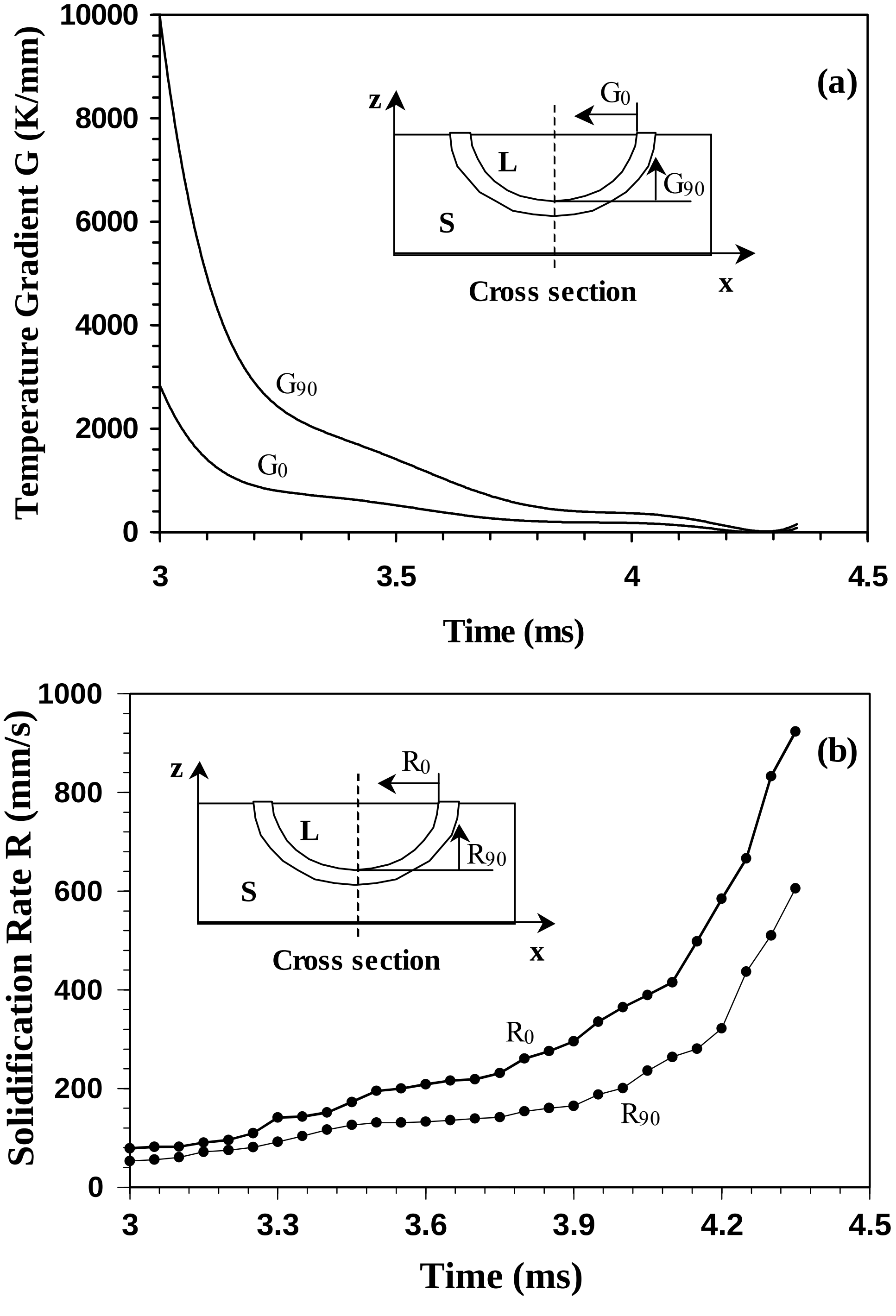
(a)
Temperature Gradient G (K/mm)
10000
8000
6000
4000
2000
0
3
3.5
4
4.5
Time (ms)
G90
G0
z
x
G0
G90
L
S
Cross section
(b)
Solidification Rate R (mm/s)
1000
800
600
400
200
0
3
3.3
3.6
3.9
4.2
4.5
Time (ms)
R0
R90
z
x
R0
R90
L
S
Cross section

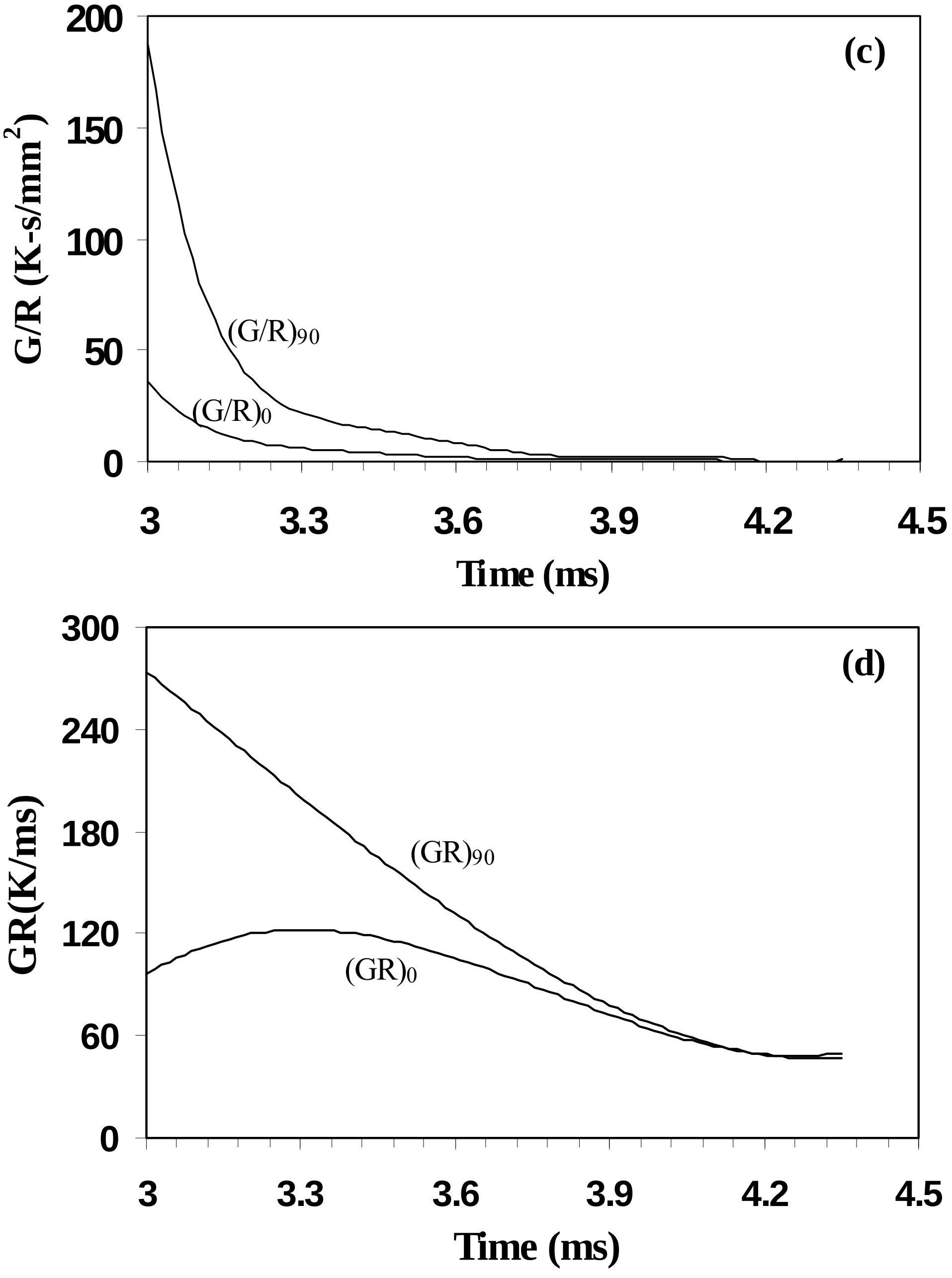

Fig. 4.10: The values of G, R, G/R, GR along 0° and 90° planes at the mushy zone-liquid interface as a function of time. (a) G; (b) R; (c) G/R; (d) GR. Laser power: 1967 W, pulse duration: 3.0 ms, and beam radius: 0.57 mm. Data used in calculation are shown in Table 4.2.

where G_S and G_L are the temperature gradients in mushy zone and liquid at the mushy zone/liquid interface, respectively, k_S and k_L are the thermal conductivities in the solid and the liquid, respectively, and f_L is the liquid fraction. As shown in Fig. 4.7, G_L drops more rapidly than G_S during solidification. Furthermore, f_L decreases with time as the solidification progresses. As a result, the solidification rate increases with time, which is indicated in Figs. 4.9(b) and 4.10(b).

The solidification rate, R, and temperature gradient, G, are important in the combined forms G/R and GR (cooling rate). As shown in Figs. 4.9(c) and 4.10(c), the solidification parameter G/R decreases with time, since G decreases while R increases with time. From Fig 4.10(c), the maximum value of G/R is about 180 K-s/mm^2 at the 90° plane.

Using the solidification parameter G/R, the solidification front stability could be determined. The criterion for constitutional supercooling for plane front instability is given as [34]:

$$G / R < \Delta T_E / D_L \qquad (4.2)$$

where ΔT_E is the equilibrium solidification temperature range at a given composition, and D_L is the solute diffusion coefficient in liquid. For 304 stainless steel, ΔT is equal to 30 K. D_L is taken as the diffusion coefficient of chromium in pure liquid iron. In general, the diffusion coefficients of different elements in liquid are almost all approximately the same order of magnitude, 10^{-3}-10^{-2} mm^2/s [35]. Thus, the value of $\Delta T/D_L$ is from 3×10^3 to 3×10^4 K-s/mm^2. Therefore, the plane front is unstable.

The solid-liquid interface stability factor, G/R, is related to the solidification morphology. As the value of G/R increases, the interface morphology changes from equiaxed-dendritic to cellular-dendritic and then, to cellular grains [36]. As the solidification progresses from the mushy zone/liquid front to the weld center, the mushy zone/liquid interface has the maximum temperature gradient and minimum solidification growth rate. While for the weld center, the situation is completely different. It has the minimum temperature gradient and maximum solidification rate. Therefore, the value of G/R decreases from the fusion line to the weld center. As a result, we may expect a cellular type of microstructure close to the fusion line, an equiaxed-dendritic microstructure at the pool center, and a cellular-dendritic microstructure between these two regions.

The solidification parameter GR is useful as it influences the scale of the solidified substructure. Since G decreases and R increases with time, the value of GR does not change monotonically with time. Depending on how the rates of G and R change with time, the value of GR can either increase or decrease with time as shown in Figs. 4.9(d) and 4.10(d).

From Figs. 4.9 and 4.10, it can be seen that the solidification parameters vary with location in the weld pool. The computed values of these parameters at the mushy zone/liquid interface for 0° and 90° planes are different. These differences can be explained using weld pool geometry. From Fig. 4.8, D_0 is very close to D_{90} for case A, while for case B, D_0 is much larger than D_{90}. In other words, the weld pool cross section for case A (Fig. 4.9) is close to a hemisphere. As a result, the values of the four solidification parameters along 0° and 90° planes are very close, while for case B (Fig. 4.10), there are significant differences in the values of these four parameters between 0° and 90° planes. As discussed before, the value of the average temperature gradient at the 90° location is higher than that at the 0° plane, while the solidification rate along the 90° plane is lower than that at the 0° plane because of lower rate of the change of D_{90} with time.

It should be noted that the calculated solidification parameters have not been validated by comparison with the corresponding experimental results in 304 stainless steel laser spot welds. Calculations presented here indicate aspects of solidification in a qualitative manner, since the focus here is the examination of the results of the transient heat transfer and fluid flow model. Furthermore, the solidification process investigated in the present model is governed only by the transfer of heat. An accurate prediction of the weld pool solidification will require consideration of both the thermodynamics and kinetics of solidification.

4.1.3.6 Comparison of Laser Spot Welding with GTA Spot and Linear Weldings

Laser spot welding is characterized by a much shorter time span than the GTA spot welding or GTA linear welding. As a result, the temperature gradients in the work piece and its cooling rates are significantly different in the three processes. The computed values of spatial and the temporal variations of temperature for the three welding processes are compared in Table 4.4. The laser spot welding is characterized by higher power intensity, higher peak temperature and smaller weld pool size. As a result, the cooling rate, temperature gradient and the solidification rate in the weld pool are much higher than those in GTA linear and spot welding. The computed results in Table 4.4 indicate that during laser spot welding, the maximum temperature gradient in the weld pool can reach up to 3050 K/mm and the maximum solidification rate can be as high as 920 mm/s. For a typical GTA spot welding of 1005 steel, the maximum temperature gradient and solidification rate in the weld pool are about 430 K/mm and 30 mm/s, respectively. More important, the cooling rate in the laser spot welding is significantly higher than in the GTA welding. Therefore, it is possible to obtain different solidification substructures in the fusion zone depending on the welding process. The computed results in the table provide a good understanding of the relative values of important parameters for the three welding processes. However, the results must be used with caution since the temperature gradients and the cooling rates presented in Table 4.4 depend strongly on the welding parameters.

Table 4.4: Comparison of laser spot welding variables with GTA linear welding [37] and GTA spot welding [31].

	GTA linear welding	GTA spot welding	Laser spot welding
Materials	AISI 1005 carbon manganese steel	AISI 1005 carbon manganese steel	304 stainless steel
Power (kW)	1.9	1.9	1.9
Beam radius (mm)	2.35	2.35	0.57
Pulse duration / welding velocity	velocity = 0.6 mm/s	16 s	3 ms
Peak temperature (K)	2000	2100	2700
Depth (mm)	1.85	1.8	0.22
Half-width (mm)	4.41	4.3	0.48
Cooling rate between 773 K and 1073 K (K/s)	40	250	41,380
Maximum temperature gradient at the top surface (K/mm)	120	430	3050
Maximum solidification rate at the top surface (mm/s)	0.6	30	920

4.2 Laser Linear Welding

4.2.1 Temperature and Velocity Fields

Fig. 4.11 shows the computed three dimensional temperature and velocity fields for a typical linear YAG laser welding of 304 stainless steel with small length scale. The temperature and velocity of liquid metal are indicated by the contour lines and the black arrows, respectively. Since the temperature coefficient of surface tension dγ/dT is negative, the molten metal on the surface flows from the middle to the periphery of the liquid pool. As a result, convection aids in the transport of heat in the weld pool. The calculated maximum temperature and liquid velocity along the y-direction in the weld pool are 2119 K and 440 mm/s, respectively.

The calculated liquid metal velocity, weld pool radius and Peclet number for different laser powers are presented in Fig. **4.12**. Both the velocity of the liquid metal and the weld pool radius increase with the laser power. As a result, the increased laser power results in a higher Peclet number. From the value of Pe shown in Fig. **4.12**, it is observed that convective heat transfer plays an important role in the transport of heat in the weld pool under most conditions. The small characteristic length for laser linear welding limits the liquid flow to a certain extent. However, convection is still an important mechanism of heat transfer in the weld pool because the Peclet number is still much higher than unity.

Taking into account the welding conditions considered in Fig. **4.11**, the ratio of surface tension force to buoyancy force is 3.84×10^5. Therefore, the liquid flow for laser linear welding is driven mainly by Marangoni convection and, to a much lesser extent, by the buoyancy force.

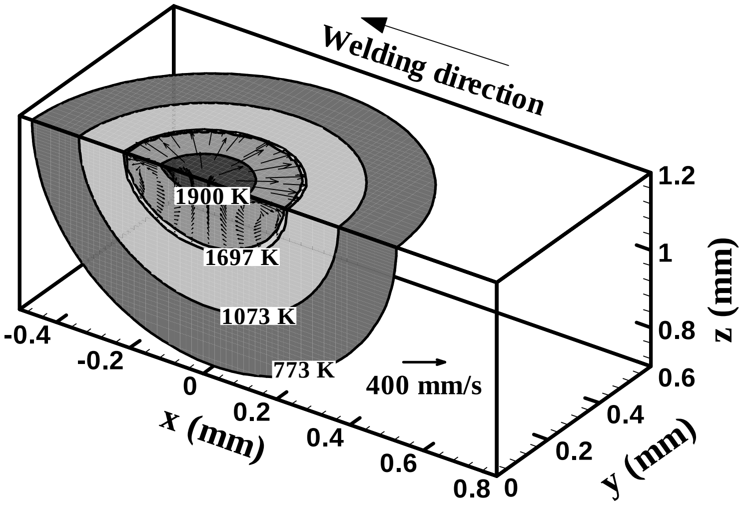

Fig. 4.11: Calculated temperature and velocity fields in three dimensions in a 304 stainless steel sample. Laser power: 100 W, beam radius: 100 µm, and welding speed: 1 mm/s. Data used in calculation are shown in Table 4.2.

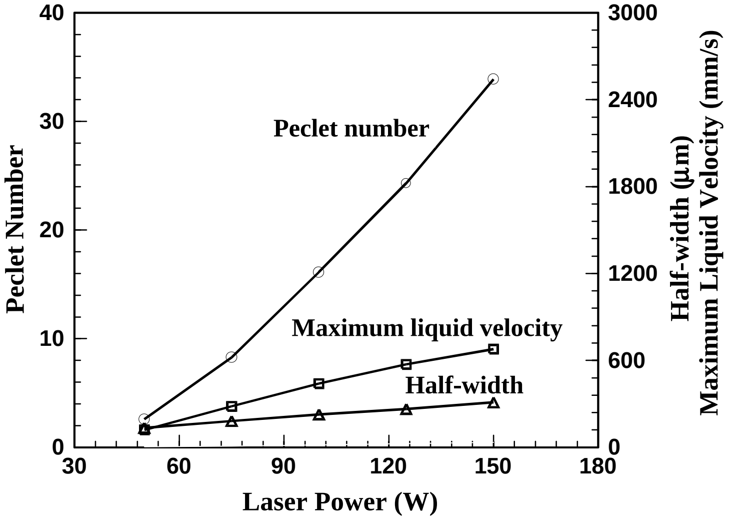

Fig. 4.12: Calculated values of maximum liquid velocity along the y-direction, weld pool half-width and Peclet number for different laser powers during welding of a 304 stainless steel sample. Beam radius: 100 µm, and welding speed: 1 mm/s. Data used in calculation are shown in Table 4.2.

Fig. 4.13 shows the computed peak temperature profiles for different combinations of laser power up to about 600 W and beam radius in the range of 50 to 150 μm. For laser welding with very small length scale, the peak temperature must remain between the melting and boiling points of the material being welded. The boiling point, defined as the temperature at which the sum total of the equilibrium partial pressures of all the constituent alloying elements equals 1 atmosphere, is viewed as the maximum permissible weld pool temperature. This upper limit of peak temperature avoids formation of a keyhole and severe metal loss by vaporization and particle ejection that can contaminate the welding environment with metal vapors and ejected metal particles. In large welds where contamination of the weldment by the metal vapors and particles is often not a major issue, a keyhole is often deliberately formed to achieve deep penetration welds in thick plates. In contrast, an important requirement in laser welds with small length scale is to keep the parts free of contamination and a large depth of penetration may not be needed, since fairly thin parts are joined. The computed results in Fig. 4.13(a) show that the practical range of laser power for laser welding with small length scale becomes rather narrow when a smaller beam radius is selected. This behavior is consistent with the increase in power density due to reduction in beam radius resulting in rapid rise of the peak temperature to the boiling point of the alloy.

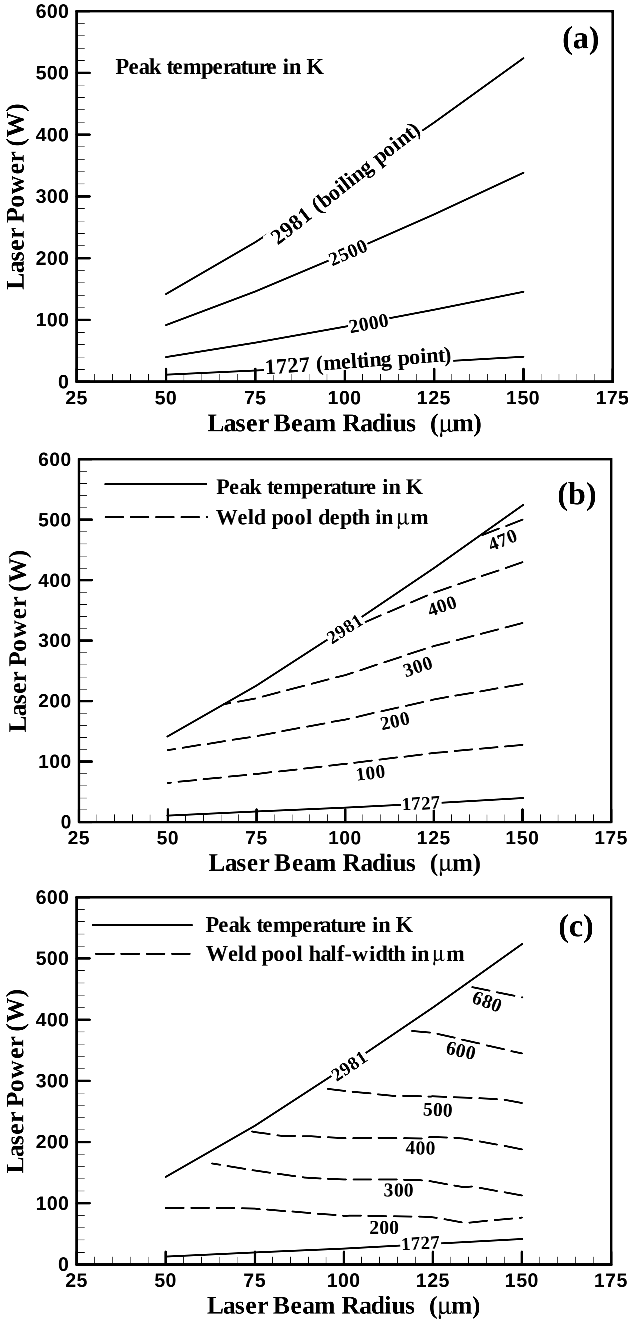

Fig. 4.13: (a) Peak temperature, (b) weld pool depth and (c) weld pool half-width for different combinations of laser power and beam radius. The peak temperature profiles corresponding to the melting and boiling points of 304 stainless steel are also shown in (b) and (c) so that the practical operating range of variables can be viewed. Welding speed: 1 mm/s. Data used in calculation are shown in Table 4.2.

The computed depth and half-width of the weld pool under various combinations of laser power and spot size are shown in Figs. 4.13(b) and 4.13(c), respectively. These results provide a useful link between the welding variables and the weld geometry. For example, for a laser beam radius of 100 μm, a laser power of 25 W is required for the liquid pool to form. At this power, the half-width and depth of the weld pool are both very small, only 29 and 5 μm, respectively. On the other hand, the peak temperature attains its upper limit, i.e., the boiling point of 304 stainless steel, at a laser power of 321 W for the same beam radius. The corresponding half-width and depth of the weld pool are much larger: 517 and 406 μm, respectively. The computed results in Fig. 4.13 provide guidance as to how the depth and width of the weld pool can vary during laser linear welding as a function of beam radius and the laser power. An important feature of the results in Fig. 4.13 is that a particular weld attribute, such as the peak temperature or weld penetration, can be achieved by multiple combinations of welding variables. The existence of multiple paths to attain a desired weld attribute demonstrates the flexibility of the laser linear welding process.

4.2.2 Weld Thermal Cycle

Fig. 4.14 shows the computed thermal cycles at different monitoring locations for a linear laser welding. At locations equidistant from the beam axis, the temperatures are higher along the y-direction (perpendicular to the welding direction) than those along the vertical z-direction. This behavior originates from the specific weld pool geometry that results from the surface tension driven flow. In other words, the temperature gradient along the z-direction is higher than that along the y-direction because of the wide and shallow weld pool. From Fig. 4.14, it can also be seen that during both the heating and the cooling periods, there are inflection points at liquidus temperature in the thermal cycle curve. This feature results from the differences in the enthalpies of the solid and the liquid metals.

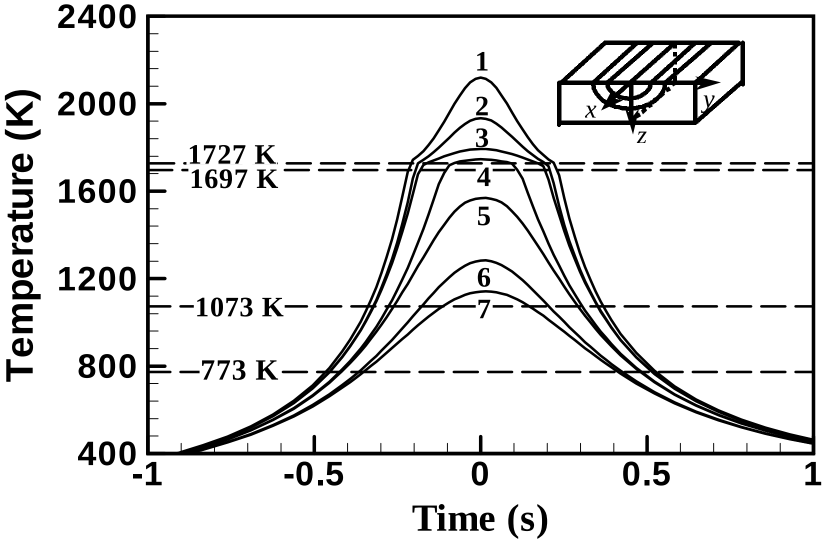

Fig. 4.14: Calculated thermal cycles at different locations in a 304 stainless steel sample. Distances from weld centerline: 1: y = 0 μm, z = 0 μm; 2: y = 100 μm, z = 0 μm; 3: y = 0 μm, z = 100 μm; 4: y = 200 μm, z = 0 μm; 5: y = 0 μm, z = 200 μm; 6: y = 300 μm, z = 0 μm; 7: y = 0 μm, z = 300 μm. Laser power: 100 W, beam radius: 100 μm, and welding speed: 1 mm/s. Data used in calculation are shown in Table 4.2.

The variations of the computed peak temperature, maximum velocity of liquid metal and weld pool size with laser beam radius are shown in Figs. **4.15** and **4.16**. At a constant laser power, smaller laser beam size results in higher peak temperatures, liquid metal velocities and weld pool depths due to higher laser power density. On the other hand, the weld pool width does not change monotonically with laser beam radius. Fig. **4.16** shows that the weld pool width increases first and then decreases with the increase of laser beam radius. When the power density is high enough to melt the areas right below the laser beam, the weld pool width increases with beam radius. However, as the beam radius increases, the laser power density decreases to a value that is insufficient to melt the entire area under the beam and, as a consequence, the weld pool width decreases. For the conditions assumed in Fig. **4.16**, the critical laser beam radius is 205 μm. The liquid pool width begins to decrease when the spot size changes from this value.

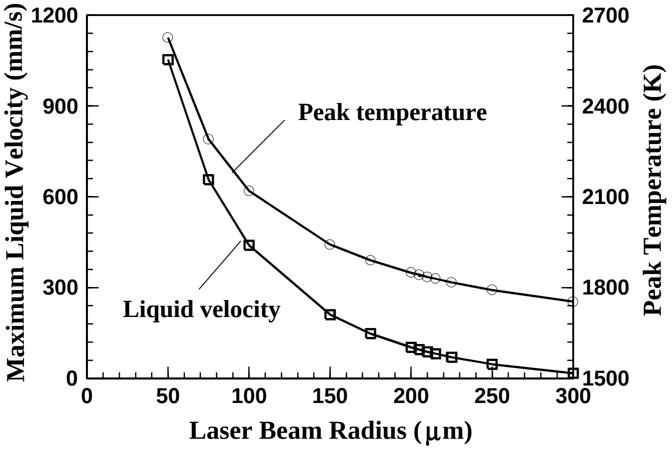

Fig. **4.15**: Effects of laser beam size on the temperature and maximum liquid velocity along the y-direction in the weld pool in a 304 stainless steel sample. Laser power: 100 W, welding speed: 1 mm/s. Data used in calculation are shown in Table **4.2**.

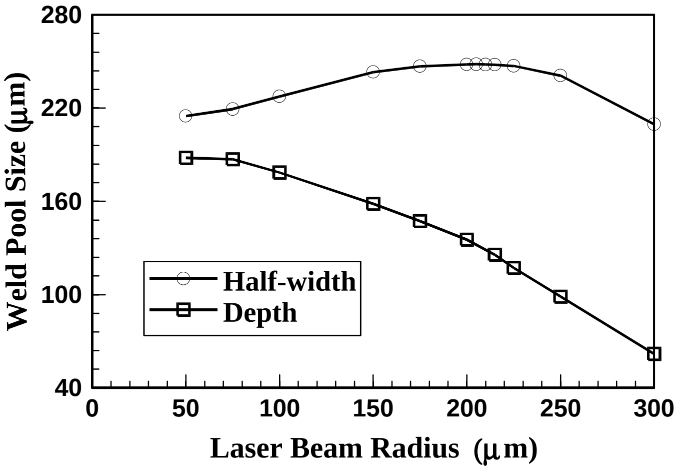

Fig. **4.16**: Effects of laser beam size on the half-width and depth of the weld pool in a 304 stainless steel sample. Laser power: 100 W, welding speed: 1 mm/s. Data used in calculation are shown in Table **4.2**.

4.2.3 Solidification

Since the shape of the weld pool remains constant at steady state during laser linear welding, the solidification rate varies with position along the fusion boundary. This point is illustrated in Fig. 4.17, which shows that the direction of movement of the solidification front is along the maximum thermal gradient normal to the solid/liquid interface. Therefore, the steady state solidification rate, *R*, is related to the welding speed as:

$$R = V \cos \alpha \tag{4.3}$$

where α is the angle between the normal to the solid/liquid interface and the welding direction, and V is the welding speed. The solidification rate is lowest at the edge of the weld pool ($\alpha \rightarrow 90°$, $\cos \alpha \rightarrow 0°$), indicated by point B in Fig. 4.17. The solidification rate is the highest at point A on the weld center line because the interface normal has the same direction as the welding direction. The solidification rate decreases from point A to point B along the fusion boundary.

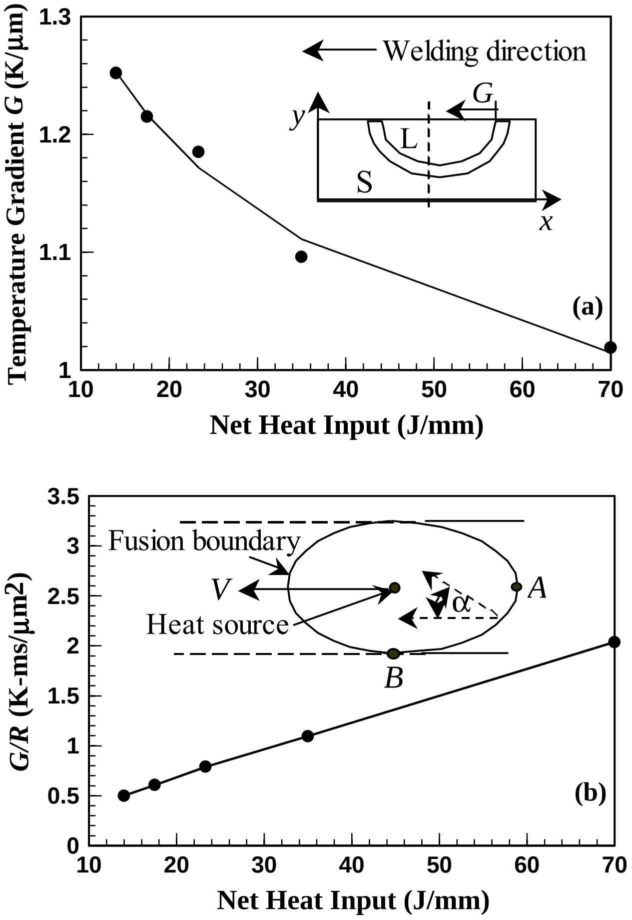

Fig. **4.17**: Calculated values of (a) G and (b) G/R at the weld center line at different net heat inputs in a 304 stainless steel sample. Laser power: 100 W, beam radius: 100 µm. The net heat input variation was obtained by varying welding speed while keeping the laser power constant.

The temperature gradient and the solidification rate are important in the combined forms G/R and GR as they influence the solidification morphology and the scale of the solidification substructure, respectively. As the value of G/R increases, the interface morphology changes from equiaxed-dendritic to cellular-dendritic and then, to cellular grains [38]. Often the value of G/R close to the fusion line is large enough to facilitate cellular solidification. As the temperature gradient in the weld pool decreases with distance from the fusion boundary, the solidification microstructure may vary spatially. For example, in some cases, an equiaxed-dendritic microstructure at the weld pool center and a cellular-dendritic microstructure between fusion boundary and weld center line may be obtained. Fig. 4.17 shows the temperature gradient G and G/R at the weld center line for different net heat inputs that were simulated by varying the welding speed while keeping the laser power constant. The net heat input, H_n, is defined as the amount of heat absorbed per unit length of weld from a traveling heat source, i.e., the ratio of the absorbed power and the welding speed [39]:

$$H_n = \frac{\eta Q}{V} \tag{4.4}$$

where η is laser absorption coefficient, Q is the laser power, and V is the welding speed. In Fig. 4.17, higher values of H_n were obtained by decreasing the welding speed from 2.5 to 0.5 mm/s for a 100 W laser beam. It is shown that with the increase in net heat input, the temperature gradient decreases, and the value of G/R at the weld center line increases. Thus, the solidification structure of the fusion zone is affected by the net heat input.

The cooling rate significantly affects the structure and properties of the welds. The weld cooling rates in laser welding are typically high, often in the range of 10^4 to 10^6 °C/s, whereas the cooling rates in GTA spot welding can reach a maximum of about 10^3 °C/s [40]. Cooling rates in welding are often compared by calculating the time taken for cooling from 800 to 500 °C, Δt_{8-5}. The austenite to ferrite phase transformation takes place in this temperature range in plain carbon steels. Although less significant for other alloys, Δt_{8-5} gives a convenient parameter to compare cooling times. For linear welds, Δt_{8-5} is calculated by dividing the x-distance between contour lines of 1073 K and 773 K by the welding speed, as shown in Fig. 4.18. The computed results show that Δt_{8-5} increases linearly with net heat input. This trend is qualitatively consistent with the following expression for $\Delta t_{8\text{-}5}$ derived by considering heat conduction from a point heat source in a thick plate [41] and ignoring convective heat transfer:

$$\Delta t_{8-5} = \frac{\eta Q / V}{2\pi k \Theta_1} \tag{4.5}$$

where k is the thermal conductivity of materials, Θ_1 is defined as

$$\frac{1}{\Theta_1} = \left(\frac{1}{773 - T_0} - \frac{1}{1073 - T_0} \right) \tag{4.6}$$

where T_0 is the initial temperature prior to welding in K. It should be noted here that Bhadeshia *et al*. [42] found that the magnitude of the cooling rates computed by using the heat conduction model are not reliable. So, here only the effects of variation of different welding parameters on the cooling time are compared.

Fig. 4.19 shows the computed cooling rate from the heat transfer and fluid flow model as a function of welding speed for linear laser welding. As expected, the cooling rate increases with welding speed, with all other variables kept constant. It should be noted that because both the cooling rate, GR, and the solidification rate, R, decrease with net heat input, the variation of temperature gradient, G, with net heat input is not monotonous. Depending on how the cooling rate and solidification rate change with net heat input, the value of the temperature gradient can either increase or decrease. The results shown in Fig. 4.17(a) indicate that the temperature gradient decreases with net heat input under the welding conditions selected in this study.

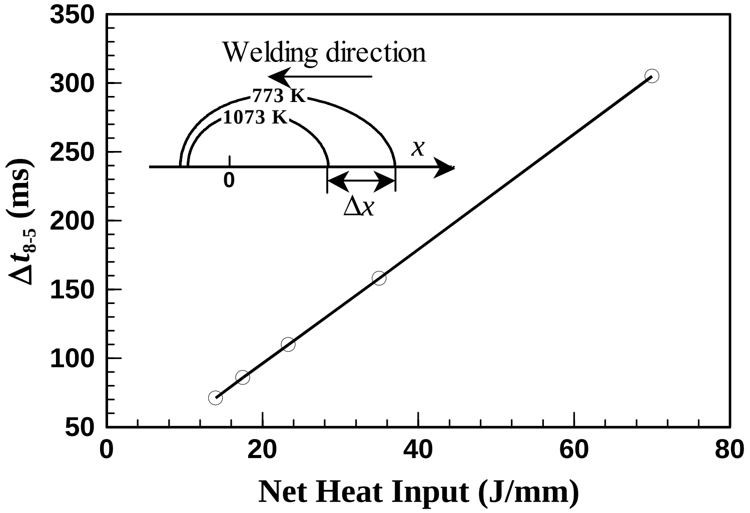

Fig. 4.18: Calculated cooling time from 800 to 500 °C at weld center line at different net heat inputs in a 304 stainless steel sample. Laser power: 100 W, beam radius: 100 µm. Data used in calculation are shown in Table 4.2.

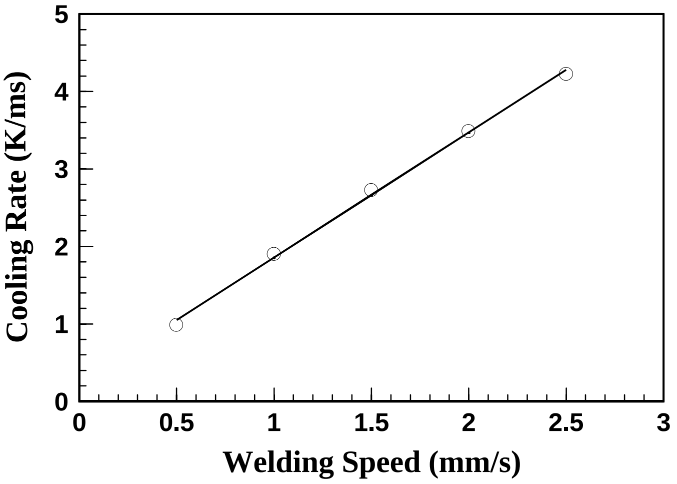

Fig. 4.19: Average cooling rate from 800 to 500 °C at weld center line as a function of welding speed in a 304 stainless steel sample. Laser power: 100 W, beam radius: 100 µm. Data used in calculation are shown in Table 4.2.

The computed solidification parameters for linear laser and spot laser welding with small length scale are shown in Table 4.5. The temperature gradient, solidification rate and G/R for spot welding are those along the mushy zone/liquid interface at the top surface when the solidification starts. It can be observed that the solidification rate and cooling rate in the temperature range from 1073 to 773 K for laser spot welding are much higher than those in linear laser welding due to extinction of the laser heat source when the solidification starts.

Table 4.5: Comparison of the solidification parameters in linear and spot laser welding of a 304 stainless steel sample with small length scale. Laser power: 100 W and laser beam radius: 100 μm.

	Laser linear welding	Laser spot welding		
		Pulse duration		
Welding speed / Pulse duration	Welding speed: 1 mm/s	1 ms	5 ms	10 ms
Temperature gradient G (K/μm)	1.10	2.94	2.48	2.20
Solidification rate R (μm/ms)	1	34.0	27.3	21.0
G/R (K-ms/μm^2)	1.10	0.086	0.091	0.105
Cooling rate from 1073 to 773 K (K/ms)	1.90	448	159	104

The solidification process investigated here has considered only the transport of heat. An accurate prediction of the weld pool solidification will require consideration of both the thermodynamics and kinetics of solidification. Nonetheless, the model presented here allows the calculation of acceptable range of welding variables such as laser power and beam diameter to attain a target weld geometry. In addition, the model can be used as a tool to seek small length scale laser welding conditions necessary to achieve an appropriate cooling rate and a target microstructure.

4.3 Summary and Conclusions

The temperature and velocity fields, weld thermal cycles, weld pool size and several solidification parameters during laser linear and spot welding of 304 stainless steel with small length scale were simulated using a comprehensive three dimensional heat transfer and fluid flow model. The following are the major conclusions:

(1) Dimensional analysis shows that the liquid metal convection continues to be an important mechanism for heat transfer within the weld pool, as the scale of the weld is reduced in linear and spot laser welding operations in comparison with conventional welds. Even with relatively small dimensions of laser welds, the Peclet number was found to be large enough for Marangoni convection to be important in the heat transfer.

(2) The weld thermal cycles for linear and spot laser welding show significantly different features. For linear welding, the heating rate initially increases with time, and the temperature reaches its peak value when the laser beam reaches directly above the monitoring location. For laser spot welding, the heating rate is very high at the beginning and then decreases gradually with increase in temperature until the laser is switched off.

(3) The practical working range of laser powers that can be used for laser welding becomes restricted as the spot size is reduced. For a given spot size, the upper and lower limits of laser powers are characterized by the peak temperature values of the boiling point and melting points of the 304 stainless steel, respectively. This range ensures welding with small length scale without contamination by metal vapor and liquid metal particles. Compared with larger welds, the allowable range of laser power for laser welding with small length scale is much narrower if keyhole behavior is to be avoided.

(4) A desired weld attribute such as the peak temperature or weld penetration may be obtained through various combinations of welding variables such as laser power and beam radius. The existence of multiple paths to attain a given weld attribute indicates the flexibility of the laser welding process with small length scale.

(5) For laser linear welding, the values of G/R along the mushy zone/liquid interface are shown to increase with the increase in net heat input. The average cooling rate from 800 to 500 °C is directly proportional to the welding speed when the laser

power and laser beam size are constant. For laser spot welding, the size of the mushy zone, i.e., liquid + solid two-phase region, grows significantly with time during solidification, and the maximum size of the mushy zone is reached when the pure liquid region vanishes. The temperature gradient decreases and the solidification rate increases with the progress of solidification. The temperature gradient and average cooling rate between 800 and 500 °C for typical laser spot welding are much higher than those in typical linear laser welding with small length scale.

4.4 References

1. W. S. Chang and S. J. Na, *J. Mater. Proc. Tech.*, **120**, 208 (2002).
2. M. J. Jackson and W. O'Neill, *J. Mater. Proc. Tech.*, **142**, 517 (2003).
3. K. Uenishi, M. Seki, M. Takatsugu, T. Kunimasa, K. F. Kobayashi, T. Ikeda and A. Tsuboi, *Mater. Trans.*, **43**, 3083 (2002).
4. S. Bednarczyk, R. Bechir and P. Baclet, *Appl. Phys. A: Mater. Sci. Process.*, **69**, S495 (1999).
5. H. J. Booth and J. Mater, *Thin Solid Films*, **453-454**, 450 (2004).
6. S. Ahn, D. W. Kim, H. S. Kim and S. J. Ahn and J. Cho, *Microelecton. Eng.*, **69**, 57 (2003).
7. P. Sahoo, M. M. Collur and T. DebRoy, *Metall. Trans. B*, **19B**, 967 (1988).
8. A. Paul and T. DebRoy, *Metall. Trans. B*, **19B**, 851 (1988).
9. P. A. A. Khan and T. DebRoy, *Metall. Trans. B*, **15B**, 641 (1984).
10. A. M. M. Collar, A. Paul and T. DebRoy, *Metall. Trans. B*, **18B**, 733 (1987).
11. T. Zacharia, S. A. David, J. M. Vitek and T. DebRoy, *Weld. J.*, **68**, 499s (1989).
12. K. Mundra and T. DebRoy, *Metall. Trans. B*, **24B**, 145 (1993).
13. K. Mundra, T. DebRoy, S. S. Babu and S. A. David, *Weld. J.*, **76** 163s (1997).
14. T. Hong, T. DebRoy, S. S. Babu and S. A. David, *Metall. Trans. B*, **31B**, 161 (2000).

15. H. Zhao and T. DebRoy, *Metall. Trans. B*, **32B**, 163 (2001).

16. Z. Yang, S. Sista, J. W. Elmer and T. DebRoy, *Acta Mater.*, **48**, 4813 (2000).

17. Z. Yang and T. DebRoy, *Sci. Technol. Weld. Joining*, **2**, 53 (1997).

18. Z. Yang and T. DebRoy, *Metall. Mater. Trans. B*, **30B**, 483 (1999).

19. W. Zhang, J. W. Elmer and T. DebRoy, *Scripta Mater.*, **46**, 753 (2002).

20. S. Sista and T. DebRoy, *Metall. Mater. Trans. B*, **32B**, 1195 (2001).

21. S. Sista, Z. Yang and T. DebRoy, *Metall. Mater. Trans. B*, **31B**, 529 (2000).

22. T. Hong, W. Pitscheneder and T. DebRoy, *Sci. Technol. Weld. Joining,* **3**, 33 (1998).

23. T. Hong and T. DebRoy, *Metall. Mater. Trans. B*, **34B**, 267 (2003).

24. K. Mundra, J. M. Blackburn and T. DebRoy, *Sci. Technol. Weld. Joining*, **2**, 174 (1997).

25. T. A. Palmer and T. DebRoy, *Metall. Trans. B*, **31B**, 1371 (2000).

26. P. W. Fuerschbach and G. R. Eisler, *Sci. Technol. Weld. Joining*, **7**, 241 (2002).

27. D. Peckner and I. M. Bernstein, *Handbook of Stainless Steels* (New York: McGraw-Hill Book Company, 1977).

28. J. R. Davis, *Metals Handbook* (Materials Park: ASM International, 1998).

29. J. R. Davis, *ASM Specialty Handbook. Stainless Steel* (Materials Park: ASM International, 1994).

30. ASM International Handbook Committee, *Metals Handbook. Volume 1. Properties and Selection: Ion, steels, and high-performance alloys* (Materials Park: ASM International, 1990).

31. W. Zhang, G. G. Roy, J. W. Elmer and T. DebRoy, *J. Appl. Phys.*, **93**, 3022 (2003).

32. T. DebRoy and S. A. David, *Rev. Mod. Phys.*, **67**, 85 (1995).

33. L. A. Betram, *J. Eng. Mater. Technol.*, **115**, 24 (1993).

34. S. A. David and T. DebRoy, *Science*, **257**, 497 (1992).

35. G. H. Geiger and D. R. Poirier, *Transport Phenomena in Metallurgy* (London: Addison-Wesley publishing company, 1973).

36. Ø. Grong, *Metallurgical Modeling of Welding* (London: The Institute of Materials, 1997).

37. W. Zhang, J. W. Elmer and T. DebRoy, *Mater. Sci. Eng. A*, **A333**, 320 (2002).

38. S. Kou, *Welding Metallurgy* (New York: John Wiley and Sons, 2002).

39. R. W. Messler, *Principles of Welding* (New York: Wiley, 1999).

40. K. Prasad, *J. Mater. Sci. Lett.* **9**, 675 (1990).

41. K. Easterling, *Introduction to the Physical Metallurgy of Welding* (London: Butterworths, 1983).

42. L. E. Svensson, B. Gretoft and H.K.D.H. Bhadeshia, *Scand. J. Metall.*, **15**, 97 (1986).

Chapter 5

PROBING TEMPERATURE DURING LASER SPOT WELDING FROM VAPOR COMPOSITION AND MODELING

Laser spot welding is characterized by a highly transient nature and a very short process duration. The welding is often completed in a few milliseconds and the heating and cooling rates attained are many times higher than those typical in steady-state linear laser welding processes. Knowledge of temperature and velocity fields, solidification rate and thermal cycle are important to determine the geometry, composition, structure and the resulting properties of the spot welds. Experimental measurements of temperature and velocity fields during laser spot welding are difficult because of the insufficient time for measurement and the highly transient nature of the welding process. In addition, the weld pool is often covered by a metal vapor plume. Because of these difficulties, no generally available technique has been developed to date to measure temperature and velocity fields in the weld pool during laser spot welding.

During high energy laser beam welding of important engineering alloys, the metal in the weld pool can be heated to very high temperatures, and significant vaporization of volatile alloying elements often takes place from the weld pool surface [1-11]. The loss of alloying elements can result in significant changes in the microstructure and degradation of mechanical properties of weldments. During welding of stainless steels, the main constituents of the metal vapor are iron, manganese, chromium and nickel [8-11]. In high manganese stainless steels, such as AISI 201, iron and manganese are the prominent vapor species in the welding environment. In order to minimize the mass loss during high power laser welding, it is necessary to quantitatively understand the role of various factors that affect the alloying element vaporization. The most important factors in determining the rate of vaporization of different elements are the temperature distribution on the surface and the weld metal chemical composition.

During laser welding, a strong spatial gradient of temperature exists on the weld pool surface. The resulting gradient of surface tension is the main driving force for the strong recirculating flow of molten metal in the weld pool [12-14]. In addition, the buoyancy force resulting from the spatial variation of density also contributes to the motion of the weld pool, although to a much lesser extent than the surface tension gradient. Because of the strong recirculating flow, the weld pool can be reasonably assumed to be well mixed and compositionally homogeneous. For a weld pool of known composition, the vaporization rates of various alloying elements are strongly affected by the surface temperatures. Since the middle region of the weld pool surface is at a much higher temperature than the periphery, it is fair to expect that much of the vaporized species originate from the middle of the weld pool surface. Since the relative rates of vaporization of two alloying elements are determined by the local temperature, the measured vapor composition can provide a rough idea of the peak temperature at the weld pool surface.

In this chapter, recent theoretical and experimental research to estimate weld pool temperatures are described. A transient, three-dimensional numerical heat transfer and fluid flow model has been used to calculate the temperature fields in the weld pool. Composition of the metal vapor from the weld pool has been determined by condensing a portion of the vapor on the inner surface of a both-end-open quartz tube which was mounted perpendicular to the sample surface and co-axial with the laser beam. The vapor composition was used to determine an effective temperature of the weld pool for various welding conditions. This technique has been shown to be a useful method to determine rough values of peak temperature during laser spot welding. No other reliable method for the estimation of peak temperature during laser spot welding has emerged so far because of the very short duration and highly transient nature of the laser spot welding process.

5.1 Experimental Procedure

Several 304 stainless steel laser spot welds were fabricated at the Sandia National Laboratories. The alloy composition was: 1 wt% Mn, 18.1 wt% Cr, 8.6 wt% Ni, 0.69

wt% Si, 0.046 wt% C, 0.012 wt% P, 0.003 wt% S, and balance Fe. A schematic diagram of the experimental set-up is presented in Fig. 5.1. During laser spot welding, a cylindrical 6 mm inner diameter by 25 mm long, open-ended quartz tube was placed co-axial to the laser beam and right above the 304 stainless steel samples. The vaporized elements were collected as condensation on the interior surface of the tube. A Raytheon SS 525 pulsed Nd:YAG laser was used for laser spot welding with pulse energies of 2.12 J and 3.19 J and pulse durations of 4.0 ms and 3.0 ms, respectively. The laser beam was focused inside the quartz tube with a 100 mm focal length lens. For each combination of energy and duration, the laser beam was defocused to different extents to obtain various spot diameters and power densities. To increase the amount of vapor condensate collected, 50 individual spot welds were made on each of the 3 by 10 by 17 mm samples. The spot welds were made in ambient air since it was impractical to provide inert gas shielding inside the quartz tube for each spot weld. The experimental parameters are indicated in Table 5.1.

Table 5.1: Welding parameters.

Sample number	Pulse energy (J)	Beam radius (mm)	Power density (W/mm^2)	Pulse duration (ms)
E	2.12	0.289	2020	4
B/F	2.12	0.247	2765	4
C	2.12	0.227	3274	4
D	2.12	0.171	5769	4
G	3.19	0.326	3185	3
A	3.19	0.28	4317	3

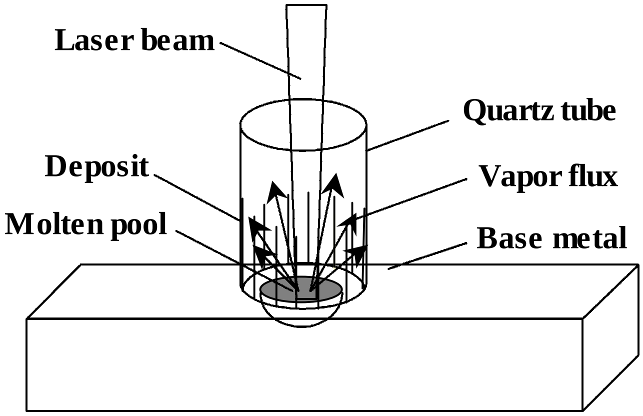

Fig. 5.1: A schematic diagram of the experimental setup.

The quartz tube samples were examined using the JEOL 8600 Electron Microprobe X-ray Analyzer to determine the vapor composition. The evaporation products had the consistency of fine dust. The quartz tubes were broken, and a suitable fragment from each experiment was mounted to expose the deposit. Due to the geometry of the samples and their highly porous nature, the probe was not operated in an automated mode. Instead, a series of spot measurements of the K-values (count rate ratios of unknown to standards) were made on each sample. The K-value measurements were converted to approximate oxide ratios and averaged together for each sample.

5.2 Results and Discussion

The local evaporation flux of an alloying element based on the Langmuir equation is expressed as [15]:

$$J_i = \frac{\alpha P_i}{\sqrt{2\pi M_i RT}} \tag{5.1}$$

where α is a positive constant with a maximum value of 1 that accounts for the inevitable condensation of a portion of the vaporized atoms on the surface at pressures higher than perfect vacuum, and P_i is the partial pressure of i over the alloy. The meanings of the other parameters are the same as those in Equation 2.14**.** At pressures close to atmospheric pressure, the value of α cannot be estimated from fundamental principles. The lack of knowledge of α poses a problem in the application of the Langmuir equation for quantitative calculation of the vaporization rates of individual alloying elements. However, since the relative vaporization rates of any two alloying elements is independent of α, the Langmuir equation can be used for predicting the relative vaporization rates of various alloying elements:

$$\frac{J_i}{J_j} = \frac{P_i}{P_j}\left(\frac{M_j}{M_i}\right)^{\frac{1}{2}} \tag{5.2}$$

The equilibrium partial pressure P_i over the alloy depends upon the composition and the temperature of the weld metal. The equilibrium vapor pressures of the alloying elements over the respective pure liquids are presented in Table 5.2**.** In these equations, the temperature is expressed in K. Assuming that the solution is ideal at high temperatures, the equilibrium vapor pressures of the various species over the alloy can be expressed as:

$$P_i = X_i P_i^0 \tag{5.3}$$

where X_i is the mole fraction of element i in the alloy, and P_i^0 is the equilibrium vapor pressure of element i over the pure liquid, which can be obtained from Table 5.2. The vapor pressures of the alloying elements over pure liquids and over 304 stainless steel are presented in Fig. 5.2. It can be seen from Fig. 5.2(a) that among the four alloying elements, manganese has the highest vapor pressure over its pure liquid in the entire temperature range studied. However, its vapor pressure over the alloy is lower than those of iron and chromium, as observed from Fig. 5.2(b). This is because manganese only accounts for 1.0 wt % in 304 stainless steel while iron and chromium are present at 72.3 and 18.1 wt%, respectively. It can be seen from Fig. 5.2(b) that over liquid stainless steel, iron is the dominant vaporizing species, followed by chromium and manganese. The vapor pressure of nickel over the alloy is very low. Vapor pressures of all the alloying elements are strong functions of temperature.

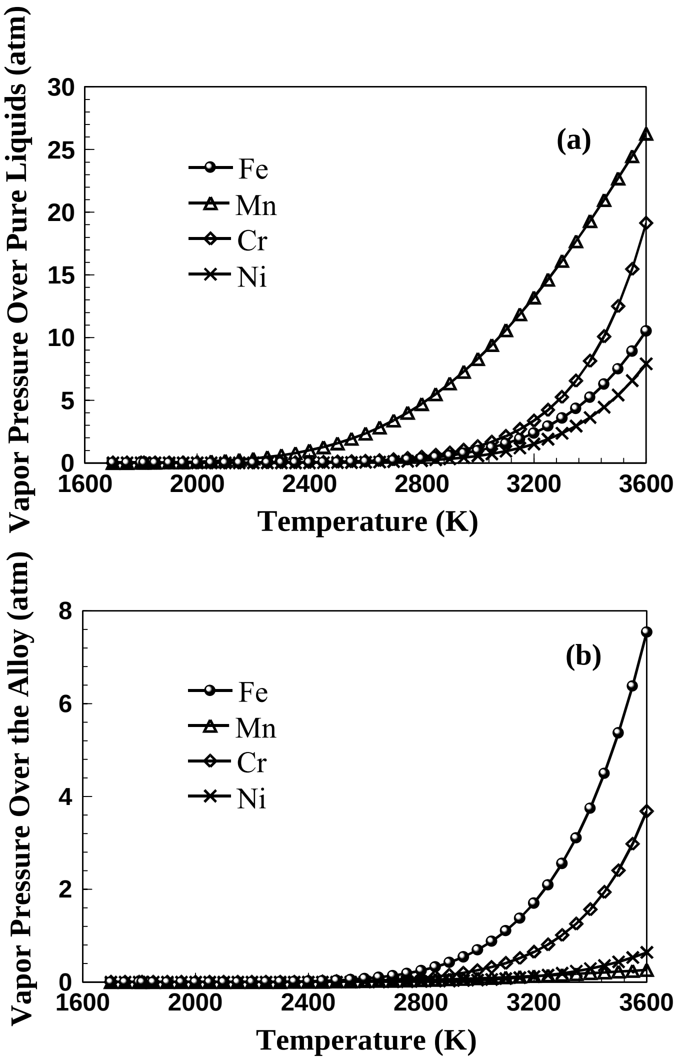

Fig. 5.2: Equilibrium vapor pressures of the four alloying elements (a) over respective pure liquids and (b) over 304 stainless steel at different temperatures. Data used are indicated in Table 5.2 [16-19].

Table 5.2: Vapor pressure of different elements as a function of temperature. The temperature is expressed in K.

Elements	The equilibrium vapor pressures over pure liquid (atm)	Reference
Fe	$\log(P^0 \times 760) = 11.5549 - 1.9538\times10^4 / T - 0.62549\log T$ $- 2.7182\times10^{-9} T + 1.9086\times10^{-13} T^2$	[16]
Mn	$\log(P^0 \times 1.013\times10^5) = -5.58\times10^{-4} T - 1.503\times10^{-4} / T + 12.609$	[17]
Cr	$\log(P^0 \times 1.013\times10^5) = -13.505\times10^3 / T + 33.658\log T$ $- 9.29\times10^{-3} T + 8.381\times10^{-7} T^2 - 87.077$	[18]
Ni	$\log P^0 = 6.666 - 20765/T$	[19]

The extent of variation of the equilibrium partial pressures resulting from temperature change is different for different elements. Since the vaporization flux of the individual elements are proportional to their equilibrium partial pressures, the ratio of the vaporization flux of any two elements can be a strong function of temperature. Consequently, if the vapor composition, i.e., the ratio of the vaporization flux of any two elements is known, the weld pool temperature can be determined. The experimentally determined concentrations of iron, manganese and chromium in the vapor condensate as a function of laser power density are shown in Figs. 5.3(a), (b) and (c), respectively. Fig. 5.3(a) shows that as the power density increases, the concentration of Fe in the vapor condensate also increases. This is because the slope of the vapor pressure versus temperature plot for iron is steeper than those of the other alloying elements, as shown in Fig. 5.2(b). For similar reasons, the concentration of chromium in the vapor condensate increases slightly with power density. On the other hand, the concentration of manganese decreases with power density. Again, the reason for this behavior can be traced to the manner in which the equilibrium vapor pressure of manganese varies with temperature relative to other alloying elements.

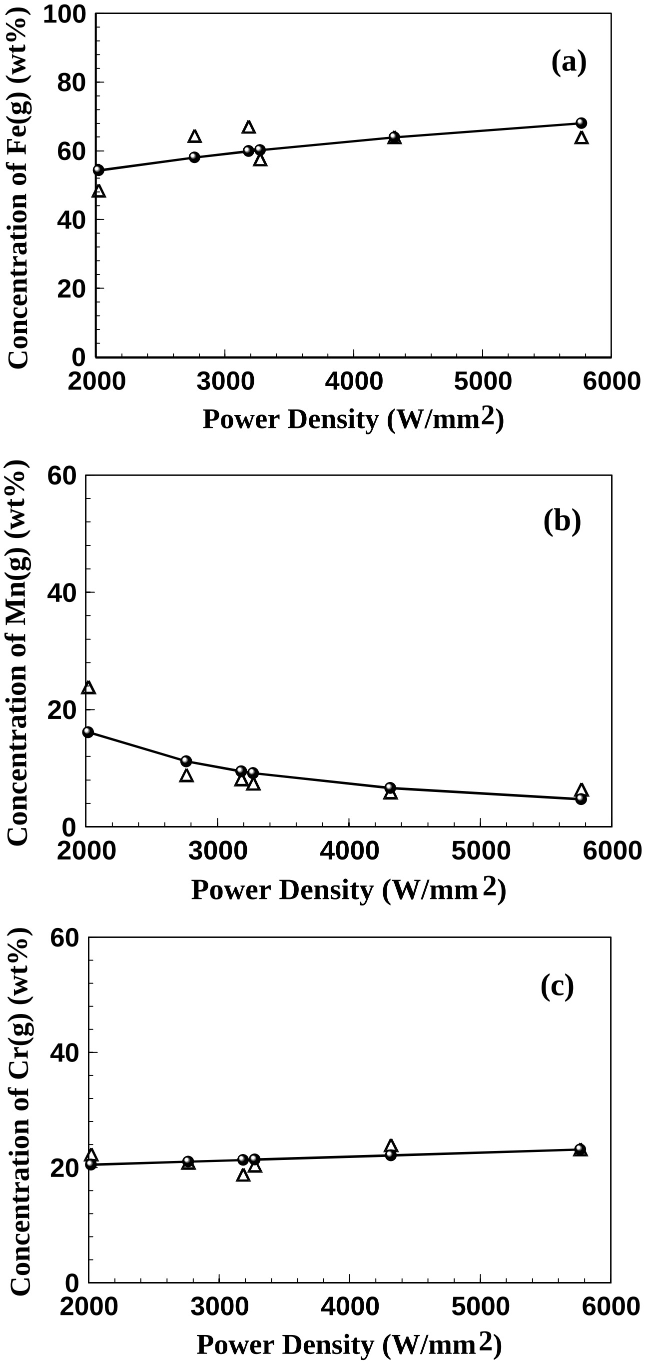

Fig. 5.3: Measured weight percent of (a) Fe, (b) Mn and (c) Cr in vapor composition with laser power density. The triangles represent the original data, and the circles show best fit. Welding parameters are shown in Table 5.1.

Using the vapor pressures of various alloying elements over liquid stainless steel presented in Fig. 5.2(b), the values of J_{Fe}/J_{Mn} and J_{Cr}/J_{Mn} are calculated from Equation 5.2 as a function of temperature. The computed values are shown in Fig. 5.4. It is observed that both the ratios of the vaporization fluxes depend strongly on temperature. So, if the vapor composition is known, an effective temperature of the weld pool can be determined. Using the experimentally determined vapor composition data presented in Figs. 5.3(a), (b) and (c) and the J_{Fe}/J_{Mn} and J_{Cr}/J_{Mn} versus temperature plots in Fig. 5.4, effective weld pool temperatures can be determined for various power densities. The results are shown in Fig. 5.5. It can be observed that the temperatures calculated from J_{Fe}/J_{Mn} are in good agreement with those obtained from J_{Cr}/J_{Mn} indicating that the estimated effective temperatures are independent of the choice of element pairs.

What does the effective temperature mean? Let us consider a relatively simple isothermal system where the vaporization of alloying elements occurs from the surface of a stainless steel melt. The relative vaporization rates as a function of temperature would be given by Fig. 5.4. Since the vapor composition at the effective vaporization temperature is the same as that obtained from the welding experiment, the effective temperature can be defined as a temperature that results in the same vapor composition as the welding experiment. During welding, the vapors originate from the entire weld pool surface where there is a strong variation of temperature. Since the vaporization rate increases strongly with temperature, most of the vapors originate from the middle of the weld pool. Furthermore, the temperature profile changes with time. It is shown in Fig. 4.4 that for the conditions of the experiments described, the surface temperature change is most pronounced in the first millisecond. The temperature change slows down considerably after that time. As a result, most of the vapor comes from the later portion of the thermal cycle when the temperature is fairly close to the value at the end of the pulse. In short, since much of the vapor originates from the middle of the weld pool surface and towards the end of the pulse, the effective temperature is expected to be fairly close to the peak temperature.

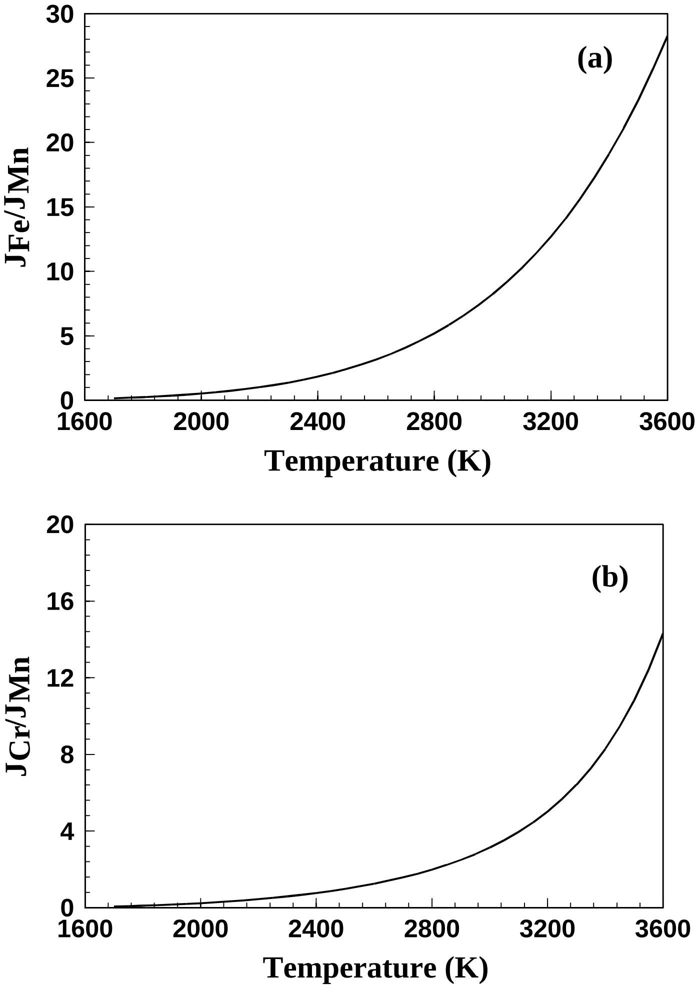

Fig. 5.4: The ratio of calculated vaporization rates of (a) Fe and Mn and (b) Cr and Mn as a function of temperature.

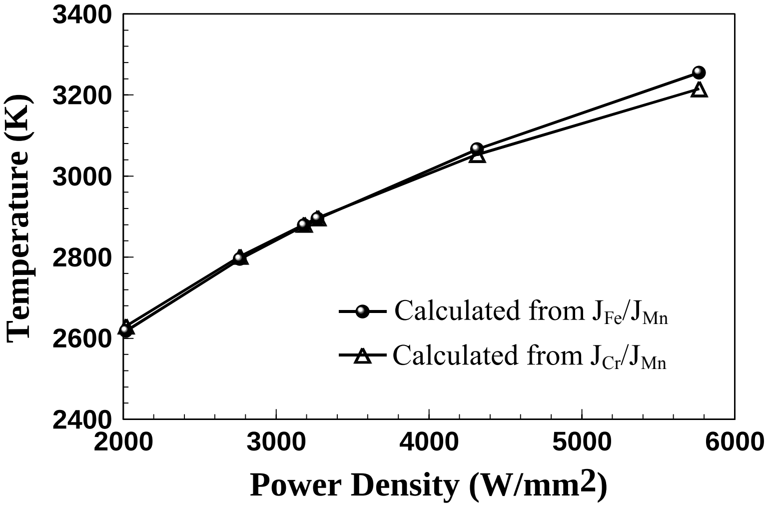

Fig. 5.5: Temperature values calculated from the ratio of vapor flux. The power density is defined as the ratio of power and laser beam area. Welding parameters are shown in Table 5.1.

The experimental and calculated values of weld pool depth and width for various laser power densities are presented in Fig. 5.6. The total power was kept constant at 1967 W, while the beam radius was varied to obtain different power densities. It can be seen that the calculated weld pool depth and width show good agreement with the experimental results at low power densities. However, at high power densities, there is some difference between the calculated and the experimental values of the weld pool depth. In order to understand the reason for the discrepancy, the experimental ratio of the weld pool depth to half-width is presented in Fig. 5.7. It is observed that the ratio varied between 0.4 to 0.7 at power densities below 3500 W/mm^2, while this value increased to over 1.0 at higher power densities. Weld pool depths higher than the half-width are often obtained when the surface of the weld pool is significantly depressed from its nearly flat position. Such depressions are common at high power densities because the high vapor flux exerts significant recoil force on the weld pool surface. In extreme cases, when the recoil force exceeds the surface tension force, fine metal droplets are ejected from the weld pool. Significant loss of mass due to vaporization and metal particle ejection can occur at high power densities, which will be discussed in the next two chapters. However, the difference between the experimental and the computed values of weld pool depth at power densities higher than 3500 W/mm^2 is consistent with the mass loss due to vaporization and particle ejection. At lower power densities, experimentally measured and computed values of weld pool depth and width agree better with the corresponding measured values.

The variation of the peak temperature with power density, computed from numerical heat transfer and fluid flow model, is shown in Fig. 5.8. The peak temperature represents the highest values on the weld pool surface at the end of the pulse. It is also observed from this figure that for the same power energy and same pulse duration, a higher pulse density results in higher peak temperature. The comparison of peak temperature calculated from the numerical heat transfer and fluid flow model with the effective weld pool temperature estimated from the vapor composition is shown in Table 5.3. It can be seen that the temperatures from the model are in fair agreement with the effective temperatures determined from the vapor composition. Thus, the vapor composition can provide a useful estimate of the weld pool peak temperature.

Table 5.3: Temperatures calculated from vapor compositions and numerical model.

Sample	Power (W)	Radius (mm)	Power density (W/mm^2)	Temperature (K)		
				By transient model	By the value of J_{Fe}/J_{Mn}	By the value of J_{Cr}/J_{Mn}
E	530	0.289	2020	2388	2625	2605
B/F	530	0.247	2765	2559	2800	2775
C	530	0.227	3274	2661	2900	2870
D	530	0.171	5769	3058	3265	3190
G	1063.3	0.326	3185	2888	2885	2855
A	1063.3	0.28	4317	3145	3075	3030

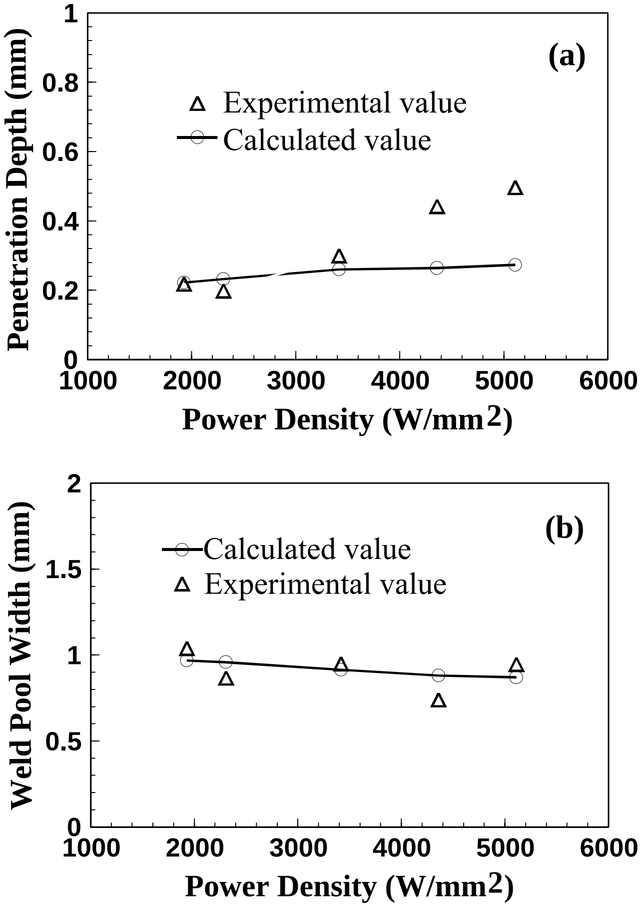

Fig. 5.6: The effects of laser power density on (a) the weld pool depth, (b) the weld pool width and (c) the weld pool volume. The power density is defined as the ratio of power and laser beam area. Laser power: 1967 W, and pulse duration: 3.0 ms. Data used in calculation are shown in Table 4.2.

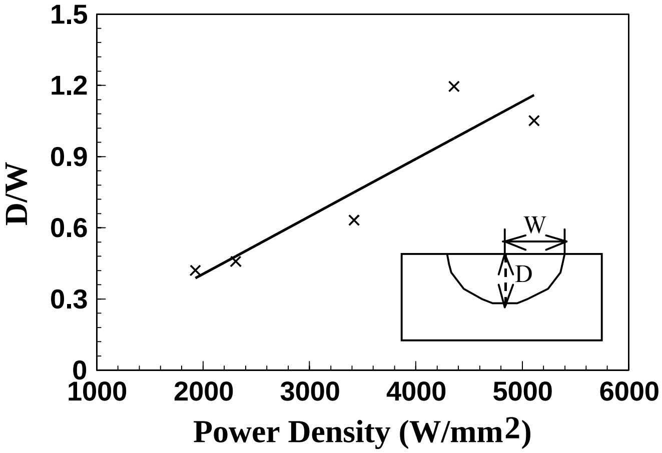

Fig. 5.7: The variation of D/W with laser power density. Laser power: 1967 W, and pulse duration: 3.0 ms. Data used in calculation are shown in Table 4.2.

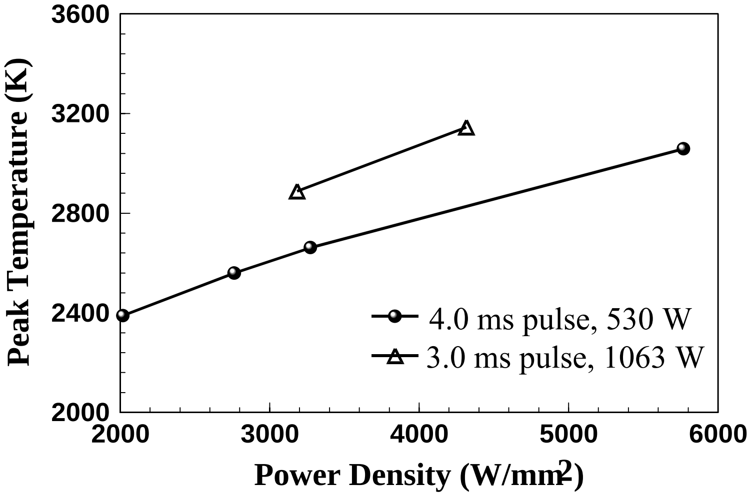

Fig. 5.8: The variation of peak temperature on the weld pool surface with laser power density. Welding parameters are shown in Table 5.1. Data used in calculation are shown in Table 4.2.

5.3 Summary and Conclusions

Weld pool peak temperature during laser spot welding of 304 stainless steel has been investigated experimentally and theoretically. Experimental work involved determination of the composition of the metal vapor by condensing a portion of the vapor on the inner surface of an open-ended quartz tube which was mounted perpendicular to the sample surface and co-axial with the laser beam. Iron, chromium and manganese were identified as the main metallic species in the vapor phase. Relative to the alloy composition, the concentrations of Fe and Cr in the vapor increased slightly while the concentration of Mn in the vapor decreased somewhat with the increase in power density. The vapor composition was used to determine an effective temperature of the weld pool. The effective temperature determined from the vapor composition was found to be close to the numerically computed peak temperature at the weld pool surface using the three-dimensional, transient, numerical model. Estimation of the approximate values of peak temperature during laser spot welding by measuring vapor composition overcomes the problems encountered in direct measurement of peak temperatures.

5.4 References

1. A. Block-Bolten and T. W. Eagar, *Metall. Trans. B*, **15B**, 461 (1984).
2. G. J. Dunn, C. D. Allemand and T. W. Eagar, *Metall. Trans.*, **17A**, 1851 (1986).
3. G. J. Dunn and T. W. Eagar, *Metall. Trans.*, **17A**, 1865 (1986).
4. A. Blake and J. Mazumder, *J. Eng. Ind.*, **107**, 275 (1985).
5. D. W. Moon and E. A. Metzbower, *Weld. J.*, **62**, 53s (1983).
6. M. J. Cieslak and P. W. Fuerschbach, *Metall. Trans. B*, **19B**, 319 (1988).
7. H. Zhao and T. DebRoy, *Metall. Trans. B*, **32B**, 163 (2001).

8. K. Mundra and T. DebRoy, *Metall. Trans. B*, **24B**, 145 (1993).

9. P. A. A. Khan and T. DebRoy, *Metall. Trans. B*, **15B**, 641 (1984).

10. M. M. Collur, A. Paul and T. DebRoy, *Metall. Trans. B*, **18B**, 733 (1987).

11. S. Basu and T. DebRoy, *J. Appl. Phys.*, **72**, 3317 (1992).

12. S. A. David and T. DebRoy, *Sci.*, **257**, 497 (1992).

13. T. DebRoy and S. A. David, *Rev. Mod. Phys.*, **67**, 85 (1995).

14. H. Zhao, D. R. White and T. DebRoy, *Int. Mater. Rev.*, **44**, 238 (1999).

15. S. Dushman, *Scientific Foundations of Vacuum Technique* (New York: Wiley, 1962).

16. C. L. Yaws, *Handbook of Vapor Pressure* (Houston: Gulf Pub. Co., 1994).

17. R. Hultgren, P. D. Desai, D. T. Hawkins, M. Gleiser, K. K. Kelley and D. D. Wagman, *Selected Values of the Thermodynamic Properties of the Elements* (Metals Park: American Society for Metals, 1973).

18. P. E. Honig and D. A. Kramer, *Physicochemical Measurements in Metal Research* (New York: Interscience Publishers, 1970).

19. C. B. Alcock, V. P. Itkin and M. K. Horrigan. *Can. Metall. Q.*, **23**, 309 (1984).

Chapter 6

ALLOYING ELEMENT VAPORIZATION AND LIQUID METAL EXPULSION DURING LASER SPOT WELDING

Joining of very small metallic components is often accomplished with short laser pulses of only a few milliseconds duration. Laser spot welding is characterized by its small length scale, fairly short duration, highly transient nature, and very high heating and cooling rates. Because of the high power density used, the weld metal is rapidly heated to very high temperatures and, as a consequence, significant vaporization of volatile alloying elements often takes place from the weld pool surface [1-11]. If the weld pool temperature is very high, the escaping vapor exerts a large recoil force on the weld pool surface [11]. As a consequence, the molten metal may be expelled from the weld pool. Vaporization and liquid metal expulsion [11-20] are the two main mechanisms of material loss during laser microjoining. The loss of alloying elements can result in significant changes in the microstructure and degradation of mechanical properties of weldments [4-6]. In the electronics industry, where components are often processed in a clean room environment, discharge of metal vapors is not acceptable. During laser assisted joining of components, loss of alloying elements needs to be minimized. Therefore, quantitative understanding of the evaporation of alloying elements and liquid metal expulsion is important in the welding of engineering alloys.

Most previous work on vaporization calculation paid more attention to linear laser welding. Vaporization of alloying elements during laser spot welding is different from that during linear welding in several ways. First, the evaporation rate is strongly time-dependent, i.e., the rate is negligible at the initiation of the pulse and gradually increases owing to increase in temperature. Second, because of the short duration of the laser pulse, experimental determination of temperature and velocity fields is difficult and remains both an important goal and a major challenge in the field. Third, although both the surface area and the volume of the weld pool are small, they change significantly with time. As a result of these difficulties, very little information is available in the literature about measurements of important variables such as the temperature field during laser spot welding.

As discussed in the last chapter, once the liquid pool forms, a strong spatial gradient of temperature exists on its surface. The resulting gradient of surface tension is the main driving force for the recirculating flow of molten metal in the weld pool. In addition, the buoyancy force resulting from the spatial variation of density also contributes to the motion of the weld pool, although to a much lesser extent than the surface tension gradient. Because of the strong recirculating flow, the weld pool can be reasonably assumed to be well mixed and compositionally homogeneous. For a weld pool of known composition, the vaporization rates of various alloying elements are strongly affected by the surface temperatures. In order to minimize the mass loss during high power laser welding, it is necessary to quantitatively understand the role of various factors, such as the temperature distribution on the surface, weld metal chemical composition and surface area, that affect vaporization of alloying elements during laser spot welding.

In this paper, the temperature fields used to calculate the loss of material were obtained from the comprehensive three dimensional transient numerical heat transfer and fluid flow model. Using the computed temperature fields, vaporization rate, composition change and total mass loss due to vaporization of various alloying elements resulting from both concentration and pressure driven transport during laser spot welding were calculated. Both vaporization and condensation of the metal vapor on the weld pool surface were considered in the model. The experimentally determined vapor composition, weld pool composition change and overall vaporization loss were compared with the corresponding modeling results. The conditions necessary for the initiation of liquid metal expulsion were determined by balancing the vapor recoil force with the surface tension force at the periphery of the liquid pool. The influences of laser power density and pulse duration on liquid metal expulsion were analyzed. In addition, the free surface profile was simulated at different times by minimizing the total surface energy.

6.1 Experimental Procedure

The composition of 304 stainless steel, laser beam energy and beam size, vapor composition and experimental setup have been shown in Sections **4.1.1** and **5.1**. A portion of the vaporized elements and ejected metal droplets were collected on the interior surface of the tube. After laser spot welding, the concentrations of iron, manganese, chromium and nickel along a radial direction of the weld pool were traced by an electron microprobe. Since other alloying elements constituted less than 1 wt %, they were ignored for this investigation. The mass loss was experimentally determined by weighing each specimen before and after welding with a Metler MT5 micro-balance. To increase the accuracy of the weight loss measurements, the reported mass loss per pulse is the average of fifteen mutually independent spot welds made on each sample. The deposit and the particles were examined from each experiment. The SEM micrographs and EDS (Energy-Dispersive x-ray Spectroscopy) analysis were performed on the interior surface of the quartz tube for every experiment.

6.2 Mathematical Modeling

The temperature distribution in the weld pool has been simulated using transient heat transfer and fluid flow model, as shown in Section **3.1**. When the temperature is very high, the liquid pool severely deforms due to the recoil pressure exerted by the escaping vapor. The calculation of the free surface profile of the weld pool involves minimizing the total surface energy. The total energy includes the surface tension energy for the change in the area of pool surface, potential energy in the gravitational field and the work done by the recoil force. The total energy can be expressed as:

$$E_t = \iint_s \left(\gamma\sqrt{1+\phi_x^2+\phi_y^2} - \frac{1}{2}\rho g \phi^2 - \Delta P \phi \right) dxdy \qquad (6.1)$$

where s indicates the surface of the weld pool. On the right hand side, the three terms within the parentheses represent surface energy, potential energy and the work by the recoil force, respectively. The symbol ϕ is defined as the vertical elevation of the top surface with respect to an arbitrarily chosen horizontal plane and depends on x and y. The variables ϕ_x, and ϕ_y represent the partial derivatives of ϕ with respect to x and y, γ is surface tension, ρ is density and ΔP is the difference between the local equilibrium vapor pressure and the atmospheric pressure. The equilibrium vapor pressure data used for the calculations are available in Table 5.2. In the calculation, the total volume of liquid pool prior to liquid metal expulsion is assumed to be constant, so the constraining equation is:

$$\Delta V = \iint_s \phi dxdy = 0 \qquad (6.2)$$

6.3 Results and Discussion

6.3.1 Weld Thermal Cycle and Weld Pool Volume

When calculating the temperature on the weld pool surface, the effect of the heat loss owing to vaporization should also be considered. The rate of heat loss per unit area from the pool surface, h_v, owing to vaporization can be expressed as:

$$h_v = \sum_{i=1}^{n} J_i \Delta H_i \qquad (6.3)$$

where n is the number of alloying elements, ΔH_i is the enthalpy of vaporization of the element i, which is shown in Table 6.1. J_i is the vaporization flux of element i and can be expressed by the Langmuir equation [22]:

$$J_i = \frac{\alpha P_i}{\sqrt{2\pi M_i RT}} \qquad (6.4)$$

where P_i is the vapor pressure of i over the alloy, and α is a positive constant that accounts for the inevitable condensation of a portion of the vaporized atoms at atmospheric pressure. When the vaporization occurs in a perfect vacuum, the value of α becomes 1. The evaporation flux calculated by the Langmuir equation is usually an order of magnitude higher than the actual rate at one atmosphere pressure [**8**,**10**,**23**]. Therefore, the value of α was taken as 0.1 for the calculation of the evaporation flux. Computed peak temperatures versus time plots both considering and ignoring the heat of vaporization are presented in Fig. **6.1**. The heat loss due to vaporization per unit area was much smaller than the heat flux absorbed from the laser beam because of the high power density used in the experiments. As a result, the cooling effect of vaporization was not pronounced, i.e., vaporization did not reduce the surface temperatures significantly. For the typical experimental condition considered in Fig. **6.1**, i.e., 1967 W, 3 ms duration pulse and 0.428 mm laser beam radius, the maximum peak temperature attained at the end of the pulse was 3205 K when the cooling effect of vaporization was ignored and 3174 K when the effect was considered. For a 530 W laser beam of 0.171 mm radius pulsed for 4 ms, the peak temperatures were 3058 K and 3047 K when the cooling effect was ignored and when the effect was considered, respectively. Thus, under the conditions of the current experiments, the heat loss owing to vaporization was much smaller than the power density of the beam, and the vaporization of alloying elements did not significantly affect the computed surface temperatures.

Table **6.1**: Enthalpies of vaporization of the alloying elements.

Element	Enthalpy (kJ/mol)
Iron	340
Manganese	220
Chromium	342
Nickel	375

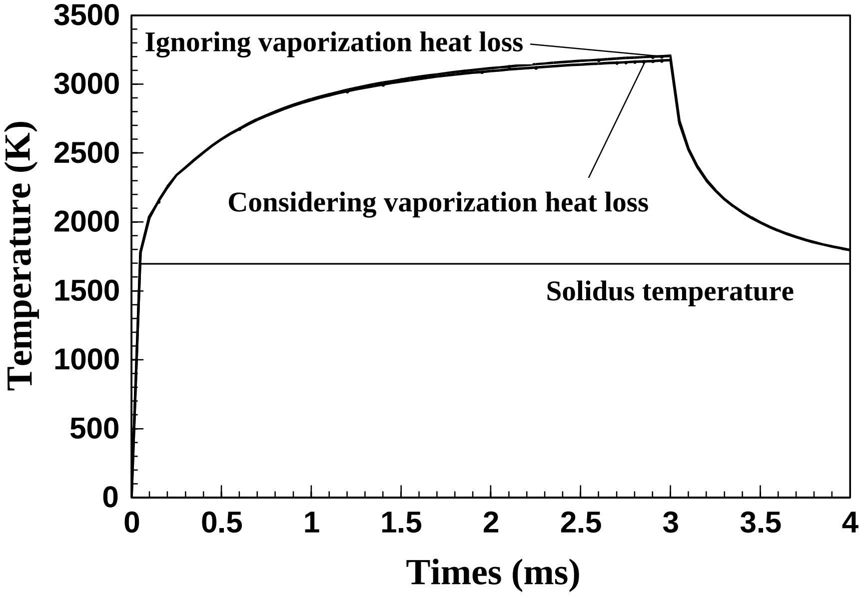

Fig. 6.1: Computed weld thermal cycles on the top surface of the weld pool. The solid horizontal line indicates solidus temperature. Laser power: 1967 W, pulse duration: 3.0 ms, and beam radius: 0.428 mm. Data used in calculation are shown in Table 4.2.

Fig. 6.2 shows changes in the computed temperatures at various monitoring locations, which are indicated as points 1, 2, 3 and 4 in the small figure. These locations represent distances of 0, 0.125, 0.175, and 0.225 mm from the axis of the laser beam, respectively. During the initial period of about 1 ms, the temperature increases rapidly and then grows slowly until the end of pulse duration. As a consequence, most of the vaporization occurs during the last two milliseconds. There are several special features of interest. First, the temperatures reach very high values near the laser beam axis. It is to be noted that the peak temperature can exceed the boiling point of the alloy, i.e., the equilibrium vapor pressure at the liquid surface can be higher than one atmosphere. Second, the computed results also indicate that the heating rates vary significantly depending on the location. Finally, as the weld metal cools, the spatial variation of the cooling rates within the solid metal is much smaller than the spatial variation in the heating rates. These features of temperature and the temperature distribution at the weld pool surface are of interest in examining the vaporization of alloying elements from the weld pool.

For laser spot welding, the volume of the weld pool is time dependent. The change of weld pool volume as a function of time is shown in Fig. 6.3. Unlike the temperature, the volume of weld pool increases almost linearly with time for the entire 3 ms period. This result clearly shows that steady state is not reached for the entire duration of the pulse. The effect of power density on the peak temperature and weld pool volume is shown in Fig. 6.4. The peak temperature in this figure is computed at the end of the pulse. It is interesting to note that the weld pool volume at the end of three milliseconds does not increase significantly above 2000 W/mm^2, while the peak temperature increases continuously even beyond this power density. Clearly, the weld pool volume is limited by the rate of heat transfer in the solid region above 2000 W/mm^2, while the deposition of higher power density locally does increase the peak temperature.

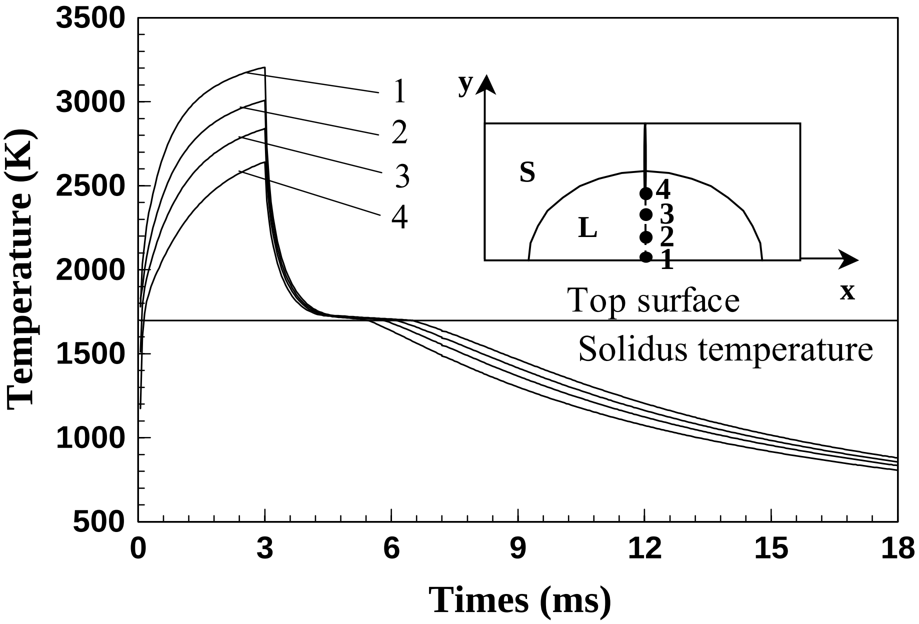

Fig. 6.2: Computed weld thermal cycles at various locations on the top surface of the weld pool. Distance from the weld center: 1: 0.0 mm; 2: 0.125 mm; 3: 0.175 mm; 4: 0.225 mm, as shown in the small figure. The solid horizontal line indicates solidus temperature. Laser power: 1967 W, pulse duration: 3.0 ms, and beam radius: 0.428 mm. Data used in calculation are shown in Table 4.2.

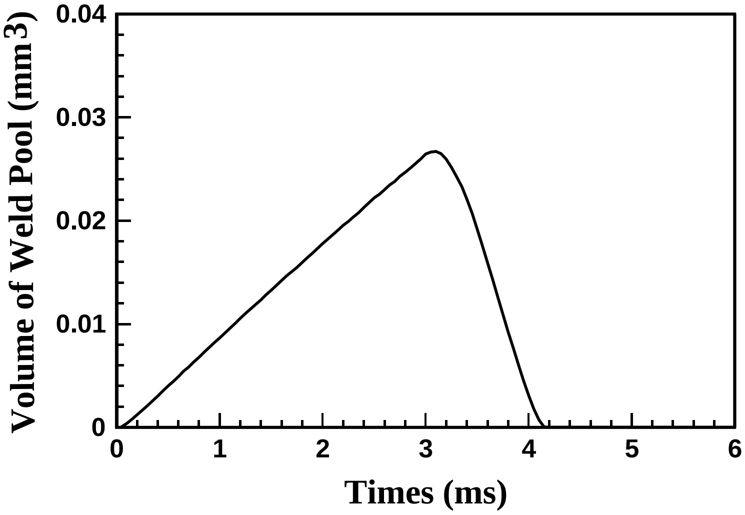

Fig. 6.3: Computed volume of weld pool as a function of time. Laser power: 1067 W, pulse duration: 3.0 ms, and beam radius: 0.26 mm. Data used in calculation are shown in Table 4.2.

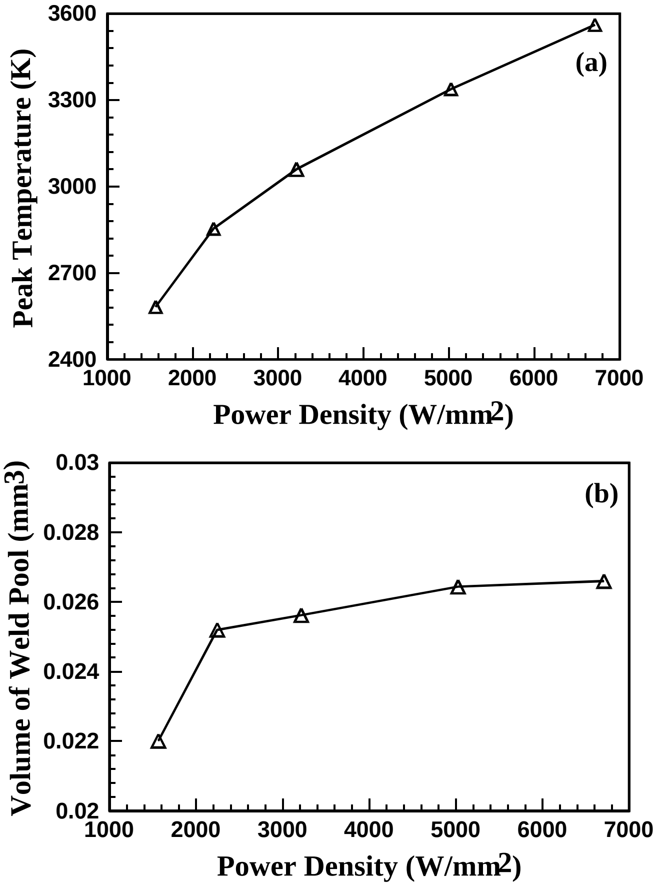

Fig. 6.4: Effects of laser power density on (a) the computed peak temperature and (b) the computed volume of weld pool. Laser power: 1067 W, pulse duration: 3.0 ms. Data used in calculation are shown in Table 4.2.

6.3.2 Vaporization Rate

Because the weld pool surface temperatures reach high values, pronounced evaporation of alloying elements takes place during high power laser spot welding. Fig. 6.5 shows the computed temperature distribution and various vapor fluxes at the weld pool surface after 3.0 ms. The total vapor flux is the sum of the fluxes of individual alloying elements resulting from both pressure driven and concentration difference driven fluxes. The results show that the distribution patterns of vapor fluxes are similar to the surface temperature profiles. This similarity is anticipated since the vapor fluxes are strongly affected by temperature. The primary driving force for vaporization is the total pressure gradient at temperatures higher than the boiling point. At lower temperatures, the vapor flux is driven mainly by diffusion in the gas phase outside the liquid pool. The calculated results show that most of the vaporization occurs from a small region near the center of the beam-workpiece interaction zone where the weld pool surface temperatures are very high as observed from Fig. 6.5(a). The diameter of this active region is approximately 0.6 mm, as can be observed from Figs. 6.5(b) through 6.5(h). This dimension is comparable but somewhat smaller than the diameter of the laser beam at the focal point.

From the computed vapor fluxes presented in Figs. 6.5(e) through 6.5(h), it can be seen that iron is the dominant vaporizing species, followed by chromium and manganese. The equilibrium vapor pressure data used for the calculations are presented in Table 5.2. Although manganese has the highest vapor pressure over its pure liquid, its concentration in 304 stainless steel is much lower than those of iron and chromium. Manganese only accounts for 1.0% of the stainless steel composition while iron and chromium are present in 72.3% and 18.1%, respectively. The lower concentration results in the lower vapor flux of manganese compared to iron and chromium over 304 stainless steel.

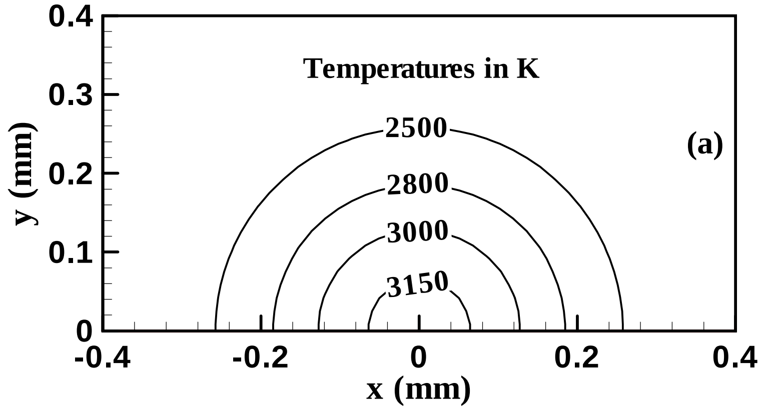
Temperatures in K
2500
2800
3000
3150
(a)
0.4
0.3
0.2
0.1
0
y (mm)
-0.4
-0.2
0
0.2
0.4
x (mm)

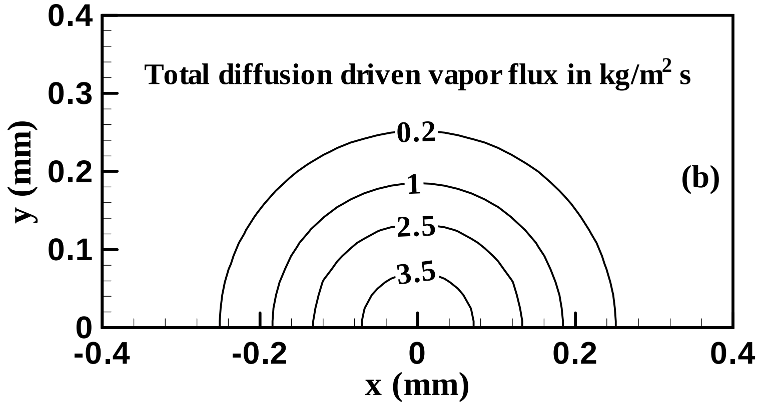
Total diffusion driven vapor flux in kg/m^2 s
0.2
1
2.5
3.5
(b)
0.4
0.3
0.2
0.1
0
y (mm)
-0.4
-0.2
0
0.2
0.4
x (mm)

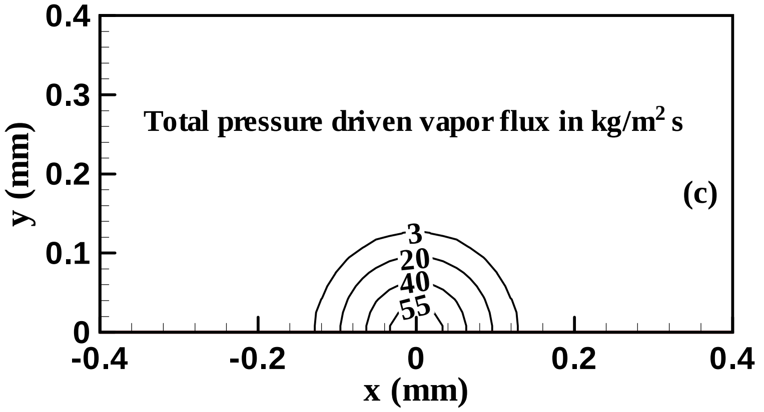
Total pressure driven vapor flux in kg/m^2 s
3
20
40
55
(c)
0.4
0.3
0.2
0.1
0
y (mm)
-0.4
-0.2
0
0.2
0.4
x (mm)

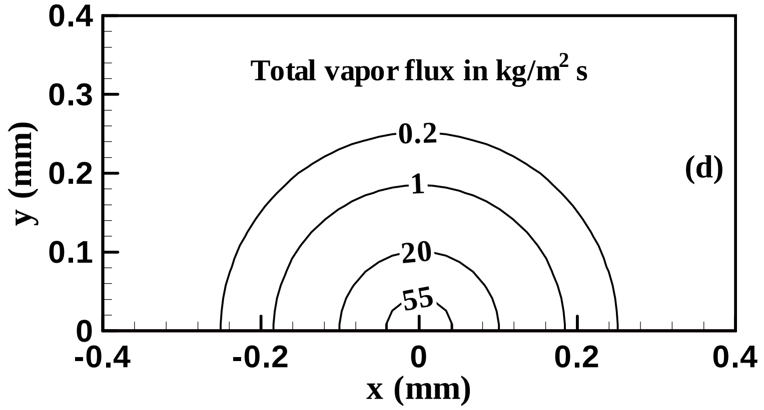
Total vapor flux in kg/m^2 s
0.2
1
20
55
(d)
0.4
0.3
0.2
0.1
0
y (mm)
-0.4
-0.2
0
0.2
0.4
x (mm)

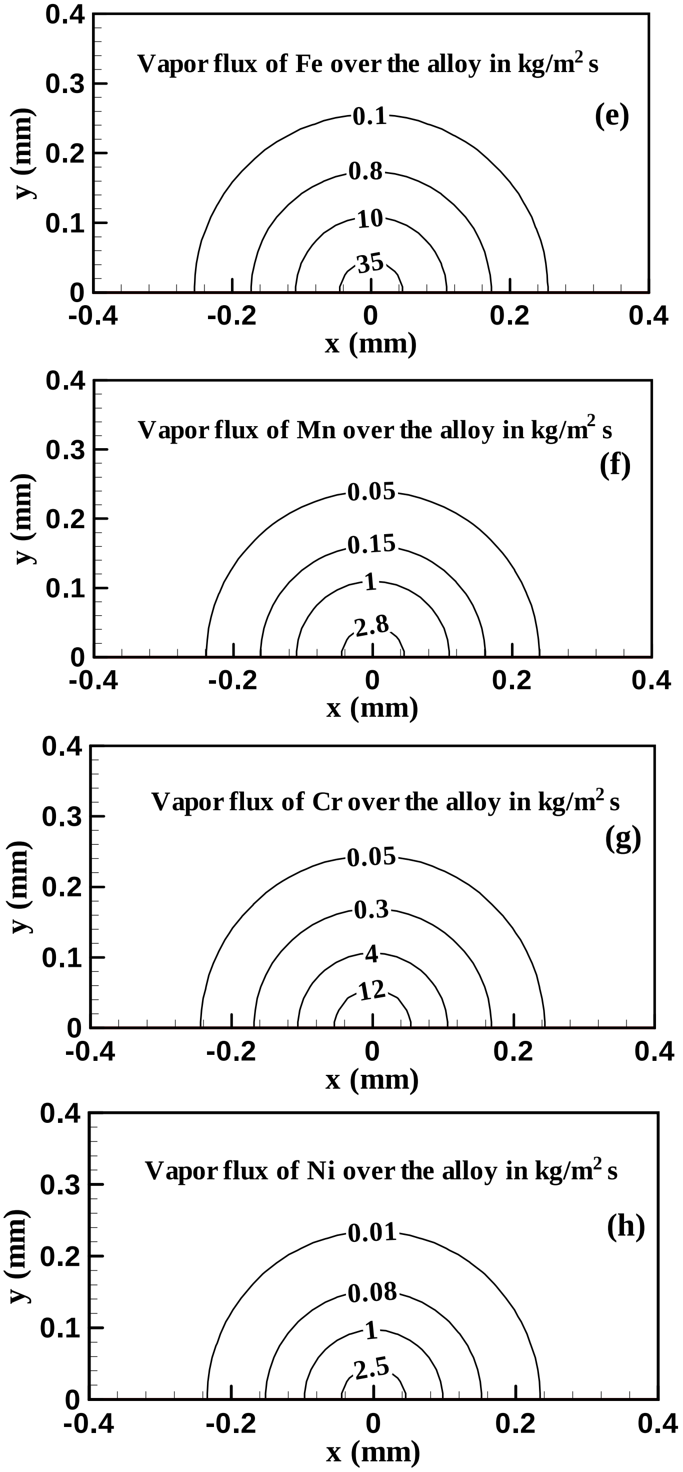

Fig. 6.5: Distributions of temperature and vapor fluxes of various elements at the weld pool surface after 3.0 ms. Laser power: 1967 W, pulse duration: 3.0 ms, and beam radius: 0.428 mm. Data used in calculation are shown in Table 4.2 and Table 5.2.

Fig. 6.6 shows the variation of vaporization rates with time calculated by the model. It can be seen that the vaporization rates of the constituent alloying elements increase with time. At the end of the pulse cycle, vaporization rates decrease suddenly, and the vaporization of alloying elements stops. The time-dependent vaporization rate is determined by the changes in the temperature distribution at the surface of the weld pool. From Fig. 6.6, it can be also seen that iron is the main vaporizing species, followed by chromium and manganese. Although manganese has the highest vapor pressure over its pure liquid, its low equilibrium vapor pressure over the alloy results in a lower vaporization rate than iron and chromium.

6.3.3 Vapor Composition

The concentrations of different elements in the vapor obtained from both experiments and calculations are presented in Fig. 6.7. Iron and chromium are the main vaporizing species. It is also observed that the calculated concentrations of various vaporizing species agree well with those obtained from measurements. The experimentally determined and the calculated concentrations of different alloying elements in the vapor for various welding conditions are presented in Table 6.2. The change in the concentrations of the main vaporizing species, i.e., iron and chromium, with power density is shown in Fig. 6.8. Generally, as the power density increases, the concentration of iron in the vapor increases. This is mainly because of the slope of the vapor pressure versus temperature plot for iron is steeper than those of the other alloying elements. For a similar reason, the concentration of chromium in the vapor condensate also increases slightly with power density.

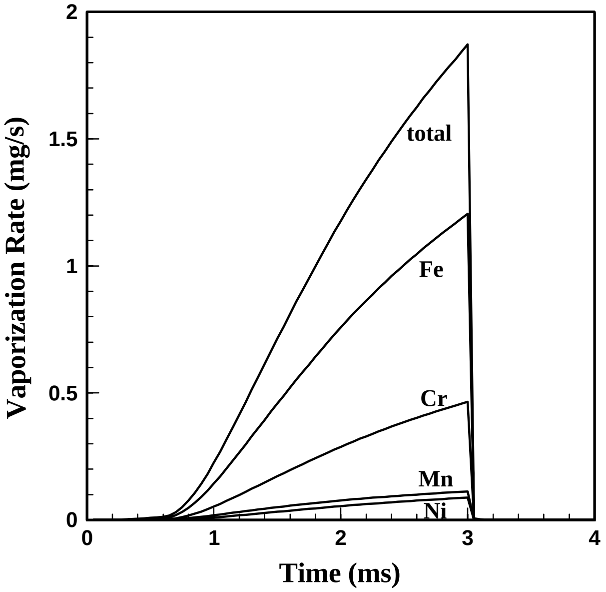

Fig. 6.6: Calculated change of vaporization rates of four alloying elements with time. Laser power: 1067 W, pulse duration: 3.0 ms, and beam radius: 0.26 mm. Data used in calculation are shown in Table 4.2 and Table 5.2.

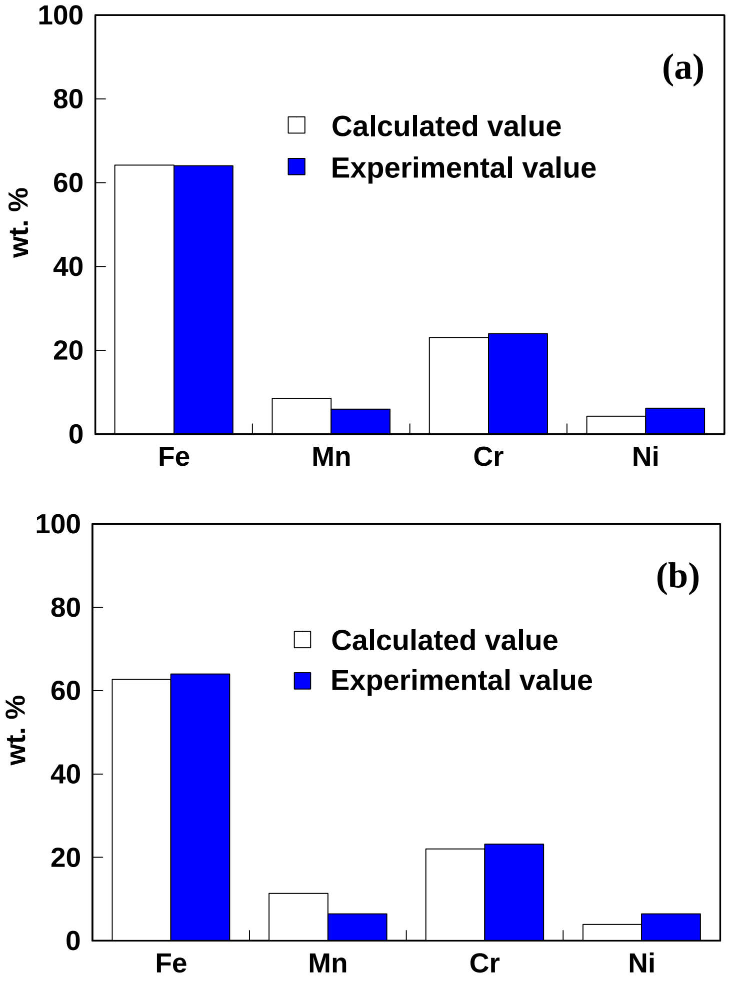

Fig. 6.7: Weight percent of different elements in vapor composition. (a) Laser power: 1063 W, pulse duration: 3.0 ms, and beam radius: 0.28 mm; (b) laser power: 530 W, pulse duration: 4.0 ms, and beam radius: 0.171 mm. Data used in calculation are indicated in Table 4.2 and 5.2.

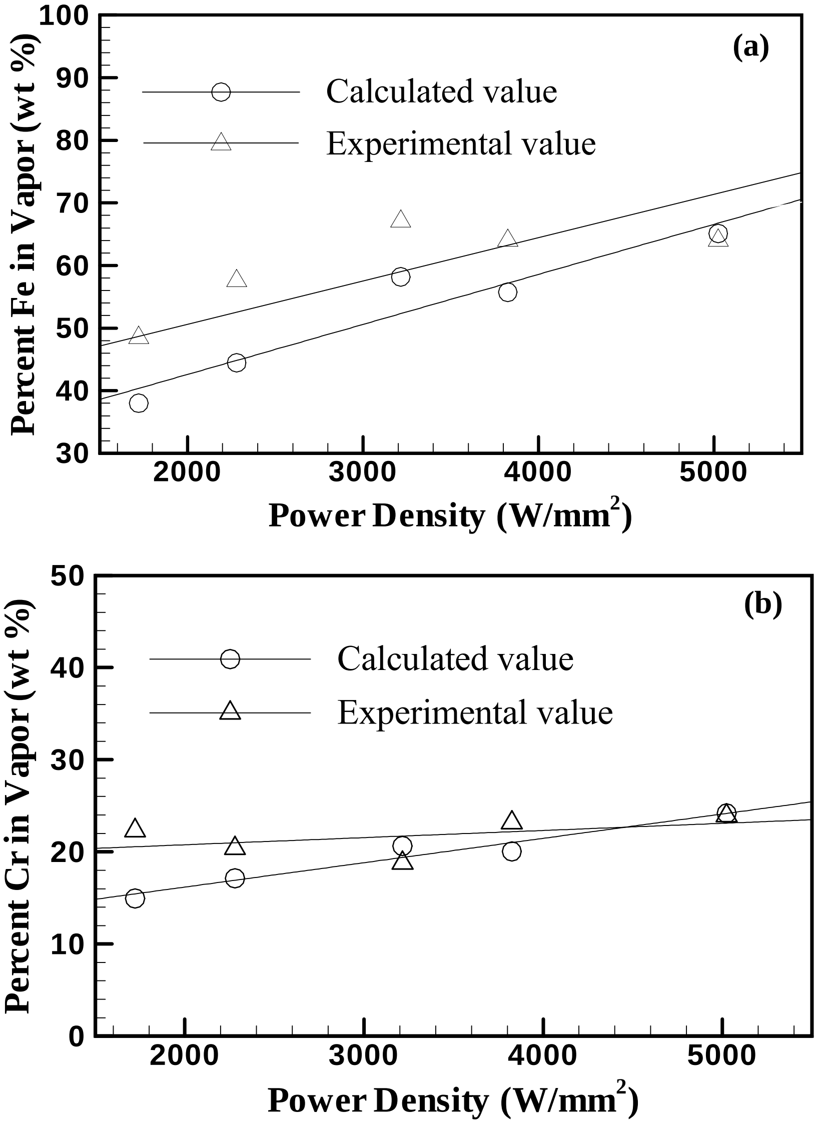

Fig. 6.8: Experimental and computed concentrations of (a) Fe and (b) Cr in the vapor. Welding parameters are shown in Table 6.2. Data used in calculation are indicated in Table 4.2 and 5.2.

Table 6.2: The experimentally determined and calculated vapor composition for different welding conditions. Data used in calculation are indicated in Table 4.2 and Table 5.2.

Spot radius (mm)		Fe (%)		Mn (%)		Cr (%)		Ni (%)	
		Exp	Cal	Exp	Cal	Exp	Cal	Exp	Cal
530 W, 4.0 ms pulse	0.289	48.5	41.7	23.9	40.4	22.3	16.2	5.4	1.7
	0.247	64.4	49.0	8.8	30.4	20.9	18.4	5.9	2.3
	0.227	57.6	52.6	7.4	25.5	20.4	19.3	14.7	2.6
	0.171	64.0	62.7	6.4	11.4	23.2	22.0	6.4	3.9
1063.3 W, 3.0 ms pulse	0.326	67.1	58.6	8.1	17.5	18.8	20.7	6.0	3.3
	0.28	64.0	64.2	5.9	8.5	23.9	23.1	6.2	4.2

‘Exp’ and ‘Cal’ indicate experimentally measured and calculated results, respectively.

6.3.4 Composition Change

As a result of selective vaporization of constituent alloying elements, the concentrations of alloying elements in the weld pool can change significantly during laser spot welding. The composition change, in turn, can lead to significant changes in the microstructure and degradation of mechanical and corrosion properties of welds [4-6].

Fig. 6.9 shows typical concentration profiles of Fe, Cr, Ni and Mn after laser spot welding of 304 stainless steel determined by an electron microprobe. It is observed that the concentrations of the constituent elements in the fusion zone are different from those in the base metal. The concentrations of manganese and chromium in the weld pool are lower than those in the base metal because of vaporization. In contrast, the concentrations of iron and nickel in the fusion zone are slightly higher than those in the base metal, and these results need some discussion. Although the total mass of iron and nickel in the weld pool after welding is slightly lower than that before the welding, the total mass of the weld pool has decreased at a higher proportion because of the loss of manganese, chromium, iron and nickel. As a result, the concentrations of iron and nickel in the fusion zone are higher than those in the base metal because of the loss of manganese and chromium. This behavior, although may appear counterintuitive, is consistent with Equation 3.34.

The computed changes in the concentrations of the constituent alloying elements as a function of time are shown in Fig. 6.10(a). In the first millisecond, the concentration change of alloying elements is small due to low temperature. After that, the vaporization rate increases due to increase in temperature and, as a result, the concentrations of alloying elements significantly increase with time. It can be seen that the concentrations of manganese and chromium decrease while those of iron and nickel increase due to laser spot welding. This behavior is similar to the experimental results presented in Fig. 6.9. Fig. 6.10(b) shows that the changes in the concentration become more pronounced with increase in laser power density resulting from higher temperatures. At the highest laser power density, the absolute values of the concentration changes of iron and chromium are 0.327 wt % and 0.375 wt %, respectively, which are higher than the composition changes of nickel and manganese. This is mainly due to the high concentrations of iron and chromium in the weld metal.

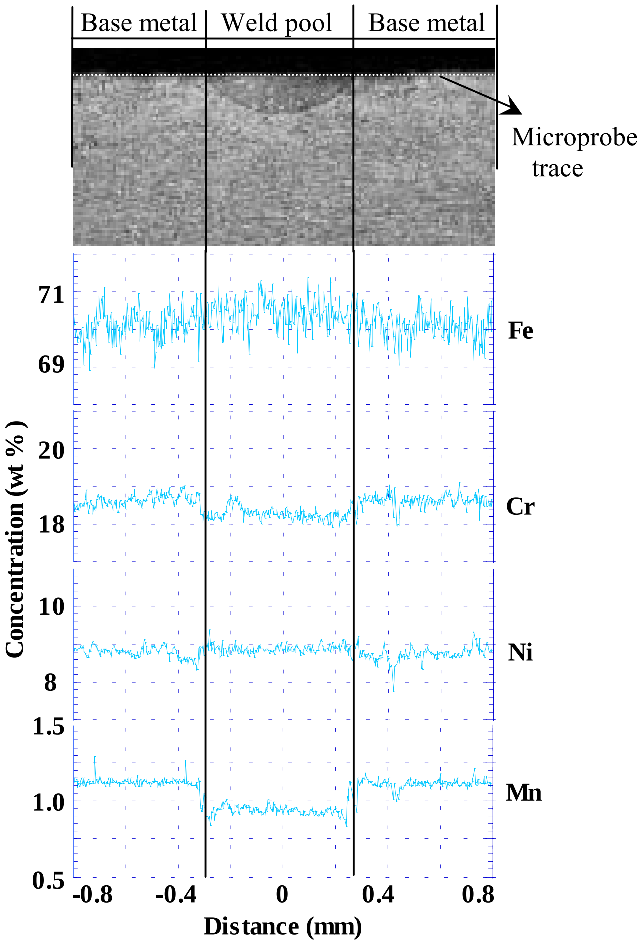

Fig. 6.9: Concentration profiles of various alloying elements traced by electron microprobe after laser spot welding. Laser power: 1067 W, pulse duration: 3.0 ms, and beam radius: 0.325 mm.

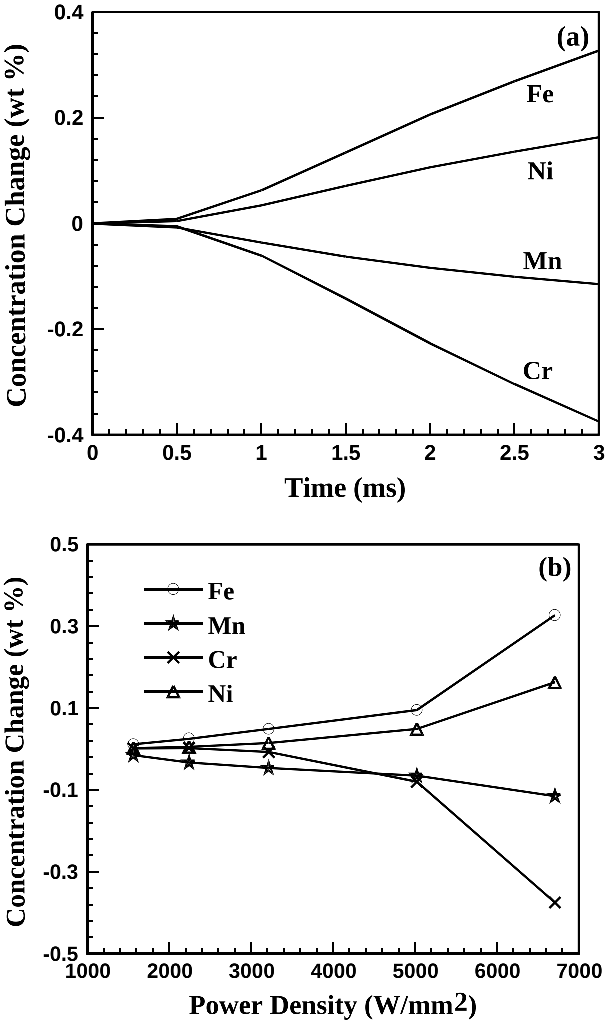

Fig. 6.10: (a) Concentration change of various alloying elements as a function of time. Laser power: 1067 W, pulse duration: 3.0 ms, and beam radius: 0.225 mm. (b) Concentration change of various alloying elements as a function of power density. Laser power: 1067 W, and pulse duration: 3.0 ms. Data used in calculation are indicated in Table 4.2 and Table 5.2.

The comparison between the experimental and computed concentration changes of various alloying elements is shown in Fig. 6.11. The fair agreement between the experimental and computed concentration changes of manganese and chromium as a function of power density can be seen in Fig. 6.12. In experiments, several electron microprobe traces were made for every sample. From Equation 3.34, the final concentration is affected by two factors: volume of weld pool and total weight loss. As laser power density increases, both the volume and total weight loss increase. As a result, the change of concentration with laser power density is not monotonous. Depending on how the rates of volume and total weight loss change with power density, the value of concentration change either increases or decreases. Because the concentration changes of alloying elements influence the mechanical or corrosion properties of alloys, the successful prediction of composition change by the model is helpful to understand how these properties are affected by laser spot welding.

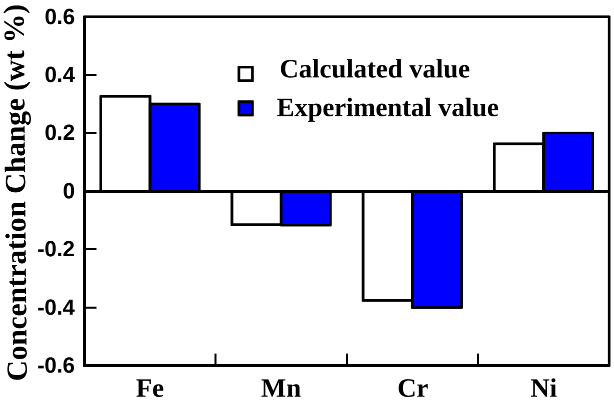

Fig. 6.11: Comparison between calculated and experimentally determined composition change of 304 stainless steel. Laser power: 1067 W, pulse duration: 3.0 ms, and beam radius: 0.225 mm.

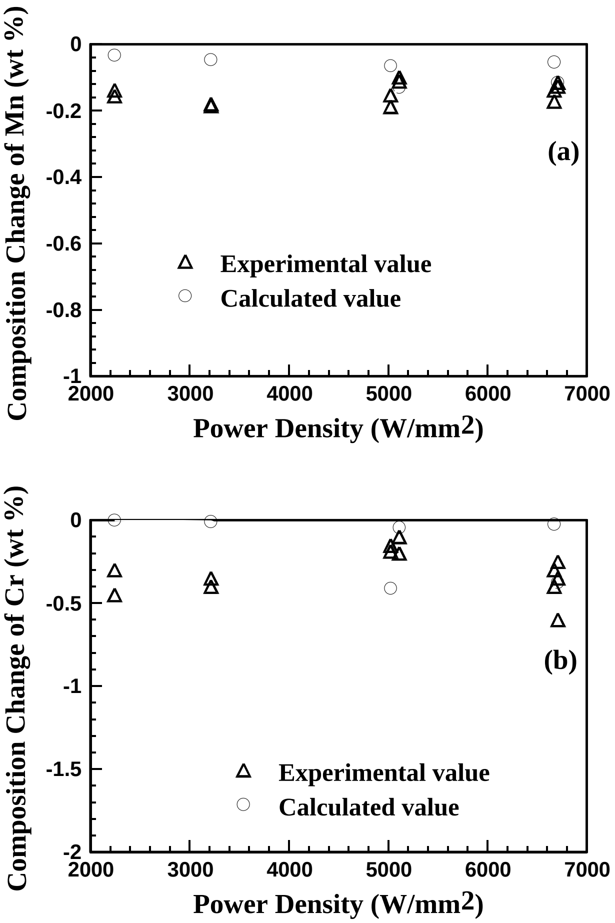

Fig. 6.12: Experimental and calculated concentration changes of (a) manganese and (b) Chromium as a function of power density. Pulse duration: 3.0 ms.

6.3.5 Mass Loss

The calculated mass loss due to evaporation is compared with the experimental results of mass loss at various power densities in Fig. 6.13. Some additional results are also presented in Table 6.3 to include data at lower power (530 W). As the laser power density increases, the temperature at the weld pool surface exceeds the boiling point of the steel. As a result, the total vaporization loss increases significantly due to pressure driven vaporization. However, it can be observed that the experimental weight loss is always higher than the computed mass loss due to vaporization. There are two possible reasons for this discrepancy. First, in a complex modeling effort such as the present research, the accuracy of the modeling results must be carefully considered. In other words, a possibility that all of the mass loss results from vaporization of alloying elements and the model consistently underpredicts the vaporization loss cannot be ruled out. Second, it is conceivable that in addition to vaporization, mass loss also occurs due to ejection of metal droplets. Both these possibilities are examined next.

The computed vaporization rates may be lower than the actual values because of several reasons. First, the computed temperatures on the weld pool surface may be lower than the actual values. Second, the computed weld pool surface area considered in the calculations is lower than the true surface area. Third, the vaporization model used in the calculations may underpredict the vaporization rate for the conditions of the current experiments. First, let us consider the possibility that the computed surface temperatures are lower than the actual temperatures prevailing at the surface. It has been established in several previous studies that during laser welding, most of the vapors originate from the center of the weld pool surface [7,8]. So, for the purpose of this inquiry, the magnitude of the computed peak temperature should be a good parameter to examine. The computed values of peak temperatures for all experiments are presented in Table 6.3. The highest computed peak temperature listed in this table is 3628 K, which is about 600 K higher than the boiling point of the alloy. Although temperatures higher than the boiling point have been reported in the literature [7,8,19,20,24], the reported temperatures are not significantly different from the boiling points for power densities close to about 10^6

watts/cm^2. Therefore, the value of 3628 K, if deemed inaccurate for the sake of argument, can only be higher than the actual value. Furthermore, Table 6.3 shows that even a temperature as high as 3628 K would not result in a vaporization rate necessary to account for all the mass loss due to vaporization. Therefore, the difference between the calculated and the experimental mass loss cannot be attributed to the low computed temperatures. Second, let us examine the role of the weld pool surface area. When the recoil force of the vapors is significant, considerable depression of the weld pool free surface can result, and the true surface area of the weld pool can be significantly higher than the nominal, flat, undeformed surface area. However, the deformation of the surface area can only account for roughly 5 to 20% increase of the surface area for typical surface deformation. The data in Table 6.3 shows that the computed mass loss is significantly lower than the experimentally determined mass loss for most situations and that typical errors in the surface area cannot explain the difference. Third, the accuracy of the evaporation rate calculation must also be examined. The evaporation model has been adapted from the works of Anisimov [25] and Knight [26]. The same model has been extensively applied to calculate the laser induced vaporization rates of alloying elements [7,8,24]. In each case, the computed vaporization rate has been comparable to the corresponding experimental data. So, the difference between the computed vaporization loss and the experimental mass loss cannot be attributed to inaccuracies resulting from the evaporation model. It is also worth noting that the experimentally measured mass loss indicated in Table 6.3, if totally attributed to vaporization, demands unrealistically high values of vaporization rate. For example, let us consider the experiment utilizing a 0.159 mm radius laser beam having 530 W power applied for 4 ms. The total mass loss was found to be 15.6 micrograms. If the entire mass loss is attributed to vaporization, the vaporization rate can be readily estimated. If we assume that roughly 1 ms was needed for the initial heating, the average vaporization rate is calculated as 5.2 mg/s. For the welding of stainless steel with a comparable power density beam, an overall vaporization rate of about 1 mg/s has been reported [27]. Thus, the experimental value of mass loss is far too high to be explained by vaporization alone.

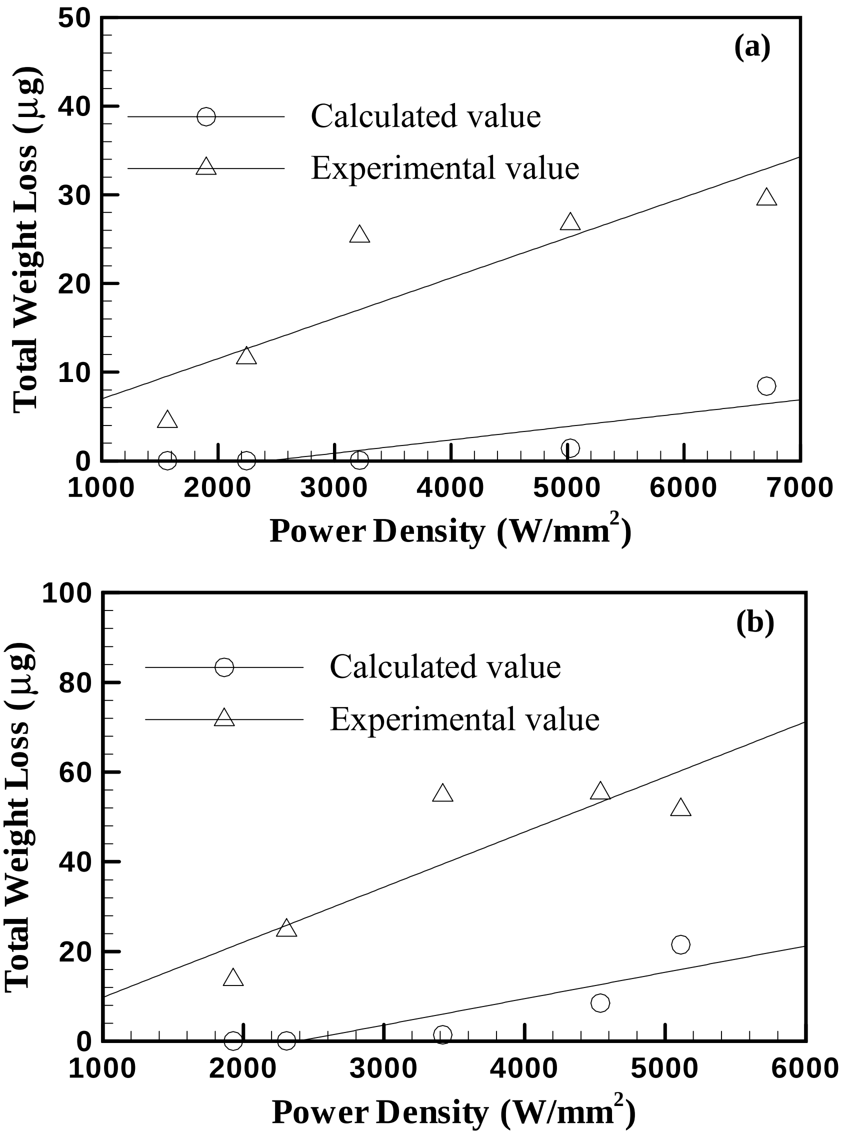

Fig. 6.13: The calculated vaporization loss is compared with measured mass loss for different power densities: (a) laser power: 1067 W, pulse duration: 3.0 ms; (b) laser power: 1967 W, pulse duration: 3.0 ms. Data used in calculation are indicated in Table 4.2 and Table 5.2.

Table 6.3: The calculated mass loss due to evaporation is compared with the experimentally determined mass loss for different welding conditions. Data used in calculation are indicated in Table 4.2 and Table 5.2.

Spot radius (mm)		Calculated peak temperature (K)	Weight loss (μg)	
			Calculated	Experimental
1967 W, 3.0 ms pulse	0.350	3628	21.52	51.6
	0.379	3448	8.50	55.3
	0.428	3205	1.42	54.8
	0.521	2814	0.08	24.7
	0.570	2674	0.04	13.7
1067 W, 3.0 ms pulse	0.225	3561	8.43	29.5
	0.260	3270	1.42	26.7
	0.325	2879	0.07	25.3
	0.389	2606	0.02	11.6
	0.466	2365	4.7×10^{-3}	4.4
530 W, 4.0 ms pulse	0.159	3176	0.46	15.6
	0.210	2761	0.03	3.6
	0.272	2451	6.7×10^{-3}	1.6
	0.313	2308	3.0×10^{-3}	0.6
	0.433	2032	0.5×10^{-3}	0.33

A possible reason for the discrepancy between the experimental weight loss and the calculated vaporization loss is that only a portion of the mass loss occurs due to evaporation, and the remainder of the loss must be attributed to some other mechanism. Therefore, the possibility of ejection of the tiny metal droplets from the weld pool owing to the recoil force exerted by the metal vapors has been, subsequently, examined both experimentally and theoretically.

6.3.6 Liquid Metal Expulsion

Fig. 6.14 shows the presence of condensed metal vapor and ejected tiny droplets on the interior wall of the quartz placed co-axial to the laser beam and right above the 304 stainless steel sample tube for several cases. The Energy Dispersive X-Ray Spectroscopy (EDS) profile for the ejected metal droplets in Fig. 6.15 indicates the presence of Fe, Mn, Cr, Ni, Si and O elements. Of these, the elements Si and O detected by EDS originated from the quartz tube. The remaining elements detected are the main elements in stainless steel. Therefore, the droplets shown in Fig. 6.14 originated from the molten 304 stainless steel weld pool, and then deposited on the interior wall of the quartz tube during laser spot welding.

Fig. 6.14 shows that under some welding conditions, only deposition of metal vapor was observed on the interior wall of the quartz tube, whereas both vapor condensate and ejected metal droplets were observed under other conditions. The size range of the ejected droplets has been determined by optical microscopy for different welding conditions. Fig. 6.16 shows the ejected droplet size as a function of power density. It can be seen that the size of the ejected droplets ranges from tens of micrometers to several hundred micrometers. Increase of power density results in larger particle size and particle size range. With the increase in power density, both the weld pool temperature as well as the weld pool size increase. The higher recoil pressures as well as the availability of more liquid metal are consistent with more liquid metal expulsion and larger droplets. The calculations to be presented subsequently in this chapter will show that after the initiation of the pulse, the weld pool is heated for certain duration before the liquid metal expulsion starts. Subsequently, the metal expulsion takes place over a span of time until the end of the pulse. The system does not reach steady state during the metal expulsion. As a result, the ejected particles show a range of droplet size as observed in Fig. 6.16.

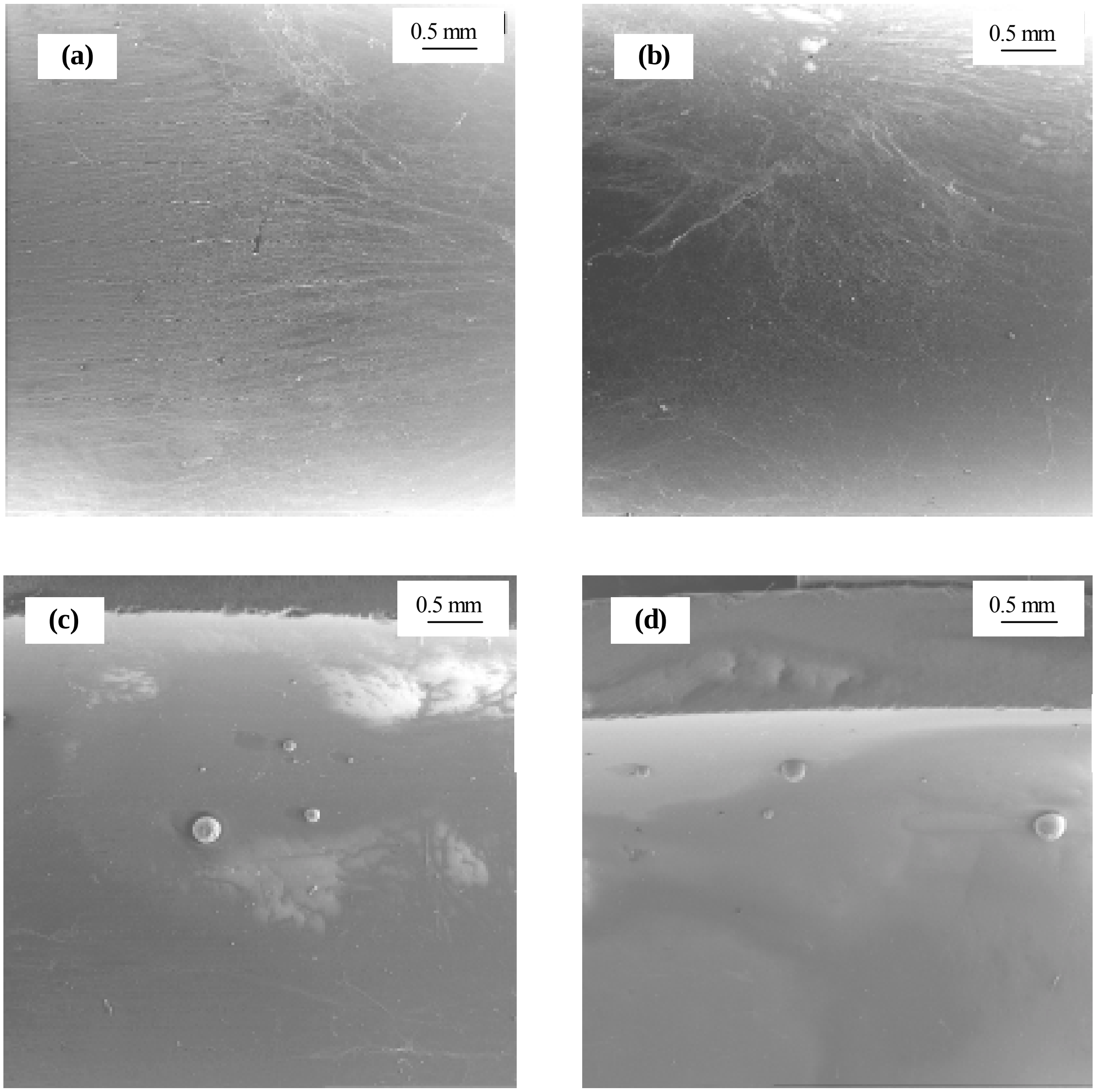
(a)
0.5 mm
(b)
0.5 mm
(c)
0.5 mm
(d)
0.5 mm

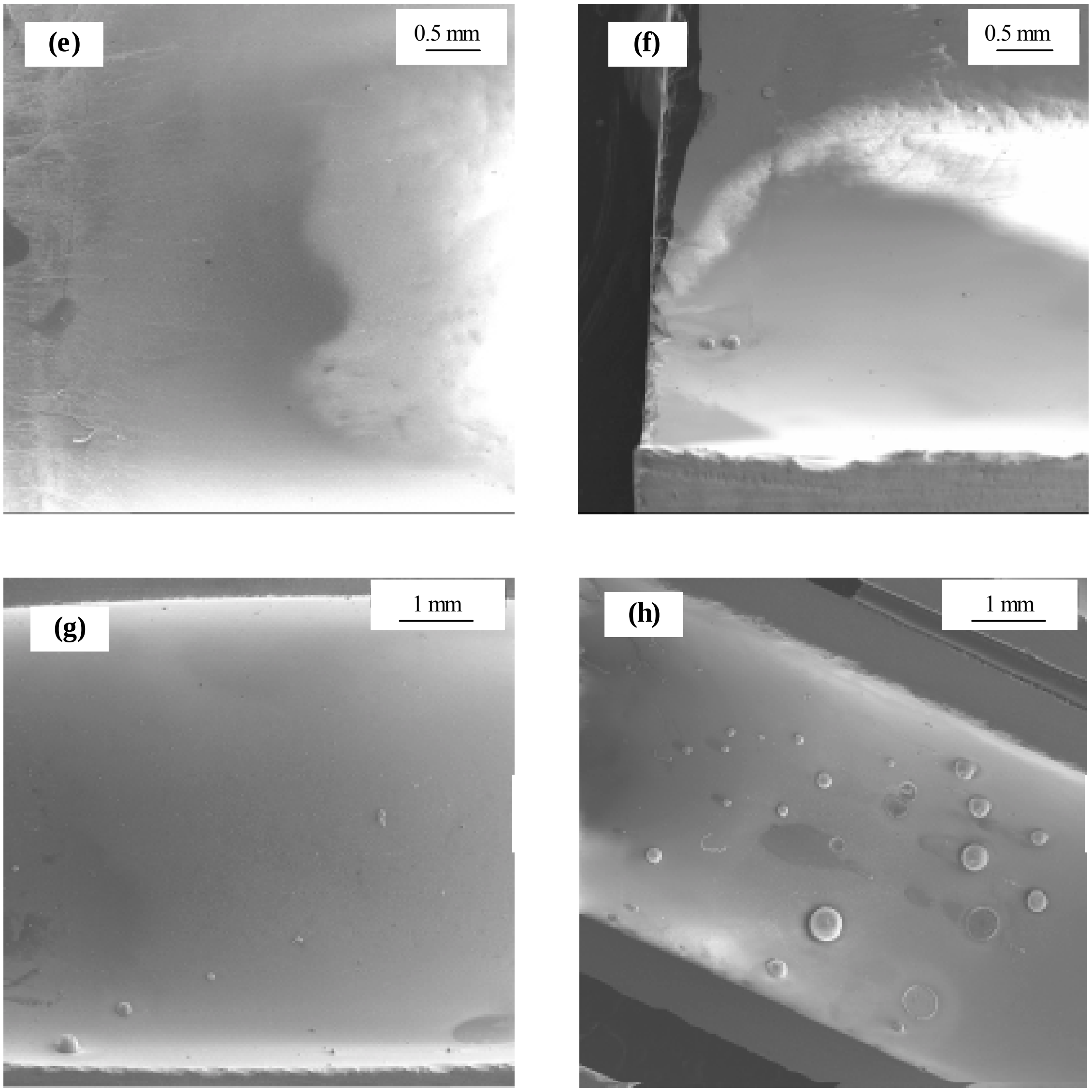

Fig. 6.14: Vaporized elements and tiny droplets ejected from the weld pool of 304 stainless steel, were captured on the inner surface of a both-end-open quartz tube placed co-axial with the laser beam during spot welding with pulse duration of 3 ms, laser power of 1067 W and spot diameter of (a) 0.625 mm, (b) 0.51 mm, (c) 0.405 mm and (d) 0.39 mm; and laser power of 1967 W and spot diameter of (e) 0.835 mm, (f) 0.651 mm, (g) 0.533 mm and (h) 0.501 mm. The results were obtained from Sandia National Laboratories.

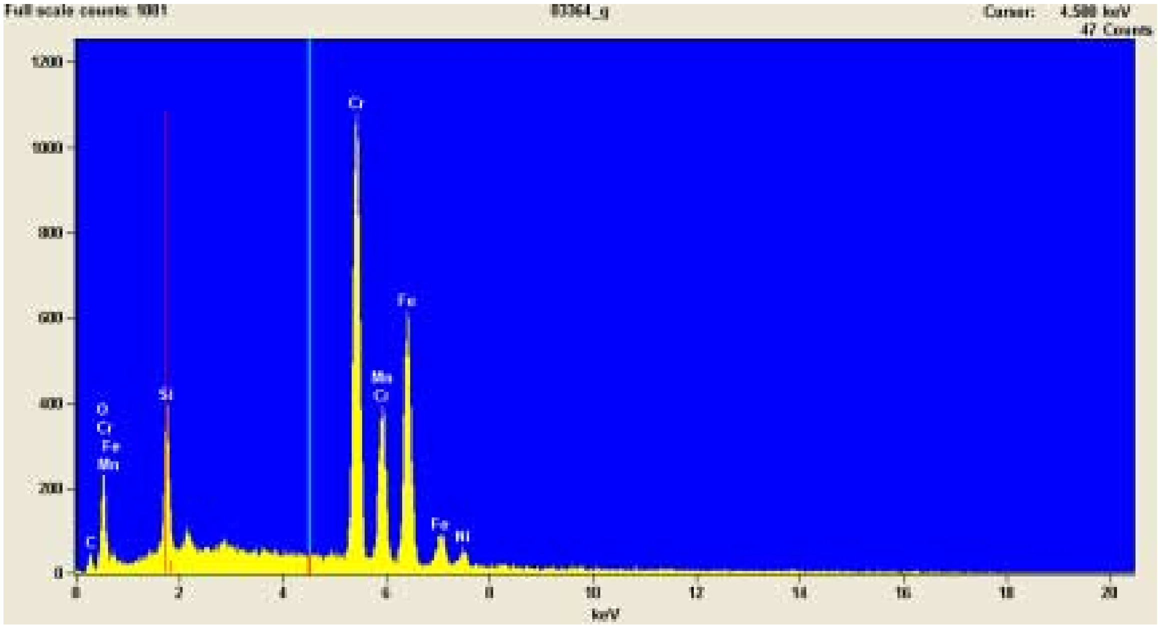

Fig. **6.15**: EDS profile for the ejected metal droplets, which were deposited on the interior wall of quartz tube. Laser power: 1967 W, pulse duration: 3 ms and spot diameter: 0.501 mm. The results were obtained from Sandia National Laboratories.

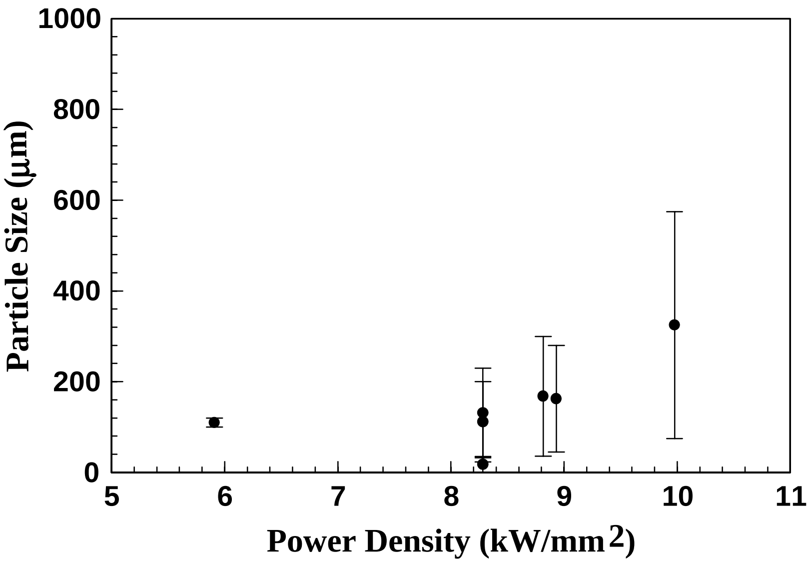

Fig. **6.16**: Effect of power density on the size of ejected metal droplets. Welding parameters are shown in Fig. **6.14**.

The experimental results indicate that the liquid metal expulsion took place at higher laser power densities when the weld metal was heated to higher temperatures. Calculated temperature distributions along the x-direction on the weld pool surface at different times for the samples A, B, C and D are shown in Fig. 6.17. The origin represents the location of the laser beam. The two lines in the figure indicate solidus (1697 K) and liquidus temperatures (1727 K). The thin region between these two lines is the two-phase solid-liquid mushy zone. It can be seen that the temperatures reach very high values near the laser beam axis and decrease with distance. It can also be observed that there are inflexion points close to the mushy zone, which result from the differences in the enthalpies of the solid and liquid metals. Also, with the decrease of beam radius, the temperatures increase due to higher laser power density. The calculation of temperature at different locations on the weld pool surface and at different times provides a theoretical basis in determining whether the liquid metal expulsion can take place.

High temperatures result in high equilibrium vapor pressures, which tend to push the liquid metal out of the weld pool. On the other hand, the surface tension force of the liquid metal holds the liquid metal in place, which tends to prevent liquid metal expulsion. When the temperature on the surface of the weld pool exceeds a critical value, the recoil force overcomes the surface tension force and liquid metal is expelled from the liquid pool. The vapor recoil force F_r and the surface tension force at the periphery F_s can be expressed by:

$$F_r = 2\pi \int_0^{r_B} r\Delta P(r)dr \qquad (6.5)$$

$$F_s = 2\pi r_0 \sigma \qquad (6.6)$$

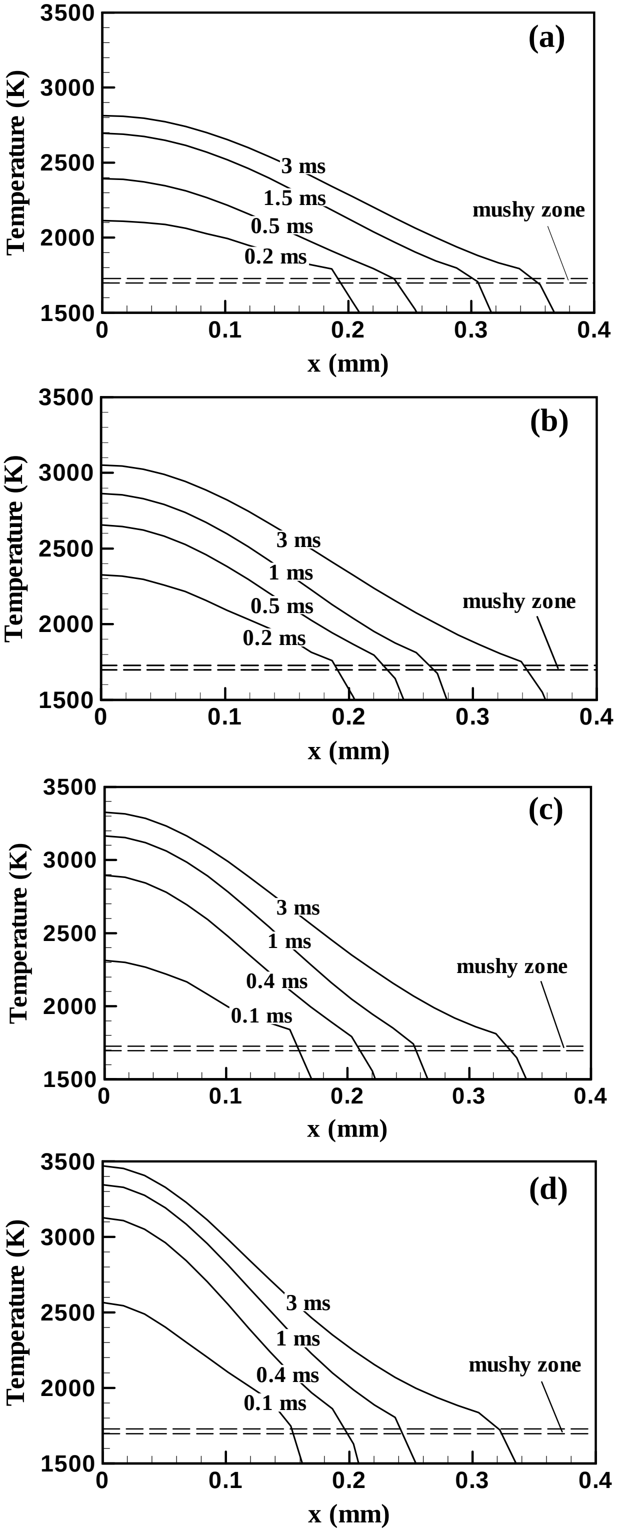

Fig. 6.17: Distribution of temperatures on the weld pool surface at different times. Laser power: 1067 W, pulse duration: 3 ms and spot diameter: (a) 0.625 mm, (b) 0.51 mm, (c) 0.405 mm and (d) 0.39 mm. Data used in calculation are shown in Table 4.2.

where r_B is the radial distance at which the surface temperature reaches the boiling point, ΔP is the difference between the local equilibrium vapor pressure and the atmospheric pressure and is the function of radial distance from the beam axis, r_0 is the radial distance at which the temperature is equal to the melting point, and σ is the surface tension coefficient at the melting point, taken as 1.872 N/m for stainless steel [28]. Fig. 6.18 shows the computed values of the surface tension force and vapor recoil force as a function of time during laser spot welding of 304 stainless steel. For example, in Fig. 6.18(c), it is observed that the surface tension force is higher than the recoil force at the start of the pulse. As the temperature increases with time, both the surface tension force and the recoil force increases. However, the recoil force increases faster than the surface tension force. At about 2.6 ms after the start of the pulse, the two forces are roughly equal. Further heating results in higher recoil force than surface tension force. When the recoil force exceeds the surface tension force, expulsion of liquid metal is anticipated. For Sample A in Fig. 6.18(a), the peak temperature on the weld pool surface is 2814 K, which is lower than the boiling point of 304 stainless steel, about 2980 K, which means that the vapor pressure is lower than one atmosphere and no expulsion of liquid metal occurs. For Sample B in Fig. 6.18(b), although the peak temperature, 3052 K, exceeds the boiling point of 304 stainless steel, the recoil force is weaker than the surface tension force of the liquid metal at the periphery of the weld pool for the whole pulse duration. As a result, no liquid metal expulsion takes place. In Fig. 6.18, for Samples C, D, F, G and H, the recoil force begins to exceed the surface tension force at some time during the welding process, which means that it is possible for liquid metal droplets to be ejected from the weld pool. This conclusion agrees well with experimental observations indicated in Table 6.4**,** which illustrates whether the liquid metal expulsion takes place.

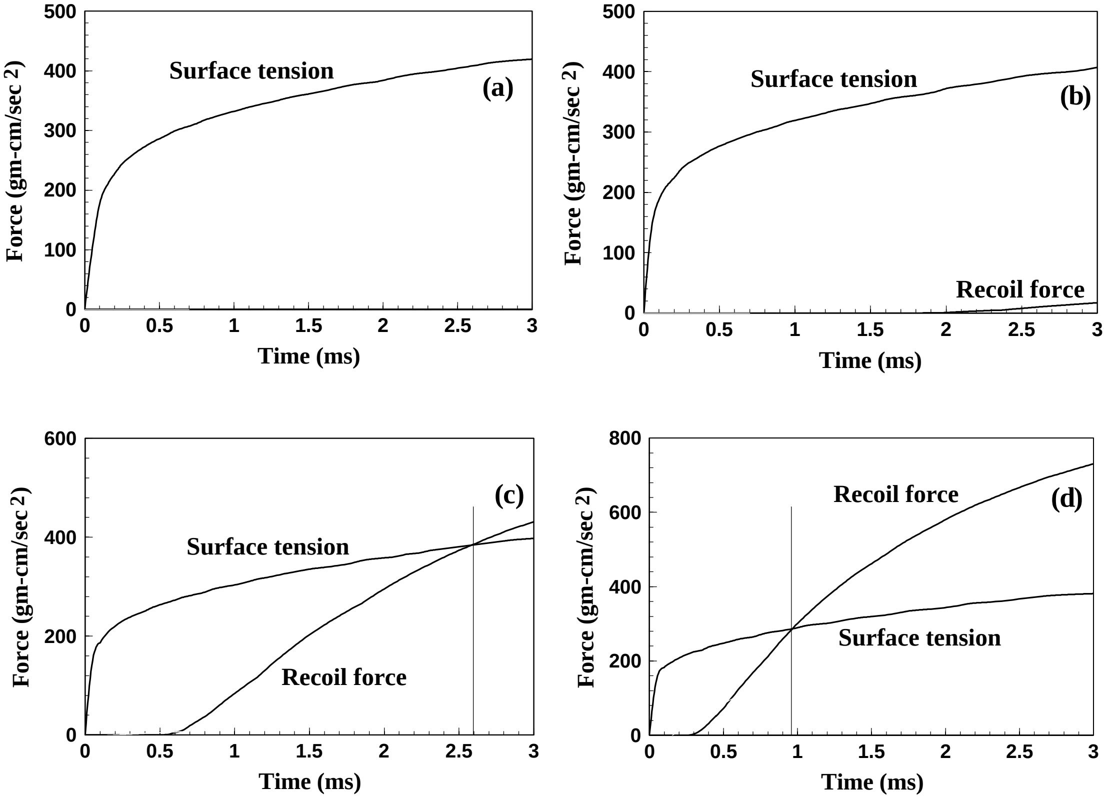
Force (gm-cm/sec 2)
Time (ms)
Surface tension
(a)
Surface tension
(b)
Recoil force
(c)
Surface tension
Recoil force
(d)
Recoil force
Surface tension
0
0.5
1
1.5
2
2.5
3
0
100
200
300
400
500
600
800

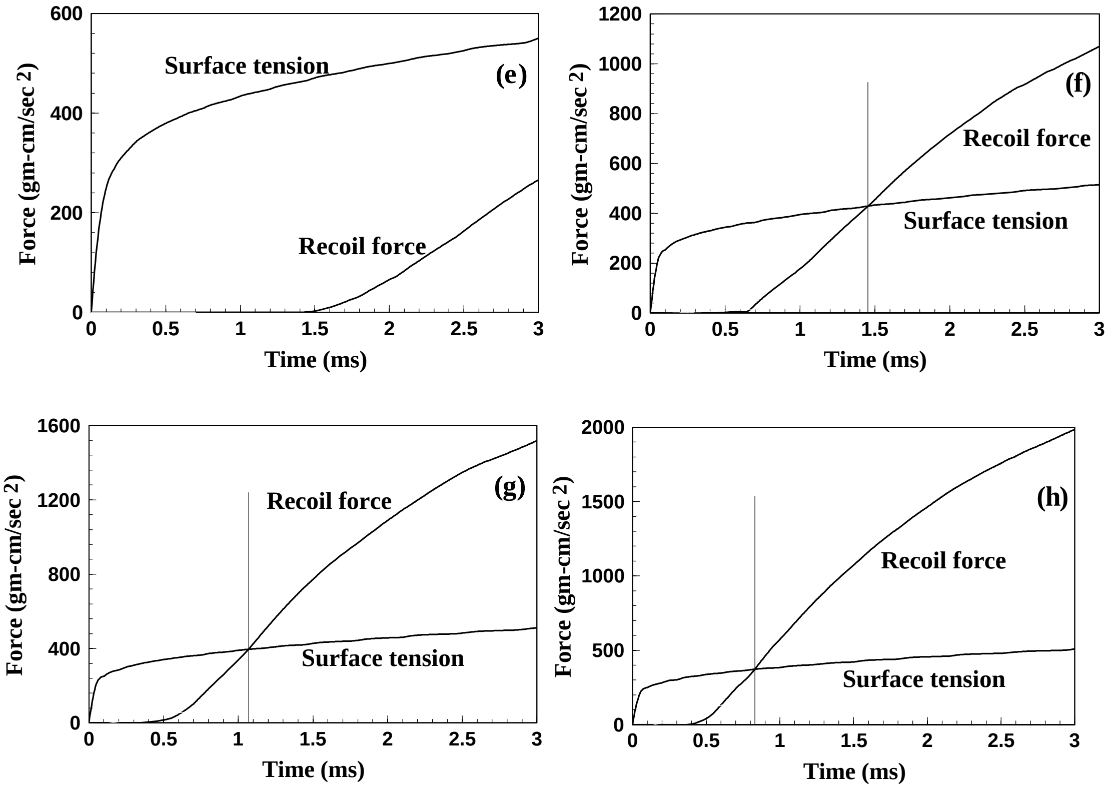

Fig. 6.18: Recoil force and surface tension force at the periphery of the liquid pool as a function of time under the condition of pulse duration of 3 ms, laser power of 1067 W and spot diameter of (a) 0.625 mm, (b) 0.51 mm, (c) 0.405 mm and (d) 0.39 mm; and laser power of 1967 W and spot diameter of (e) 0.835 mm, (f) 0.651 mm, (g) 0.533 mm and (h) 0.501 mm.

Table 6.4: Vapor deposit and tiny droplet expulsion observed in experiments. Pulse duration: 3 ms.

Sample no.	Laser power (W)	Spot diameter (mm)	Power density (W/mm^2)	Observation	Size for ejected liquid droplets (μm)
A	1067	0.625	3478	Vapor deposit only	—
B	1067	0.51	5223	Vapor deposit only	—
C	1067	0.405	8283	Vapor deposit and tiny droplet expulsion	1-35 23-200 32-230
D	1067	0.39	8932	Vapor deposit and tiny droplet expulsion	45-280
E	1967	0.835	3592	Vapor deposit only	—
F	1967	0.651	5910	Vapor deposit and tiny droplet expulsion	100-120
G	1967	0.533	8816	Vapor deposit and tiny droplet expulsion	36-300
H	1967	0.501	9978	Vapor deposit and tiny droplet expulsion	75-575

The experimental combinations of laser power and spot diameter that lead to liquid metal expulsion for pulse durations of 3.0 ms and 4.0 ms, respectively, are shown by the dotted line in Fig. 6.19. The points on the same dotted curve have the same laser power density, defined by laser power per unit area. It is observed that the liquid expulsion occurs above a critical laser power. For the same laser power, when the spot diameter is large, liquid metal expulsion is not observed. With the decrease of spot diameter, the intermittent expulsion occurs due to the increase of laser power density. When the spot diameter continues to decrease, the laser power density increases and eventually significant expulsion takes place at high laser power density. Fig. 6.19 shows that pulse duration also affects liquid metal expulsion. For a 3.0 ms pulse duration, the critical laser power density for liquid metal expulsion is about 8.0 kW/mm^2. However, when the pulse duration is increased to 4.0 ms, the critical laser power density decreases to about 7.0 kW/mm^2. The recoil and surface tension forces were compared to predict the critical beam diameter under different laser powers, as shown by the solid lines in Fig. 6.19. The computed spot diameter and laser power combination necessary to initiate liquid metal expulsion agreed well with experiments, indicating the accuracy of the mechanism of liquid metal expulsion.

Fig. 6.20 shows the extent of liquid metal expulsion under different laser power densities and pulse durations. At a given pulse duration, higher laser power density increases the tendency of intermittent or heavy liquid metal expulsion. At 7 kW/mm^2, no vapor deposits were noticeable on the inner surface of the quartz tube for a pulse duration of 2 ms. When the pulse duration was increased to 3 ms, a coating of metal vapor condensate was found on the inner wall of the quartz tube. When the pulse duration was further increased beyond 4 ms, intermittent or heavy expulsion of metal drops was observed. Liquid metal expulsion can take place at lower critical power density when longer duration pulses are used, which has also been predicted from calculated results, as shown by the solid line in Fig. 6.20. The longer pulse duration allows more interaction time between the laser beam and the materials and leads to high weld pool temperatures and high recoil pressures. Therefore, liquid metal expulsion can take place at a lower laser power density when longer pulse duration is used. Laser power density and pulse duration are the two most important parameters for the liquid metal expulsion. The results shown in Figs. 6.19 and 6.20 provide guidance in controlling the occurrence of liquid metal ejection in laser spot welding by adjusting these two parameters.

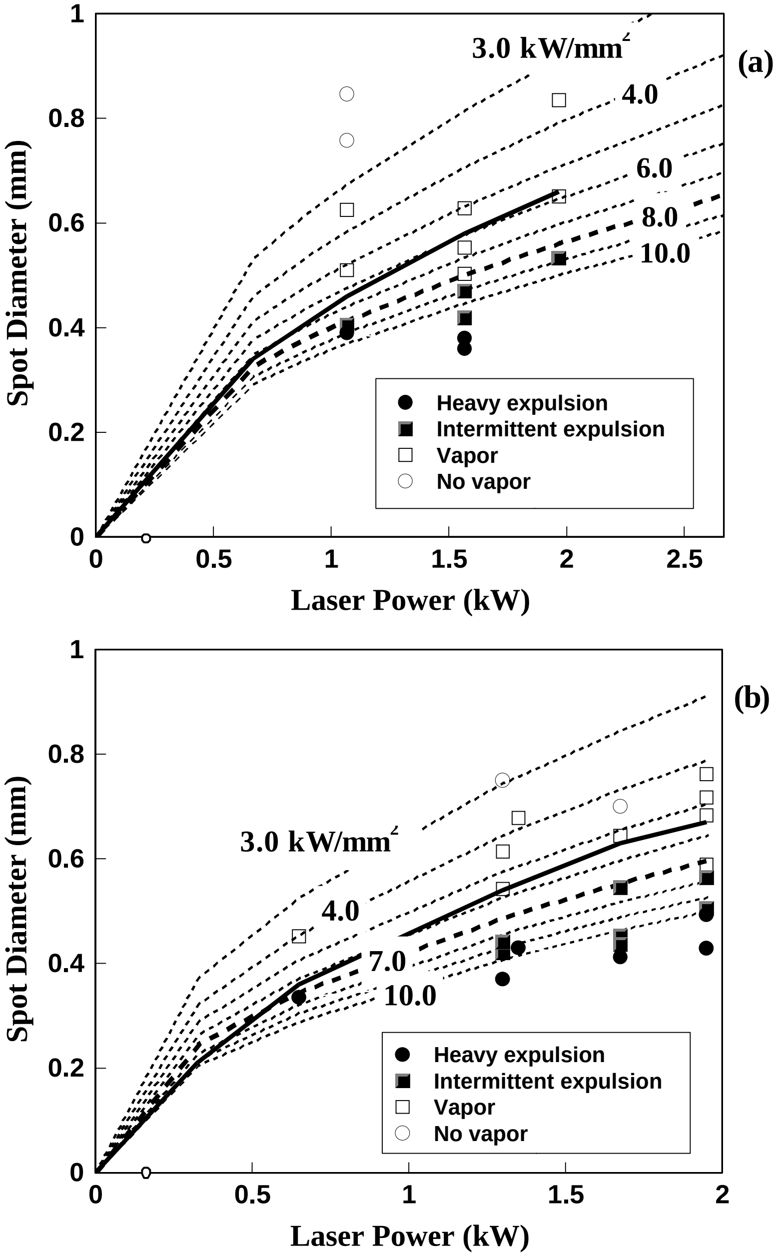

Fig. 6.19: Liquid metal expulsion analysis data under different laser power densities for laser spot welding of 304 stainless steel. (a) 3.0 ms pulse duration, and (b) 4.0 ms pulse duration.

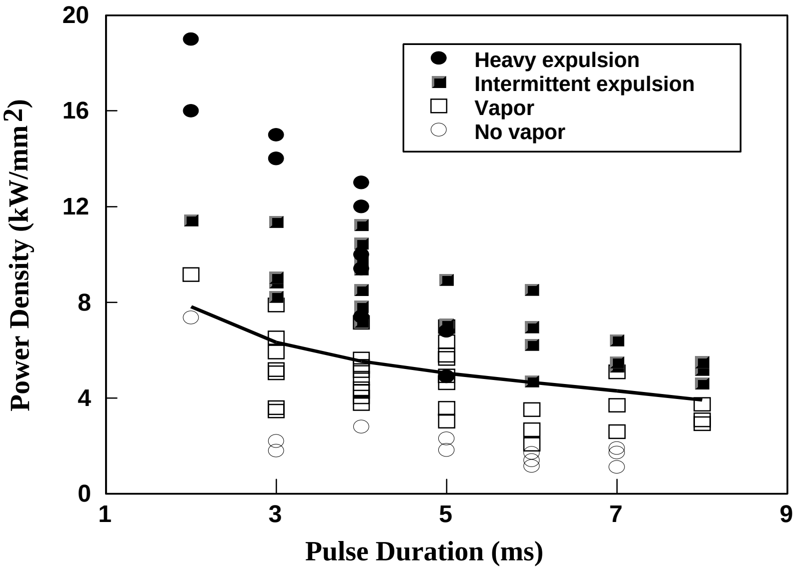

Fig. 6.20: Analysis of liquid metal expulsion under different laser power densities and pulse durations for laser spot welding of 304 stainless steel.

Fig. 6.21 shows the computed free surface profiles at different times. The sample surface is taken as a reference surface. Near the middle of the weld pool, the liquid metal is depressed due to high recoil pressure. The liquid metal displaced from the middle is transported near the boundary of the weld pool, where a hump is formed to satisfy the conservation of total volume. With time, the recoil pressure on the weld pool increases due to higher surface temperatures. As a result, the extent of surface deformation increases with time. The dimensionless number indicating the ratio of maximum depression, l, to the weld pool depth, d, is used to indicate the extent of surface deformation. Fig. 6.22 shows that the ratio increases with time. The variation of l/d with laser power density is shown in Fig. 6.23. It can be seen that the ratio increases as the laser power density increases. When the laser power density is low, the temperature is lower than the boiling point, the vapor pressure is lower than atmospheric pressure and the weld pool surface is flat. As the laser power density increases, the temperature on the weld pool surface can become higher than the boiling point, and significant deformation of the free surface occurs. Fig. 6.19(b) shows that the critical laser power density is 7 kW/mm^2 for a pulse duration of 4 ms. This experimental result is in agreement with calculations of vapor recoil pressure and surface tension force. The corresponding value of maximum depression of liquid metal is about 14% of weld pool depth, as seen in Fig. 6.23. The results shown in Fig. 6.23 indicate that apart from the calculations of the recoil and surface tension forces, the depression of the free surface may also serve as an indicator of liquid metal expulsion.

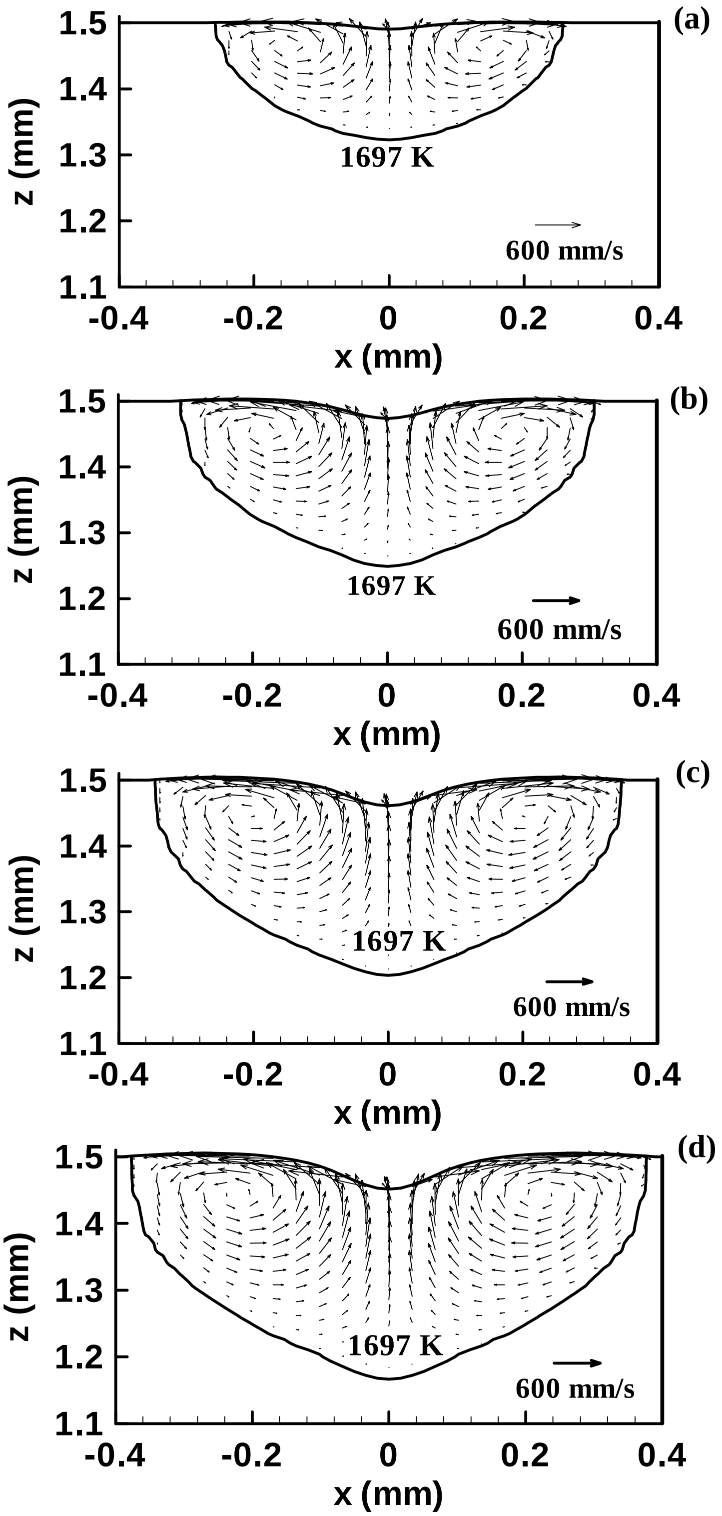

Fig. 6.21: Temperature distribution with free surface at times of (a) 1 ms, (b) 2 ms, (c) 3 ms and (d) 4 ms. Laser power: 1300 W, pulse duration: 4 ms and spot diameter: 0.42 mm. Data used in calculation are shown in Table 4.2.

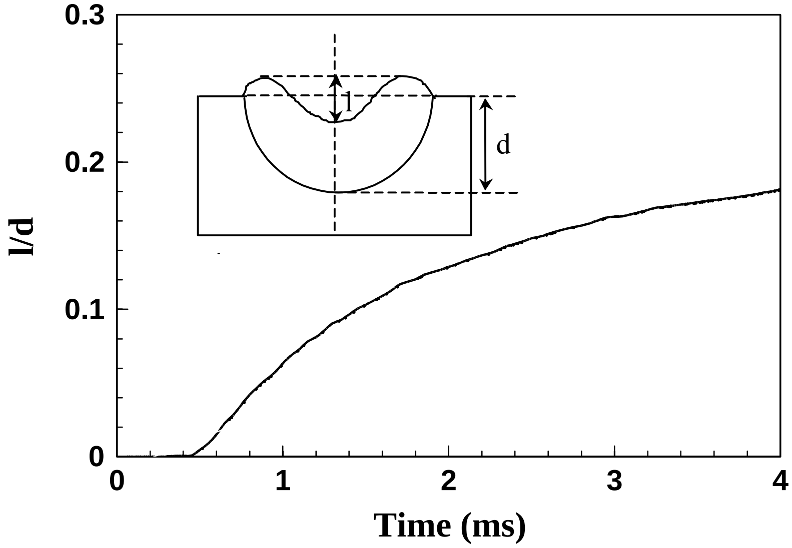

Fig. 6.22: Computed l/d as a function of time. Laser power: 1067 W, pulse duration: 3 ms and spot diameter: 0.405 mm. Data used in calculation are shown in Table 4.2.

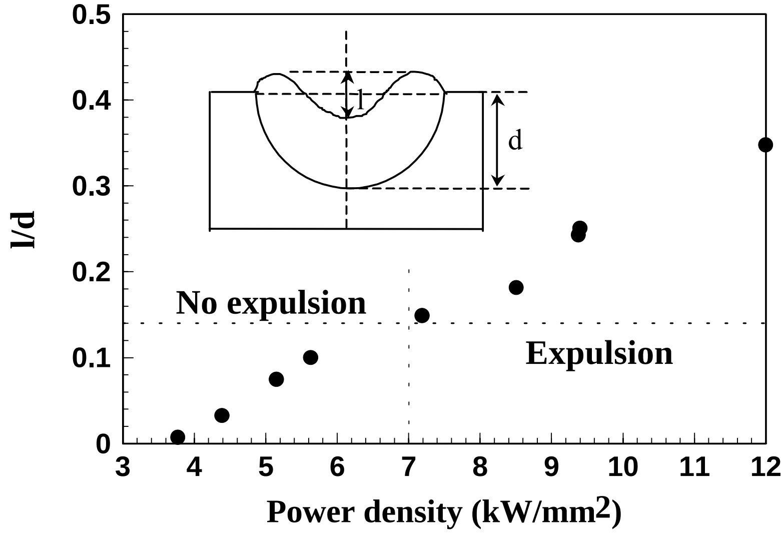

Fig. 6.23: Variation of l/d with laser power density. Pulse duration: 4 ms. Data used in calculation are shown in Table 4.2.

6.4 Summary and Conclusions

Vaporization of alloying elements and liquid metal expulsion from the weld pool during laser spot welding of stainless steel has been investigated experimentally and theoretically. The experiments involved measurements of weight loss, electron microprobe analysis of weld pool composition change resulting from welding, and analysis of the chemical composition of the vapor by condensing a portion of it on the inner surface of a both-end-open quartz tube. In theoretical work, a comprehensive model to calculate temperature, vaporization rates of alloying elements and weld metal composition change during laser spot welding of 304 stainless steel, taking into account both vaporization and condensation, was developed.

During laser spot welding, peak temperature and volume of the weld pool increased with time and laser power density. At very high power densities, the computed temperatures on the weld pool surface were found to be higher than the boiling point of 304 stainless steel. As a result, vaporization of alloying elements resulted from both pressure and concentration gradients. The calculations showed that the vaporization was concentrated in a small region under the laser beam where the temperature was very high. The computed vapor loss was found to be lower than the measured mass loss because of the ejection of the tiny metal droplets owing to the recoil force exerted by the metal vapors. After laser spot welding, the concentration of manganese and chromium decreased, while the concentration of iron and nickel increased owing to welding. The composition change predicted by the model was in fair agreement with the corresponding experimental results for spot welds of a few milliseconds duration and a few hundred micrometers depth.

If the temperature in the weld pool is very high, liquid metal droplets are expelled from the weld pool. The liquid metal expulsion can be predicted by balancing the vapor recoil force with the surface tension force at the periphery of the liquid pool under various welding conditions. The laser power density and pulse duration are the two most important parameters for liquid metal expulsion during laser spot welding. Higher laser power density and longer pulse duration increases the tendency of occurrence of liquid metal expulsion. The size of the ejected droplets ranges from tens of micrometers to several hundreds of micrometers. Increase of power density results in larger droplets and greater size range of particles. The depression of the weld center under the recoil pressure could be used as an indicator of liquid metal expulsion during welding.

6.5 References

1. A. Block-Bolten and T. W. Eagar, *Metall. Trans. B*, **15B**, 461 (1984).
2. R. G. J. Dunn, C. D. Allemand and T. W. Eagar, *Metall. Trans.*, **17A**, 1851 (1986).
3. G. J. Dunn and T. W. Eagar, *Metall. Trans.*, **17A**, 1865 (1986).
4. A. Blake and J. Mazumder, *J. Eng. Ind.,* **107**, 275 (1985).
5. D. W. Moon and E. A. Metzbower, *Weld. J.,* **62**, 53s (1983).
6. M. J. Cieslak and P. W. Fuerschbach, *Metall. Trans. B*, **19B**, 319 (1988).
7. H. Zhao and T. DebRoy, *Metall. Trans. B*, **32B**, 163 (2001).
8. K. Mundra and T. DebRoy, *Metall. Trans. B*, **24B**, 145 (1993).
9. P. A. A. Khan and T. DebRoy, *Metall. Trans. B*, **15B**, 641 (1984).
10. M. M. Collur, A. Paul and T. DebRoy, *Metall. Trans. B*, **18B**, 733 (1987).
11. S. Basu and T. DebRoy, *J. Appl. Phys.*, **72**, 3317 (1992).
12. K. T. Voisey, C. F. Cheng and T. W. Clyne, in *Laser-solid Interactions for Materials Processing*, edited by D. Kumar (San Francisco: Materials Research Society, 2001) pJ5.6.1.
13. K. T. Voisey, S. S. Kudesia, W. S. O. Rodden, D. P. Hand, J. D. C. Jones and T. W. Clyne, *Mater. Sci. Eng. A*, **356**, 414 (2003).
14. Y. F. Lu, Y. W. Zheng and W. D. Song, *J. Appl. Phys.*, **87**, 549 (2000).

15. B. S. Yilbas, *J. Laser Appl.*, **7**, 147 (1995).

16. M. K. Chun and K. Rose, *J. Appl. Phys.*, **11**, 614 (1970).

17. W. S. O. Rodden, P. Solana, S. S. Kudesia, D. P. Hand, P. Kapadia, J. Kowden and J. D. C. Jones, in *International Congress on Applications of Lasers and Electro-optics* (San Diego: Laser Institute of American, 1999).

18. M. von Allmen, *J. Appl. Phys.,* **47**, 5460 (1976).

19. C. L. Chan and J. Mazumdar, *J. Appl. Phys.*, **62**, 4579 (1987).

20. M. von Allmen, *Laser Beam Interaction with Materials* (London: Springer-Verlag, 1987).

21. T. Iida and R. I. L. Guthrie, *The Physical Properties of Liquid Metals* (Oxford: Clarendon Press, 1988) p8.

22. S. Dushman, *Scientific Foundations of Vacuum Technique* (New York: Wiley, 1962).

23. P. Sahoo, M. M. Collur and T. DebRoy, *Metall. Trans. B*, **19B**, 967 (1988).

24. T. DebRoy, S. Basu and K. Mundra, *J. Appl. Phys.*, **70**, 1313 (1991).

25. S. I. Anisimov and A. Kh Rakhmatulina, *Soviet Physics – JETP*, **37**, 441 (1973).

26. C. J. Knight, *AIAA J.***,** **17**, 519 (1979).

27. P. A. A. Khan, T. DebRoy and S. A. David, *Weld. J.*, **67**, 1s (1988).

28. T. Iida and R. I. L. Guthrie, *The Physical Properties of Liquid Metals* (Oxford: Clarendon Press, 1988).

Chapter 7

CONCLUDING REMARKS

7.1 Summery and Conclusions

The present thesis have addressed several important experimental and theoretical issues involving Nd:YAG laser welding of 304 stainless steel with hundreds of micrometers in laser beam diameter, such as heat transfer and fluid flow in the weld pool, weld thermal cycle, vaporization of alloying elements and resultant composition change of the weld pool, liquid metal expulsion and weld pool solidification.

Experimental work, conducted at the Sandia National Laboratories, involved the determination of weld pool geometry, measurements of mass loss, electron microprobe analysis of weld pool composition change resulting from welding, determination of composition of the metal vapor by condensing a portion of the vapor on the inner surface of an open-ended quartz tube which was mounted perpendicular to the sample surface and co-axial with the laser beam, and also the observation of liquid metal expulsion during laser spot welding of 304 stainless steel. The laser power used is 530 to 1970 W, spot radius of 0.1 to 0.6 mm, and pulse duration of 2 to 8 ms for laser spot welding.

A comprehensive model was used to calculate heat transfer, fluid flow and vaporization of alloying elements during laser spot welding of 304 stainless steel. In the calculation of heat transfer and fluid flow, a three dimensional comprehensive numerical model was utilized to calculate the temperature and velocity fields, weld thermal cycle, weld pool geometry, solidification parameters and free surface profile, based on mass, momentum and energy conservation equations. Surface tension and buoyancy forces were considered for the calculation of transient weld pool convection. Using the calculated temperature fields, vaporization rate, vapor composition, mass loss and composition change due to vaporization can be computed. The vaporization results from both concentration and pressure driven transport. Both vaporization and condensation were considered in the model.

For Nd:YAG laser welding of 304 stainless steel with small length scale, the practical working range of laser powers that can be used for laser welding becomes restricted as the spot size is reduced by the limitation of upper and lower limits of peak temperature values of the boiling and melting points of 304 stainless steel, respectively. For a laser beam radius of 100 μm and a welding speed of 1 mm/s, the range of usable laser power is 25 to 320 W. For a laser beam radius of 50 μm with the same welding speed, the range of laser power is only 10 to 140 W.

The Peclet number was used to evaluate the relative importance of heat transfer by conduction and convection. During laser spot welding of 304 stainless steel, for a laser power of 530 W and beam radius of 0.16 mm, the Peclet number is higher than unity after 1 ms, which shows that the liquid metal convection continues to be an important mechanism for heat transfer within the weld pool as the scale of the weld is reduced.

Spatial feature of temperature in the weld pool for laser welding of 304 stainless steel was examined. At locations equidistant from laser beam axis, the temperatures on the top surface are higher than those along the direction perpendicular to the top surface. The weld thermal cycles for linear and spot laser welding show significantly different features. For linear welding, the heating rate initially increases with time, and the temperature reaches its peak value when the laser beam reaches directly above the monitoring location. For laser spot welding, the heating rate is very high at the first millisecond and then decreases gradually with increasing in temperature until the laser is switched off. As the weld metal cools, the spatial variation of the cooling rates decreases. In the range of 800 °C to 500 °C, the cooling rate is almost independent of position, which is due to nearly constant outward heat loss from all locations of the weld.

For Nd: YAG laser linear welding of 304 stainless steel, the values of G/R at weld center line are shown to increase with the increase in net heat input, ratio of the absorbed power and welding speed. So if the net heat input increases, the interface morphology changes from equiaxed-dendritic to cellular-dendritic and then, to cellular grains. The average cooling rate from 800 °C to 500 °C is directly proportional to the welding speed when the laser power and laser beam size are constant. For laser spot welding, the size of the mushy zone, i.e., liquid + solid two-phase region, grows significantly with time during solidification, and the maximum size of the mushy zone is reached when the pure liquid region vanishes. Under the condition of 530 W laser power, 0.159 mm beam radius and 4 ms pulse duration, the pure liquid region disappears about 0.8 ms after the solidification start, and the mushy zone exists for about another 0.9 ms before the weld pool solidifies completely. With the progress of solidification, the temperature gradient decreases, and the solidification rate increases. Under the welding condition of 100 W laser power and 100 μm beam radius, the temperature gradient and average cooling rate between 800 °C and 500 °C for laser spot welding with 5 ms pulse duration may reach to 2.5×10^3 K/mm and 160 K/ms, respectively, which are higher than those in linear laser welding with the welding speed of 1 mm/s. For the latter, the temperature gradient and cooling rate are 1.1×10^3 K/mm and 1.9 K/ms, respectively.

During Nd:YAG laser spot welding of 304 stainless steel, because of the high power density used, the temperatures on the weld pool surface were found to be higher than the boiling point of 304 stainless steel. As a result, significant vaporization of alloying elements, resulted from both pressure and concentration gradients, often takes place from the weld pool surface. The calculations show that the vaporization was concentrated in a small region under the laser beam where the temperature was very high. The vaporization rates of the constituent alloying elements increase with time. At the end of pulse cycle, vaporization rates decrease suddenly and the vaporization of the alloying elements stops. Under the condition of 1063 W laser power, 0.28 mm beam radius and 3 ms pulse duration, the total vaporization rate just before laser beam is switched off is 1.87

mg/s. Iron, chromium and manganese have been identified as the main metallic species in the vapor phase with a weight percent of 64.2%, 23.1% and 8.5%, respectively.

The vapor composition can also provide a rough idea of the peak temperature at the weld pool surface during Nd:YAG laser spot welding of 304 stainless steel. Since the relative rates of vaporization of two alloying elements are determined by the local temperature, the vapor composition can be used to determine an effective temperature of the weld pool. This temperature is close to the peak temperature because most vaporization takes place from weld center in the later potion of pulse duration. Under the condition of 1063 W laser power, 0.28 mm beam radius and 3 ms pulse duration, the effective temperature determined from the relative vaporization rate of iron and manganese is 3075 K. The peak temperature calculated from the heat transfer and fluid flow model is 3145 K. Estimation of the approximate values of peak temperatures during laser spot welding by measuring vapor composition overcame the problems encountered in direct measurement of peak temperatures.

Under the condition of 530 W laser power, 0.159 mm beam radius and 4 ms pulse duration, the maximum liquid velocity in the weld pool is about 95 cm/s. Because of such strong recirculating flow, the weld pool can be reasonably assumed to be well mixed and compositionally homogeneous. As a result of selective vaporization of alloying elements during laser spot welding, the composition in the weld pool can change. After laser spot welding with a 1067 W laser power, 0.225 mm beam radius and 3 ms pulse duration, the concentrations of manganese and chromium in the weld pool decreased by 0.115% and 0.375%, while the concentrations of iron and nickel increased by 0.327% an 0.163% owing to welding.

During Nd:YAG laser spot welding of 304 stainless steel, the computed vapor loss was found to be lower than the measured mass loss under various welding conditions, so the liquid metal expulsion was examined and verified by experiments. Liquid metal expulsion is caused by the recoil force exerted by escaping metal vapors when the temperature at the weld pool surface is very high, and can be predicted by balancing the vapor recoil force with the surface tension force at the periphery of the liquid pool. Larger laser power density and longer pulse duration increase the tendency of occurrence of liquid metal expulsion. For a 3.0 ms pulse duration, the critical laser power density for liquid metal expulsion is about 8.0 kW/mm^2. When the pulse duration is increased to 4.0ms, the critical laser power density decreases to about 7.0 kW/mm^2. The size of the ejected droplets ranges from tens of micrometers to several hundreds of micrometers. Increase of power density results in larger droplets and greater size range of particles. In addition, the depression of the weld center under the recoil pressure could be used as an indicator of liquid metal expulsion during laser spot welding.

The most important feature of this study is its usefulness in understanding the heat transfer, fluid flow and vaporization of alloying elements for laser welds with small length scale based on the fundamentals of transport phenomena. The results obtained from the mathematical models developed in the present thesis provide not only improved understanding of laser welding processes from a scientific point of view but also a guidance for practical welding application. Using a reliable comprehensive mathematical model, the conventional trial and error approach for the determination of welding parameters for a given task can be minimized. The research presented in this thesis is a contribution to the growing quantitative knowledge base in laser welding with small length scale. Expansion of this knowledge base is helpful to achieve structurally sound, defect free welds in welding industry.

7.2 Suggestions for Future Work

Some solidification parameters, such as solidification rate and cooling rate, were calculated by heat transfer and fluid flow model. The calculation was based on the heat transfer and fluid flow only. An accurate prediction of the weld pool solidification will require consideration of both the thermodynamics and kinetics of solidification.

Incorporating a solidification model with the heat transfer and fluid flow model is an effective approach to better understand the solidification process in the weld pool.

In the calculation of temperature fields, the effect of heat loss owing to vaporization was ignored. A more realistic simulation of temperature fields may need to consider the effect of evaporative heat loss. It can be realized by incorporating heat transfer and fluid flow mode with vaporization model. In such a case, the convergence will be more difficult and the calculation time will increase.

In the calculation of composition change, the weld pool was assumed to be well mixed and compositionally homogeneous. The spatial features of concentrations of different alloying elements were ignored. Besides mass, momentum and energy conservation, species conservation can be included in the calculation to obtain the concentration distribution of different elements in different locations in the weld pool.

Liquid metal expulsion is a complex process. Few literatures are available on liquid metal expulsion during laser welding. The further investigation of mechanism of liquid metal expulsion and simulation of the size of rejected droplet will help to understand liquid metal expulsion better.

VITA

Xiuli He

Xiuli He was born in Heilongjiang Province, China, on March 16, 1973. She obtained both Bachelor and Master degrees of engineering in Materials Science and Engineering at Beijing University of Aeronautics and Astronautics in 1995 and 1998, respectively. In the spring of 2002, she joined the Pennsylvania State University to pursue doctoral study in Materials Science and Engineering. She is a member of American Welding Society (AWS), and American Society of Metals (ASM International). A list of her publications during her Ph. D. study at Pennsylvania State University is as follows:

1. X. He, J. T. Norris, P. W. Fuerschbach and T. DebRoy, *Liquid metal expulsion during laser spot welding of 304 stainless steel*, *Journal of Physics D: Applied Physics*, to be published.
2. X. He, J. T. Norris, P. W. Fuerschbach, T. DebRoy, *Alloying element vaporization and liquid metal expulsion during laser micrjoing of stainless steel with short pulse,* Proceedings of 7th International Conference on Trends in Welding Research, May 2005, Pine Mountain, GA, to be published.
3. X. He, J. W. Elmer and T. DebRoy, *Heat transfer and fluid flow in laser microwelding*, *Journal of Physics D: Applied Physics*, **97**, 084909 (2005).
4. X. He, T. DebRoy, and P. W. Fuerschbach, *Composition change of stainless steel during microjoining with short laser pulse*, *Journal of Applied Physics,* **96**, 4547 (2004).
5. X. He, P. W. Fuerschbach, and T. DebRoy, *Heat transfer and fluid flow during laser spot welding of 304 stainless steel, Journal of Applied Physics, Journal of Physics D: Applied Physics,* **36**, 1388 (2003).
6. X. He, T. DebRoy, and P. W. Fuerschbach, *Probing temperature during laser spot welding from vapor composition and modeling*, *Journal of Applied Physics,* **94**, 6949 (2003).
7. X. He, T. DebRoy, and P. W. Fuerschbach, *Alloying element vaporization during laser spot welding of stainless steel*, *Journal of Physics D: Applied Physics*, **36**, 3079 (2003).